JIMMA UNIVERSITY

SCHOOL OF GRADUATE STUDIES

JIMMA INSTITUTE OF TECHNOLOGY

FACULTY OF MATERIALS SCIENCE AND ENGINEERING

CHAIR OF CERAMICS ENGINEERING

MASTERS OF SCIENCE PROGRAMME IN CERAMICS ENGINEERING

Tuning the Thermoelectric Transport Properties of Pseudo-Binary Cu_2Te - Sb_2Te_3 System by Unidirectionally Solidification and Brine Quenching

A thesis Submitted to the School of graduate studies of Jimma University in Partial Fulfilment of the Requirement for Degree of Masters of Science in Ceramics Engineering.

By

Surafel Shiferaw Legese

August 2020

Jimma, Ethiopia

JIMMA UNIVERSITY

SCHOOL OF GRADUATE STUDIES

JIMMA INSTITUTE OF TECHNOLOGY

FACULTY OF MATERIALS SCIENCE AND ENGINEERING

CHAIR OF CERAMICS ENGINEERING

MASTERS OF SCIENCE PROGRAMME IN CERAMICS ENGINEERING

Tuning the Thermoelectric Transport Properties of Pseudo-Binary Cu_2Te - Sb_2Te_3 System by Unidirectionally Solidification and Brine Quenching

A thesis Submitted to the School of graduate studies of Jimma University in Partial Fulfilment of the Requirement for Degree of Masters of Science in Ceramics Engineering.

By

Surafel Shiferaw Legese

Main Advisor: Dr. Olu Emanuel Femi (PhD)

Co-Advisor: Prof. Kamanio Chattopadhyay

August 2020

Jimma, Ethiopia

JIMMA UNIVERSITY

SCHOOL OF GRADUATE STUDIES

JIMMA INSTITUTE OF TECHNOLOGY

FACULTY OF MATERIALS SCIENCE AND ENGINEERING

CHAIR OF CERAMICS ENGINEERING

MASTERS OF SCIENCE PROGRAMME IN CERAMICS ENGINEERING

Tuning the Thermoelectric Transport Properties of Pseudo-Binary Cu_2Te - Sb_2Te_3 System by Unidirectionally Solidification and Brine Quenching

By

Surafel Shiferaw Legese

Approved by Board of Examiners:

Dr Georgies Alene (Phd)		30/10/2020
External Examiner	Signature	Date
Dr Mulalem Abebe (PhD)	_____	____/____/_____
Internal Examiner	Signature	Date
Dr Lodric Wangatia	_____	____/____/_____
Chairperson	Signature	Date
Dr Olu Emmanuel Femi (PhD)	_____	____/____/_____
Main Advisor	Signature	Date
Prof. Kamanio Chattopadhyay	_____	____/____/_____
Co- Advisor	Signature	Date

Declaration

I, Surafel Shiferaw Legese, declare that this thesis work titled "Tuning the Thermoelectric Transport Properties of Pseudo-Binary Cu_2Te - Sb_2Te_3 System by Unidirectionally Solidification and Brine Quenching" is my original work. This work has not been accepted for any degree and is not concurrently submitted for award of other degree. Except where states or otherwise, are fully acknowledged in accordance with the standard referencing practices, the work presented is entirely my own.

Surafel Shiferaw Legese (BSc.) _____ ____/____/_____

Candidate Signature Date

As master Research advisor, we here by certify that we have read and evaluate this MSc research under our guidance by Surafel Shiferaw Legese entitled "Tuning the Thermoelectric Transport Properties of Pseudo-Binary Cu_2Te - Sb_2Te_3 System by Unidirectionally Solidification and Brine Quenching". The experimental part of this research is conducted in Department of Materials Engineering, Indian Institute of Science, IISc, Bangalore, India, with help of Shriparna Mukherjee and Aramanda Shanmukha Kiran under supervision of Prof. Kamanio Chattopadhyay.

We recommended that it can be submitted as fulfilling for M.Sc. thesis requirement.

Dr Olu Emanuuel Femi (PhD) _____ ____/____/_____

Main Advisor Signature Date

Prof. Kamanio Chattopadhyay _____ ____/____/_____

Co- Advisor Signature Date

Acknowledgement

It is with the deepest senses gratitude of the almighty that gives strength and ability to complete this thesis successfully.

First of all, I would like to give my sincere appreciation to my supervisor, Dr. Olu Emmanuel Femi for taking me under his supervision. He has given me critics, encouragement, guidance, and valuable advice to complete this research proposal.

I am grateful to Jimma Institute of Technology, Jimma, Ethiopia for a Master scholarship and office of International relation (OIR), Indian Institute of Science for support. And also would like to acknowledge the microscopy facilities (EPMA and SEM) available at the Advanced Facility for Microscopy and Microanalysis (AFMM) and at Department of Materials Engineering, Indian Institute of Science, Bangalore, India.

My sincere thanks also go to Prof. Kamanio Chattopadhyay, who has accepted me to carry out experimental work in his laboratory at the Indian Institute of Science Bangalore India.

My deep thanks also go to others who have assisted at various occasions whether directly or indirectly in the completion of my research thesis. Last, but certainly not least, my special thanks also extends to my family for the continual encouragement and support.

Abstract

The rapidly depleting available energy resources have led to an increased research focus on the development of alternative energy sources. In this aspect, research on the development of efficient thermoelectric (TE) materials and integrating them into devices has taken a lead role in recent years worldwide. Thermoelectricity is a phenomenon of conversion of thermal energy into electrical energy and vice versa. The conversion efficiency of a TE material is dependent on a dimensionless parameter known as the figure of merit zT, which is directly related to the product of electrical conductivity (σ) and the square of the Seebeck coefficient (S) whereas inversely related to the thermal conductivity (κ).

This research contains two studies. In the first studies, we explore in-situ lamellar composites of $(Cu_2Te)_{62.02}$-$(Sb_2Te_3)_{37.98}$ produced by directional solidification using a modified Bridgman apparatus and its effect on the thermoelectric properties. The eutectic microstructure under higher growth rates exhibits a cellular microstructure due to growth instability (and hence segregation at cell boundaries) with cell spacing varying with growth rates. Further, a quantitative evaluation of the scale of the microstructure in terms of interlamellar spacings allows us to evaluate the role of the microstructure in tuning the thermoelectric properties as a function of temperature. An additional significant observation of the present work is a relatively mild variation of the power factor across a range of temperatures (300 K to 600 K) in this eutectic system along the transverse direction.

In the second study, we report the microstructure and thermoelectric Properties Of $(Cu_2Te)_X(Sb_2Te_3)_{100-x}$ pseudobinary system synthesized by brine quenching method and compare the microstructure and transport properties to the same composition synthesized by solid-state synthesis.

Keywords: Thermoelectric, Directional solidification, eutectic, lamellar spacing, power factor, brine quenching solidification, pseudo-binary system

Glossary

TEG – Thermoelectric generator

TE – Thermoelectrics

S– Seebeck Coefficients

σ– Electrical Conductivity

T– Temperature

κ –Thermal Conductivity

TEC – Thermoelectric cooler

V – Voltage

N – Number of couples

ΔT – Temperature gradient

Sp – Seebeck coefficient of p – type semiconductor

Sn – Seebeck coefficient of n – type semiconductor

η - Thermoelectric device efficiency

Th – Hot Temperature Tc – Cold Temperature

κ_l / κ_e – Lattice / electron thermal conductivity

n – Number of carrier K_B – Boltzman Constant

h – Planks constant m* - carrier effective mass

μ - mobility ρ – Electrical resistivity

m_b – band effective mass

L – Lorenz factor

PGEC – Phonon glass electron crystal

d_{hkl} – Interplaner spacing

λ – Wave Length

Table of Contents

CHAPTER ONE

1. Introduction and Literature Review

Humanity's desire for energy is to give rise to significant growth of social and political stability. Likewise, the global climate's environmental impact due to the combustion of fossil fuels is becoming increasingly terrifying. One method to improve the long-lasting electricity desire is through searching for waste heat with thermoelectric generators. Home utensils used for heating and cooking, self- propelling exhaust, and industrial processes all generate a significant quantity of unused waste heat that could be converted to electricity by using thermoelectric materials.

The rising concern with the debilitation of energy resources essential to contemporary life, such as natural gas, oil, and coal, gives the growth of new technologies based on the use of alternate natural resources: wind energy, solar bioenergy, hydroelectric energy geothermal energy, etc. Regarding the thermal energy, it inhabited a special position in human activities, since it accompanies the majority of industrial processes and processes occurring in Nature. In most cases, the waste heat is lost without any economic profit. This energy resource does not cost anything and can be used to reduce both the impact of the energy crisis and global warming. Therefore, the interconversion of waste heat into electricity could play a significant role in a global sustainable energy solution. The conversion of heat into electricity is known as the thermoelectric generator (TEG) [1]. The materials which convert heat flow into electrical current and vice versa are known as thermoelectric materials [2-4]. These materials can be used either in power generation or refrigeration, respectively [5].

Thermoelectric (TE) modules can couple heat and electric current. This approach offers a possible power generation route from different sources of waste heat, such as car exhaust and industrial plants. Compared to competing technologies, such as traditional heat engines, a thermoelectric device that contains no moving part or fluids are noise and emission-free. They

can be of small size and operate at low powers (mile- or microwatts) as an energy source for remote sensors. TE modules are also used for many cooling applications [6]. Historically, in 1821, the German scientist Thomas Johann Seebeck noticed an interesting experimental result that a compass needle was rebounded by a nearby closed-cycle jointed by two different metals, with a temperature difference between junctions. This phenomenon is called the Seebeck effect, where an applied temperature difference drives charge carriers in the material (electrons and/or holes) to diffuse from hot side to cold side, resulting in current flow through the circuit [7].

Thermoelectric materials have long been incompetent to be cost-effective in most applications. However, a revival of interest in thermoelectric materials began during the mid20 centuries; the thermoelectric field gained attention from the worldwide scientific research community when theoretical predictions suggested that thermoelectric efficiency could be significantly enhanced through nanostructural engineering, which leads to experimental efforts [8, 9]. At the same time, complex bulk materials (such as skutterudites [10], Oxides [11], Chalcogenides, clathrates [12], Zintl phases [13] and half-huesuler [14]) have been investigated and found that high efficiencies could indeed be obtained. The efficiency of both power generation and refrigeration is determined in general by a measure of material`s dimensionless figure of merit, $_zT$ define as

$$zT = \frac{S^2 \sigma T}{\kappa} \tag{1.1}$$

S, σ, T, and κ are the Seebeck coefficient, electrical conductivity, absolute temperature, and thermal conductivity.

1.1. Thermoelectric devices efficiency

The schematic figure of a thermoelectric cooler (TEC) is given in Fig. 1a. As of this figure, several preferred material properties become easy to understand. This cooler, also is known as "Peltier cooler," contains two electrodes, one of which is p-type, which has positive charges (holes), and the other leg is n-type and contains mobile electrons. These two electrically

conducting legs are connected by a metal (black bar) at the top to make a junction. These two electrodes are connected thermally in parallel and electrically in series. When the current is passed through the electrodes along the direction shown in the figure, both the holes and electrons flow from the top toward the bottom of the device and carry heat from the junction at the top of the device toward the base, cooling the junction at the top [15, 16]. A thermoelectric generator (TEG) is the reverse of a Peltier cooler. A thermoelectric generator (TEG), as showed in Fig. 1.1b.It generates electricity in the presence of an externally generated temperature gradient. In this instance, both carriers conduct heat from the heated junction at the top to the cooled side at the bottom, and a voltage drop is generated between the electrodes at the bottom of the heat sink [16].

Besides cooling the top junction, when current is passed, it results in Ohmic heating in each electrode. Ohmic heating is the process where the energy of electric current is converted into heat. So, materials with low resistivity are required. Moreover, to stop the hold-up of the flow of heat from hot to cold, after reaching thermal equilibrium, low thermal conductivity is necessary. The significant parameter is the Seebeck coefficient, which measures the voltage generated across the material due to a temperature difference [15]. The large Seebeck coefficient is desired to maximize the voltage output for a given temperature drop.

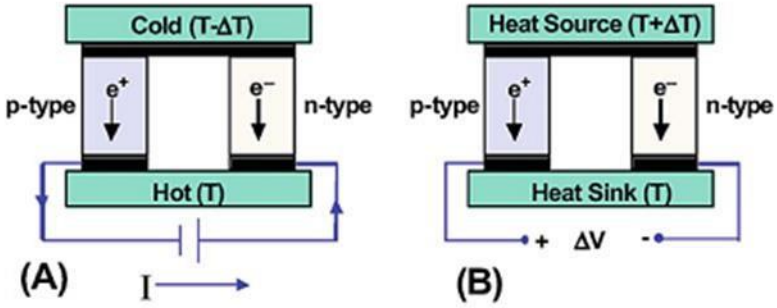

Fig. 1.1. A schematic diagram of the thermoelectric cooler (A) and generator (B) [8]

The voltage (V) generated by a thermoelectric generator (TEG) is directly proportional to the number of couples (N) and the temperature gradient (ΔT) between the heat sources and heat sink sides of the and the Seebeck coefficients of the p-type and n-type materials (Sp and Sn, respectively):

$$V=N\ (Sp - Sn)\ \Delta T \tag{1.2}$$

Thermoelectric device efficiency from a TEG is given by:

$$\eta = \frac{Th-Tc}{Th}\frac{\sqrt{(1+zT)}-1}{\sqrt{1+zT}Tc/Th} \tag{1.3}$$

1.2. Thermoelectric material properties, physics, and principle

Essential to the field of thermoelectric materials is the need to enhance a variety of properties. There are two obvious ways to increase ZT: either boost the power factor ($S^2\sigma$); a high Seebeck coefficient (thermopower), high electrical conductivity, or lower the thermal conductivity (k = kl + ke; thermal conductivity is the sum of lattice thermal conductivity and electrical thermal conductivity), especially the lattice thermal conductivity is required. Currently, the high TE performance of the present composites is mainly due to the extremely low lattice thermal conductivity resulting from phonon scattering [17]. As often, these are typically contra-indicating properties; that is, efforts to increase one result in the compromise of the other [18]. As these transport characteristics are determined by interconnected material properties, numerous parameters need to be enhanced to maximize *zT*.

1.2.1. Carrier concentration

The total number of carriers (n) involved in the conduction mechanism is one of the significant parameters in the property optimization method. Only one kind of carrier, either n or p-type, is present in the transition process, leading to a larger Seebeck coefficient. If mixed n-type and p-type conduction is present in the same system, it will cancel out the induced

Seebeck voltages by individual carriers and reduce the resultant Seebeck coefficient [19]. One of the primary advantages that semiconductors offer is the ability to change the electrical conductivity via doping. Based on the electron transport model of Mott-Boltzmann formalism with energy independent carrier scattering, Low carrier concentration insulators, and semiconductors have large Seebeck coefficients [20]. However, to the extent that the electrical conductivity is concerned, it is directly proportional to carrier concentration and is decreased for low carrier concentration, as described in Eq. (2): The interdependency between the Seebeck coefficient and carrier concentration can be seen from quite simple models of electron transport. For metals or degenerate semiconductors, the Seebeck coefficient is given by:

$$S = \frac{8x\pi^2 k^2 \mathrm{B}}{3eh^2} \; m^*T \left(\frac{\pi}{3n}\right)^{2/3} \tag{1.4}$$

$$\frac{1}{\rho} = \sigma = ne\mu \tag{1.5}$$

Where m* is the carrier's effective mass, n is the carrier concentration, μ is the carrier mobility, ρ is the electrical resistivity, σ is the electrical conductivity, K_B Boltz man constant and h planks constant.

Generally, optimizing Seebeck coefficient and electrical conductivity, according to Eqs (1.4) and (1.5), have been found in heavily doped semiconductors, in which the carrier concentration ranges between 10^{19} and 10^{21} carriers per cm^3 which, have a positive effect on the Seebeck coefficients. In the comprehensive form, in thermoelectric materials, the relationship between

the Seebeck coefficient, thermal conductivity, and electrical conductivity with carrier concentration, for maximum Figure of merit (zT), can be represented as in Fig. 1.2 as follow:

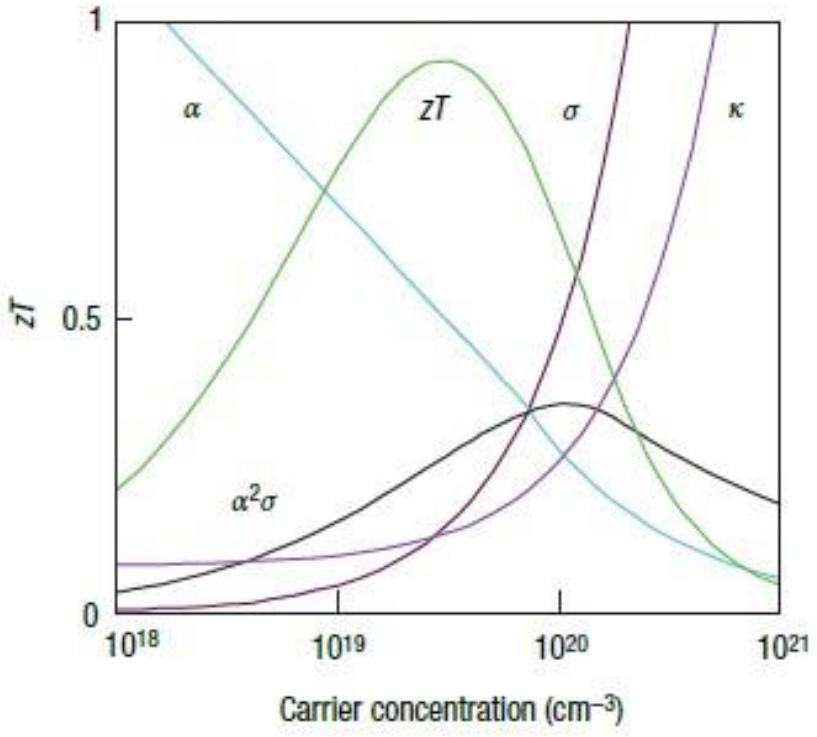

Fig. 1.2. Optimizing ZT through carrier concentration tuning [13]

1.2.2. Effective mass

Finding a way to tune a figure of merit (zT) using S, σ and Ke separately has been a big challenge since they are strongly interdependent through band structure, scattering, and carrier concentration [21]. However, for the optimal electronic performance of a thermoelectricity semiconductor depends mainly on non-degenerate mobility of carrier. The discussion of the carrier mobility (electrons or holes) in semiconductors is usually based on the use of the concept of effective mass [22]. The density-of-state effective mass (m^*_d) is related to the band effective mass (m_b) by the relation of $m^*_d = N^{2/3} m_b$. Also, in the case when carriers are mainly scattered by acoustic phonons, the carrier mobility depends on the band's effective mass and the inertial effective mass according to the relation of $m^* = m_I^{-1} m_b^{-3/2}$. Getting a high Seebeck coefficient by producing large density-of-states effective mass through either electronic structure

modification or controlling nanostructures is commonly considered as a way to advanced thermoelectric materials.

Stability must be found for the effective mass (or bandwidth) for the principal charge carrier, forming cooperation between high mobility and high effective mass. Low effective mass and high mobility are classically found in materials made from elements with a small electronegativity difference; however high low mobility and effective mass are found in materials with narrow ban gap such as ionic compounds.

1.2.3. Thermal conductivity

A significant quantity in the denominator of Eqs. (1.1), the figure of merit ($_Z$T) is thermal conductivity. Therefore, to attain a high value of zT, a lower value of thermal conductivity is required, along with increased electrical conductivity and Seebeck coefficient values. Good thermoelectric materials require a low thermal conductivity to prevent a significant portion of the heat from flowing down the temperature gradient [23]. On the other hand, the reduction in thermal conductivity is pretty complex in the logic that it must occur without any contrary effect on the electronics properties, for instance, the electrical conductivity and Seebeck coefficient [19].

Thermal conductivity in thermoelectric materials arises from two sources: (1) electrons and holes transporting heat, electronic thermal conductivity (κ_e), and (2) phonons travelling through the lattice; lattice thermal conductivity (κ_l).

1.2.3.1. Electronic thermal conductivity

Electronic thermal conductivity (κ_e) signifies the contribution of charge carriers, for instance, holes and electrons, to transporting heat. A low thermal conductivity is a vital criterion that needs to be considered for material selection for improved $_Z$T. The electronic components of the thermal conductivity cannot be changed much as it is associated with the Lorenz factor defined in Eq. (1.5) which differs mainly with the transport mechanism and the carrier concentration except in low carrier concentration materials wherein, the Lorenz factor can be

decreased up to 20% from the free-electron value. Another prospect of a reduction in electronic concentration thermal conductivity is a bipolar effect. Irrespective of reduced electronic contribution to the total thermal conductivity, the Seebeck coefficient values are decreased significantly by mixed conduction. Most of the electronic term (k_e) is directly related to the electrical conductivity through the Wiedemann Franz law and given by the formula:

$$k_T = k_e + k_l \tag{1.6}$$

$$k_e = \sigma LT = ne\mu LT \tag{1.7}$$

Where L is the Lorenz factor, 2.4×10^{-8} J^2 K^{-2} C^{-2}. For free electrons, high zT requires low thermal conductivity but high electrical conductivity, the Wiedemann Franz low make known an intrinsic materials conflict for attaining high thermoelectric device efficiency. For materials with high electrical conductivity or very low lattice thermal conductivity like metals, the Seebeck coefficient alone mainly decides *zT*, as can be seen in equation (4), where (κl/κe) <<1.

1.2.3.2. Lattice thermal conductivity

If it were not for their low charge-carrier mobility and accompanying poor electrical conductivities, one might look to non-metallic amorphous solids (glasses) as candidate thermoelectric materials: they possess some of the lowest thermal conductivities of all fully dense solids [24]. Glasses have poor thermoelectric properties because they lack the required ‘electron-crystal` properties compared with crystalline semiconductors, they have lower mobility due to lower effective masses and increased electron scattering because of broader bands. Therefore, good thermoelectric material is crystalline in materials and manages to scatter phonons without significantly disturbing the electrical conductivity. Thermoelectric materials, therefore, require a “glass-like” thermal conductivity values called a `phonon-glass electron-crystal` (PGEC) which, was first introduced by Slack [25]. The electron-crystal requirement arises from the circumstance that crystalline semiconductor has been the best at

fulfilling the requirement for the electronic properties (electrical conductivity and Seebeck coefficient). The phonon glass necessity arises from the need for a low lattice thermal conductivity as much as possible.

One common feature of thermoelectric materials with zT >1 is that these thermoelectric materials have lower lattice thermal conductivities than the current commercially available thermoelectric materials. Therefore the general achievement is that they maintain the 'electron crystal' by getting closer to 'phonon glasses.` While this decreased lattice thermal conductivity is attained through phonon scattering across various length-scales, a reduced lattice thermal conductivity directly improves the thermoelectric efficiency, zT.

There are three main approaches to reduce lattice thermal conductivity that has been effectively used. The first approach is to scatter phonons inside the unit cell by generating fast-moving structures or point defects such as vacancies or interstitials by alloying [26]. The second approach is to use complex structures to distinct the electron crystal from the phonon glass. At this time, the aim is to attain a phonon glass without disturbing the crystallinity of the electron transport region [25, 27]. A third approach is to scatter phonon at the interface, leading to the use of multiphase composites mixed on the nanometre scale. These physical phenomena affect not only the phonon scattering but, similarly, the band structure of the material modifying the Power Factor [28].

1.2.4. Power factor enhancement

The rapid advancement in thermoelectric properties enhancement is focused on the efforts of the development of experimental methods and understanding phonon transport to reduce lattice thermal conductivity. This fact leads to the disregard of concepts to enhance electronic transport, and thermoelectric power factor. With a thermal conductivity of the potential thermoelectric material approaching the minimum theoretical limit, on the advance to higher zT values, it is essential to consider the improvement of thermoelectric power factor [29]. The application of small potential barriers that could enhance the power factor was first suggested

by Rowe and Min [103] as well as Whitlow and Hirano [104]. Shakouri and Bowers first proposed inserting tall barrier layers into degenerate semiconductor superlattices for selective emission of hot electrons and thus a higher PF.

Furthermore, Vashaee and Shakouri pointed out that the lateral momentum must be relaxed to allow a larger number of hot electron emissions for a higher PF in the direction perpendicular to planar barriers [30]. The temperature requirement of the thermoelectric power factor reported for different classes of high-performance n-type and p-type TE materials. It is observed that the majority of high-performance thermoelectric materials possess power factor values between 0.8 and 2.5 W $m^{-1} K^{-1}$. The largest PF values reported in n-type materials belong to intermediate valance $YbAl_3$. Multiple filled half-Heusler alloys, skutterudites, and SiGe exhibit the largest reported values in p-type materials with PF value 0.8 W $m^{-1}K$.

Different approaches have also been proposed to increase the power factor, such as energy filtering [6], modulation doping [7], quantum confinement [8] and percolation effect [9]. Some of them have been successfully utilized in experiments, e.g., the power factor of a twophase nanocomposite sample (Si80Ge20)80(Si100P3)20 was improved by 40% compared to the uniformly doped sample by using the modulation-doping approach [7]. In these all approaches, interfaces usually play an important role in the power factor enhancement.

In the past few decades, intensive efforts have been devoted to improving ZT of TE materials, in which interface engineering has been confirmed to be an effective strategy via decreasing κ and/or boosting PF. Hence, an effective thermoelectric material should have a high power factor ($PF = S^2\sigma$) [31].

1.3. Thermoelectric Materials

Three different classes of medium-high to high-temperature thermoelectric materials, i.e., skutterudites [10], Oxides [11], Chalcogenides, clathrates [12], Zintl phases [13], Halfhuesuler

[14] and high entropy [32-35] will be discussed below concerning their physical and thermophysical properties as well as recent advances in materials design.

1.3.1. Skutterudites

Skutterudites are one class of materials that have received a lot of attention within the TE community since the 1990s [36]. Among the most promising materials for a widespread thermoelectric application in a waste heat gradient from room temperature to about 900 K are filled skutterudites with the general structural-chemical formula $EPyT4_X12$, where the filler atom EP is usually an electropositive element species enclosed by an icosahedral cage structure formed by tilted pnictogen octahedral (eight per formula unit, made from atoms X) each cantered by a transition metal atom, T [37]. The ideal is that these filler atoms can clatter in these voids, resulting in a lower lattice thermal conductivity by point defect scattering. The most important features to use skutterudites as thermoelectric (TE) materials are: (i) the starting material is abundant and cheap among other thermoelectric mas, (ii) they are of high TE quality (ZT >1), (iii) they can be used in a wide Te, range (room temperature to 900 K, they reveal long-term thermoelectric stability, and (v) they show reasonable mechanical performance. Skutterudites are CoSb3 based minerals found in small mining in Norway called Skutterud. They are cage-like materials with voids in their structure that can be filled with guest atoms that can clatter in this void and scatter phonon via point defect scattering, thereby reducing lattice contribution to thermal conductivity. They are also studied under the concept of phonon glass electron crystal, i.e., materials with electrical conductivity like that of a single crystal and a lattice thermal conductivity like that of a glass [38]. Cahill et al. enumerate the criteria for a glass-like lattice thermal conductivity, which includes possession of loose atoms that have no long-range correlation with one another and are an integral part of the compound rather than the rattler/impurity atoms [39]. $CoSb_3$ and all Skutterudites satisfy the requirement of Cahill *et al.* for small lattice conductivity and possess reasonably mobile charge carriers.

The general formula for basic Skutterudites is given ad MX_3 where M can be Co, Rh or Ir, and X can be P, As, and Sb. They can also be represented as $[\ G]_2M_8X_{24}$ taking into account the two voids (G) for every 8M atoms and 24 X atoms. Guest atoms are therefore introduced into these voids to form filled Skutterudites. The ideal is that these guest atoms can rattle in these voids, thereby leading to a lower lattice thermal conductivity by point defect scattering.

Shi *et al.* reported a ZT of 1.7 at 850 K by co-filling Ba, La, and Yb atom into the $CoSb_3$ voids. The observed ZT was attributed to a reduced lattice thermal conductivity through the combination of filler species of different rattling frequencies in these voids to achieve a broad frequency phonon scattering [40]. Filled antimonide compound with formula $R_{1-y}Fe_{4x}Co_xSb_{12}$ with ZT great than 1 at elevated temperature (700-1000 K) was reportedly synthesized by Sales *et al.*, who claimed that the incoherent rattling of the weakly bonded rare-earth atoms in the void of the skutterudite gave rise to the observed thermoelectric properties [41]. Similar work by Tang *et al.* also showed a decrease in the thermal conductivity of filled skutterudite $Ce_yFe_xCo_{4-x}Sb_{12}$ with increasing substitution of Fe at Co sites and increasing Ce filling fraction. A maximum ZT of 0.8 was obtained for the composition $Ce_{0.12}Fe_{0.71}Co3.29Sb_{12}$ at 750 K [42]. This value reported for multiply filled skutterudite is significantly higher than single element filled and non-filled Skutterudites.

In most Skutterudites, the guest atom that is introduced into the voids also acts as dopants, and the high effective mass allows their carrier concentration to be high without the Seebeck coefficient becoming too small. The effect of double-doping on the pnicogen rings with Ge and Te via melt spinning techniques resulted in a binary skutterudite $CoSb_{2.75}Ge_{0.5-x}Te_x$ with a ZT value of 1.1 at 750 K as reported by Su *et al.*[43]. Filled and unfilled skutterudite are continually being researched for high-temperature applications because they can be tuned to exhibit tremendously low lattice thermal conductivity.

1.3.2. Oxides

Oxides are potential thermoelectric materials for high-temperature applications because they are thermally stable, chemically inert, and generally non-toxic [44]. The layered cobalt oxides, such as Na_xCoO_2 (2) and $Ca_3Co_4O_9$ (CO-349) (3), were discovered in Japan to be good *p*-type TE materials for approximately 20 years ago. Many of the oxide thermoelectric materials like $SrTiO_3$ and $NaCo_2O_4$ possess layered superlattice structures resulting in a low thermal conductivity perpendicular to the layers while maintaining good electrical conductivity within the layers. The first investigation of oxides as potential thermoelectric materials was reported by Terasaki *et al.* in single-crystal $NaCo_2O_4$ metallic transition-metal oxides consisting of a two-dimensional triangular lattice of Co [45]. Yakabe *et al.* prepared $NaCo_2O_4$ by sintering via hot and cold press technique. The figure of merit of the hot-pressed sample was $0.5x10^{-3}$ K^{-1} over the temperature range of 100-400°C with a Seebeck coefficient ranging between 100 and 140 μVK^{-1} [46]. The properties were further improved by Ba or Bi substitution for Na and Cu or Bi substitution for Co, which resulted in 1.4 times enhancement in the power factor. This earlier work gave understanding into the potential range of ability of oxides as prospective TE materials. Oxides TE developed due to its promising performance and environmental friendliness [47]. However, they usually have lower mobility and higher lattice thermal conductivity than other thermoelectric materials, due to the high electronegativity of oxygen and the strong bonding of light atoms. These properties give oxides a major drawback limiting these materials to broaden their application.

1.3.3. Full-Heusler's, Half-Heusler's and Double Half- Heusler's alloys

Both Heusler's and half-Heusler's phases have attracted a lot of research interest over the past few decades because they are among the best known ternary intermetallic compounds which are environmentally friendly, mechanically stable, and can withstand high temperature. The half-Heusler phase consists of XYZ chemical composition where X is usually the most

electropositive and it can be a transition metal, noble metal or a rare-earth metal, Y is a less electropositive and it is either a transition metal or noble metal and Z is the most electronegative and the main group element [48], XYZ forms a MgAgAs type structure with a space group F4 $\bar{3}$m with a unit cell compressing three interpenetrating face-centred cubics

(FCC) sublattice occupying Wyckoff positions (0,0,0) for X, (1/4, 1/4, 1/4), for Y (3/4, 3/4, 3/4) positions for Z atom[49]. The remaining (1/2, 1/2, 1/2) positions are empty for half huesuler.

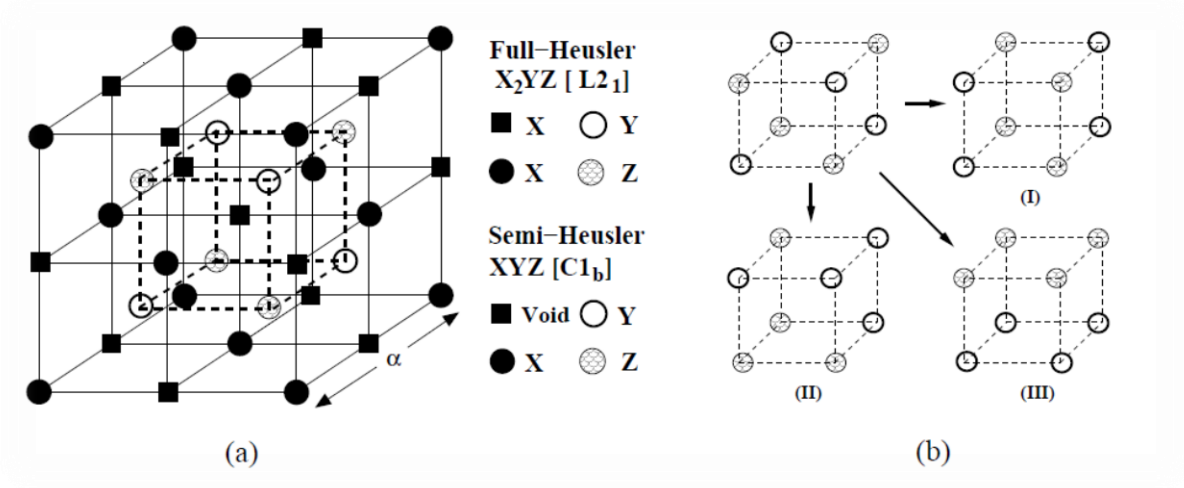

Fig. 1.3: Heusler Alloys: Experimental and Theoretical Background [14]

The Heusler phase, on the other hand, is generally represented by X_2YZ, forming a Bi_3F type structure with space group $Fm\bar{3}m$ in which the unit cell consists of four interpenetrating face-centred Cubic's (FCC) sublattices [50]. The semiconducting Heusler compounds can be identified by the number of valence electrons [49] forming closed 18 or 28 valence-electron shells, in addition to vacancy-compensated 19 valence-electron compounds [51]. The semiconducting nature of these materials due to the formation of a pseudo-gap in the density of states makes them promising for intermediate temperature thermoelectric materials. Cooks *et al.* reported a Seebeck coefficient as high -200 to -400 µV/K at room temperature for the compound MNiSn (M=Ti, Zr, and Hf) a semiconducting behaviour [52]. Uher *et al.* also studied the transport properties in pure and doped intermetallic of the form MNiSi (M=Zr, Hf)

half-Heusler alloys. They observed that the transport properties are sensitive to the constituent atoms' structural arrangement, which can be manipulated by annealing, isostructural alloying, and doping [53]. Kimura *et al.* also investigated the thermoelectric behaviour of half-Heusler compounds MPtSn (M= Ti, Zr, and Hf) by using an optical floating zone melting technique for the direct solidification of such compounds. Both ZrPtSn and HfPtSn showed p-type thermoelectric properties with a thermopower around 70 μV/K and 250 μV/K respectively at intermediate temperature range while TiPtSn exhibited an ntype behaviour with a very high thermopower of -500 μV/K at room temperature. The electric resistivities in these compounds were very high, leading to a high lattice contribution to thermal conductivity [54].

To reduce the fairly large thermal conductivity in this class of materials, the addition of impurity atoms has been explored to eliminate the bipolar electronic conduction rather than a decrease in the lattice contribution to thermal conductivity, as reported by Mutu *et al.* [55]. By the combination of spark plasma sintering and arc-melting with substitution of Nb and Sn sites in NbCoSn alloys, Ono *et al.* observed an improved power factor of 2.2 $mWm^{-1}K^{-1}$ for the composition $Nb_{0.99}Ti_{0.01}CoSn_{0.9}Sb_{0.1}$ at 700 K. However; such substitution could not significantly reduce the lattice contribution to thermal conductivity resulting in a ZT of 0.3 at 850 K [56].

Half-Heusler and Heusler alloys have interesting attributes in addition to those already mentioned that makes them stand out as potential thermoelectric material. Such attributes include the fact that they can be easy to synthesis using conventional arc melting procedures; they are easy to cut due to very good mechanical sturdiness. Neither single crystals nor oriented films are required to maximize these systems' thermoelectric properties because of their isotropic structures.

1.3.4. Chalcogenides

The metal chalcogenides, a sequence of materials composed of both chalcogen elements (S, Se, and Te) and metal, have been attracting significant consideration in a variety of energy applications, including solar cells, light-emitting diodes, sensors, batteries, supercapacitors, thermoelectric devices, etc. [9]. Compared with oxides, metal chalcogenides based thermoelectric materials possess a higher power factor (PF = $S^2\sigma$), because of arising from low electronegativity, the less covalent nature of their bonds. Their heavy atomic weight compared to some other thermoelectric materials is of advantage for reducing thermal conductivity. Also, the chalcogenides are easy to form into different structures, which offer a good platform for investigating and improving thermoelectric performance

It has been shown by many research reports, that metal-chalcogenides-based thermoelectric materials possess excellent performance [57]. For example, a *ZT* of 2.6 was obtained at 923 K for a single crystal of SnSe; [58] and Na doped full scale-structured PbTe synthesized under high pressure exhibited a zT of 1.7 achieved at 750 K [59].

1.3.5. High entropy alloys

HEAs are defined as alloys constituted of at least 5 different elements in equimolar or close to equimolar amounts [32]. Each principal element should have a concentration between5 to 35%. Besides principal elements, HEAs can contain minor elements, each below 5%. These alloys are named 'HEAs' because their liquid or random solid solution state have significantly higher mixing entropies than those in conventional alloys. Thus, the effect of entropy is much more noticeable in HEAs.

Binary/ternary phase diagrams mention that such multi-element alloys may develop several kinds of phases and intermetallic compounds, resulting in complex and brittle microstructures that are difficult to investigate and engineer, and probably have very limited practical value. Differing to these, however, experimental results show the higher mixing entropy in HEAs

enables the formation of a solid solution phase with simple structures, and thus reduce the number of phases. A phase said to be simple if the structure is resulting from BCC, FCC, or HCP structures. Such characters, made available by the higher entropy, are of principal importance to the advance and application of these alloys.

High entropy alloys (HEAs) have been proposed as novel types of alloys with many interesting structural and functional properties. HEAs also have other excellent properties, such as excellent wear resistance, high-temperature performance, fracture toughness, corrosion and irradiation resistance, high hardness, as well as very high resistivity, good soft magnetic properties, which are the potential materials under extreme conditions [34].

As a rule, $K_{latt's}$ reduction is a vital stage on the road to a high zT of a TE material. This most of the time it needs the use of three key approaches: 1st, the scattering of phonons on the atomic length through fast atoms, impurities, vacancies, substitutional, or interstitials atoms
(all connected to point defect in a material); 2nd, the theory of "phonon glass electron crystal" ($PGEC$) should ideally be fulfilled, i.e., phonons are scattered by disorder in the crystal structure, whereas electron moves freely as in an electron crystal; and 3rd, through interfaces, for instance; mesoscale grain and phase boundaries.

In high entropy alloys, all of the phonon mentioned above, scattering approaches can, in principle, be attained concurrently through the intrinsically complex nature of the materials. In general, HEAs compromise a large amount of complexity through point defects, sever lattice distortions, or the second phase's precipitation to scatter phonon effectively, whereas keeping high mobility of the conduction electrons. As well as effective means for phonon scattering. HEAs have mostly high symmetry crystal structure, for face centre cubic close packing (FCC) or body-centred cubic close packing (BCC), or in some case hexagonal cubic close packing

(HCP). Thus, they are also likely to achieve a high convergence of the bands close to the fermi level to obtain high Seebeck coefficient values [35].

HEAs have a high degree of disorder in its atomic arrangement, resulting in the enhanced scattering of phonon and effectively reducing its lattice thermal conductivity. Polycrystalline high entropy $PbSnTeSe$ alloys with a slight addition of La in place of Pb were prepared by melting, followed by spark plasma sintering (SPS). The base $PbSnTeSe$ HEA undergo very low thermal conductivity at low temperature, for example, less than 0.6Wm^{-1} K^{-1}at 300 K. The minor compositional change not only improved both the Seebeck coefficient and electrical conductivity of the PbSnTeSe HEA at high temperatures but also improved it`s bipolar thermal conductivity to some degree, resulting in the improvement in the maximum zT value. When $PbSnTeSe$ HEA is doped with 1.5% La, its zT value was found to be about
0.8 at 873 K. The power factor PF is about 12.6×10^{-4} $Wm{-}1$ K^{-2} in the temperature range of 823–873K for alloy 1.5 La and Seebeck coefficient of alloy 0.5 La is around 180 μV/K at 873 K [33].

The other HEAs within the $AlxCoCrFeNi$ system ($0 \leq x \leq 3$) have been explored for TE properties in the temperature range of 100-900 ^{0}C. They found that the addition of Al improves the TE properties through an increase in the maximum absolute value of the Seebeck coefficient (~ 1 μV K^{-1} for x = 0 to ~ 23 μV K^{-1} for x = 3), and a simultaneous decrease in the electrical conductivity (from ~ 0.85 MS m^{-1} for $x = 0$ to ~ 0.36 for x = 3). The thermal conductivity is also decreased from ~ 15W $m^{-1}K^{-1}$ = 0 to ~12.5-13W $m^{-1}K^{-1}$ for x = 2.25 and 3, which is indicative of the lower electrical contribution (ke), to the total thermal conductivity. This is also showed in the ratio between the electrical and lattice thermal conductivity (k_e/k_{latt}), which decreases to unity for Al content (i.e., x = 2.5, 2.75, and 3). Furthermore, it is found that the investigated compositions reach a ZT ~ 0.015 for x= 2.0 and 2.25 at T = 505 ^{0}C, which was the upper limit for their thermal conductivity measurements [32].

1.4. References

1. Polozine, A., S. Sirotinskaya, and L.r. Schaeffer, *History of the development of thermoelectric materials for electric power generation and criteria of their quality.* Materials Research. **17**: p. 1260-1267.

2. Ponnamma, D., et al., *12 - Piezo- and Thermoelectric Materials From Biopolymer Composites*, in *Biopolymer Composites in Electronics*, Elsevier. p. 333-352.

3. Rademann, K., et al., *Chapter 3 - Crystallization and Growth Mechanisms of Nanostructures in Silicate Glass: From Complete Characterization Toward Applications*, in *Glass Nanocomposites*, William Andrew Publishing: Boston. p. 89114.

4. Sirusi, A.A., J.H. Ross, and G.A. Webb, *Chapter Three - Recent NMR Studies of Thermoelectric Materials*, in *Annual Reports on NMR Spectroscopy*, Academic Press. p. 137-198.

5. Xiao Zhang, L.-D.Z.L.-D., *Thermoelectric materials: energy conversion between heat and electricity.* Journal of Materiomics, 2015.

6. Zhang, H.a.D.V.T., Thermoelectric Tin Selenide: The Beauty of Simplicity. Angewandte Chemie International Edition. 53(35): p. 9126-9127.

7. Li JF, L.W., Zhao LD, Zhou M. Npg . High-performance nanostructured thermoelectric materials. 2010. 2(Asia Materials): p. 152-8.

8. Chen, G., et al., *Recent developments in thermoelectric materials.* International Materials Reviews, 2003. **48**(1): p. 45-66.

9. Dresselhaus, M., et al., *New Directions for Lowâ€•Dimensional Thermoelectric Materials.* Advanced Materials, 2007. **19**: p. 1043-1053.

10. Rull-Bravo, M., et al., *Skutterudites as thermoelectric materials: revisited.* RSC Advances. **5**(52): p. 41653-41667.

11. Yin, Y., B. Tudu, and A. Tiwari, *Recent advances in oxide thermoelectric materials and modules.* Vacuum. **146**: p. 356-374.

12. Iversen, B.B., et al., *Why are Clathrates Good Candidates for Thermoelectric Materials?* Journal of Solid State Chemistry, 2000. **149**(2): p. 455-458.

13. Liu, K.-F. and S.-Q. Xia, *Recent progress on thermoelectric Zintl phases: Structures, materials and optimization.* Journal of Solid State Chemistry. **270**: p. 252-264.

14. Huang, L., et al. *Recent progress in half-Heusler thermoelectric materials.* Materials Research Bulletin. **76**: p. 107-112.

15. Ghosez, P., *First-principles study of the dielectric and dynamical properties of barium titanate.* Ph.D. Thesis, Universite Catholique de Louvain, 1997.

16. S. Krishnamurthy, A.S., A.-B. Chen, 1026, Phys. Rev. B 33(2), (1986).

17. Zhao, L.-D., V.P. Dravid, and M.G. Kanatzidis, *The panoscopic approach to highperformance thermoelectrics.* Energy & Environmental Science, 2014. **7**(1): p. 251268.

18. Jiaqing He, M.G.K.a.V.P.D., *High-performance bulk thermoelectrics via a panoscopic approach.* Materials Today, May 2013. **Volume 16, Number 5**

19. N. M. Ravindra, B.J., Asahel Bañobre, Aniket Maske - *Thermoelectrics Fundamentals, Materials Selection, Properties, and Performance*. SpringerBriefs in Materials. 2019: Springer International Publishing.

20. Levin, E.M., *Charge carrier effective mass and concentration derived from a combination of*

Seebeck coefficient and 125Te NMR measurements in complex tellurides. 2016.

21. Pei, Y., et al., *Low effective mass leading to high thermoelectric performance.* Energy & Environmental Science. **5**(7): p. 7963-7969.

22. J, B.A.V.S., *Deformation Potentials and Mobilities in Non-Polar Crystals.* PHYSICAL REVIEW, 1950. VOLUME 80, NUMBER 1.

23. Rowe, D.M., *CRC Handbook of Thermoelectrics* 1995.

24. Cahill, D.G., Watson, S. K. & Pohl, R. O. Phys. Rev. B and 46.

25. Slack, G.A., *CRC Handbook of Thermoelectrics.* 1995 p. p. 407.

26. Bhandari, *C. M., in CRC Handbook of Thermoelectrics (ed. Rowe, D. M.).* 1995: p. 55–65.

27. Slack, G.A., *Proceedings of the 1992 1st National Thermogenic*

Cooler Conference. 1992: p. 171-195.

28. Tani, J.-i. and H. Kido, *Thermoelectric properties of Bi-doped Mg2Si semiconductors.* Physica B: Condensed Matter, 2005. **364**(1): p. 218-224.

29. M. Dehkordi, A., et al., *Thermoelectric power factor: Enhancement mechanisms and strategies for higher performance thermoelectric materials.* Materials Science and Engineering R Reports. **97**: p. 1-22.

30. Vashaee, D. and A. Shakouri, *Improved Thermoelectric Power Factor in Metal-Based Superlattices.* Physical review letters, 2004. **92**(10): p. 106103.

31. Wang, X.-y., et al., *The Thermoelectric Performance of Sb2Te3-based Alloy is Improved by Introducing PN Junctions.* ACS Applied Materials & Interfaces. **10**.

32. shafeie, J.A.P., 184905, (2015).

33. Wang, H., et al., Thermoelectric performance of PbSnTeSe high-entropy alloys AU - Fan, Zhao. Materials Research Letters. 5(3): p. 187-194.

34. Weiran Zhang, P.K.L.a.Y.Z., Science and technology in high-entropy alloys. SCIENCE CHINA Materials, 2018.

35. Y. Pei, X.S., A. LaLonde, H. Wang, L. Chen, and G. J. Snyder, Nature 473, 2011. 66.

36. Guo, J.Q., et al., *Development of Skutterudite Thermoelectric Materials and Modules.* Journal of Electronic Materials. **41**(6): p. 1036-1042.

37. Rogl, G. and P. Rogl, *Skutterudites, a most promising group of thermoelectric materials.* Current Opinion in Green and Sustainable Chemistry. **4**.

38. G.S. Nolas, J.S., H.J Goldsmid, *Thermoelectric: Basics principle and New Material Developments.* Springer, Berlin p. p.177.

39. Cahill, D.G., S.K. Watson, and R.O. Pohl, *Lower limit to the thermal conductivity of disordered crystals.* Physical Review, B, 1992. **46**(10): p. 6131-6140.

40. Shi, X., et al., *Multiple-Filled Skutterudites: High Thermoelectric Figure of Merit through Separately Optimizing Electrical and Thermal Transports.* Journal of the American Chemical Society. **133**(20): p. 7837-7846.

41. Sales, B.C. et al., *Filled skutterudite antimonides:â€fElectron crystals and phonon glasses.* Physical Review, B, 1997. **56**(23): p. 15081-15089.

42. Tang, X.F., et al., *Synthesis and thermoelectric properties of filled skutterudite compounds CeyFexCo4âˆ'xSb12 by solid-state reaction.* Journal of Materials Science, 2001. **36**(22): p. 5435-5439.

43. Su, X., et al., *Microstructure and thermoelectric properties of CoSb2.75Ge0.25âˆ'xTex prepared by rapid solidification.* Acta Materialia. **60**(8): p. 3536-3544.

44. He, J., Y. Liu, and R. Funahashi, *Oxide Thermoelectrics: The Challenges, Progress, and Outlook.* Journal of Materials Research. **26**: p. 1762-1772.

45. Terasaki, I., Y. Sasago, and K. Uchinokura, *Large thermoelectric power in single crystals.* Physical Review, B, 1997. **56**(20): p. R12685-R12687.

46. Yakabe, H., et al. *Thermoelectric properties of transition-metal oxide NaCo₂O₄ system*. in *Thermoelectrics, 1997. Proceedings ICT '97. XVI International Conference on*. 1997.

47. MartÃ-n-GonzÃ¡lez, M., O. Caballero-Calero, and P. DÃ-az-Chao, *Nanoengineering thermoelectrics for 21st century: Energy harvesting and other trends in the field.* Renewable and Sustainable Energy Reviews. **24**: p. 288-305.

48. Zhu, T., et al., *High-Efficiency Half-Heusler Thermoelectric Materials for Energy Harvesting.* Advanced Energy Materials. **5**.

49. Casper, F., et al., *Half-Heusler compounds: Novel materials for energy and spintronic applications.* Semiconductor Science and Technology - SEMICOND SCI TECHNOL. **27**.

50. Momma, K. and F. Izumi, *VESTA: a three-dimensional visualization system for electronic and structural analysis.* Journal of Applied Crystallography, 2008. **41**(3): p. 653-658.

51. Anand, S., et al., *A valence balanced rule for discovery of 18-electron half-Heuslers with defects.* Energy & Environmental Science. **11**(6): p. 1480-1488.

52. Cook, B.A., et al. *High-temperature thermoelectric properties of MNiSn (M=Zr, Hf)*. in *Thermoelectrics, 1999. Eighteenth International Conference on*. 1999.

53. Uher, C., et al., *Transport properties of pure and doped MNiSn (M=Zr, Hf).* Physical Review B, 1999. **59**(13): p. 8615-8621.

54. Kimura, Y., A. Zama, and Y. Mishima. *Thermoelectric Properties of P-type HalfHeusler Compounds HfPtSn and ZrPtSn*. in *Thermoelectrics, 2006. ICT '06. 25th International Conference on*. 2006.

55. Muta, H., et al., *High-temperature thermoelectric properties of Nb-doped MNiSn (M = Ti, Zr) half-Heusler compound.* Journal of Alloys and Compounds, 2009. **469**(1â€“2): p. 50-55.

56. Ono, Y., et al. *Thermoelectric Properties of NbCoSn-based Half-Heusler Alloys*. In *Thermoelectrics, 2006. ICT '06. 25th International Conference on*. 2006.

57. Chao, H., et al., *Thermoelectric Enhancement of Different Kinds of Metal Chalcogenides.* Advanced Energy Materials: p. 1600498.

58. Zhao, L., et al., *Ultralow Thermal Conductivity and High Thermoelectric Figure of Merit in SnSe Crystals.* Nature. **508**: p. 373-7.

59. Cai, B. et al., *Enhanced thermoelectric performance of Na-doped PbTe synthesized under high pressure.* Science in China Materials.

CHAPTER TWO

2. Statement of the Problem, Scope and experimental methods

2.1 Introduction

This chapter contains a detail of the problem; the scope, experimental procedures; an overview of the methods, instrument, and techniques used for this work. The instruments include X-Ray diffractometer, Scanning Electron Microscopy (SEM), Electron Probe Micro Analyzer (EPMA), Seebeck and resistivity machine. The sample preparation techniques used for this work are also described in this chapter. The sample preparation method mainly includes solid-state synthesis, directional solidification, cutting sample in both transverse and longitudinal direction, surface preparation, etc.

This work has been conducted using Cu, Sb, and Te as reagents. All are more than 99.9 at% pure, elemental chunk, and granules. The pseudo-binary phase diagram, shown in figure 1.6, was considered to select the compositions for this study. Accordingly, some compositions are taken from the Cu-Sb-Te side of the phase diagram. These samples are aimed to conduct two different experiments. The former focuses on the Effect of unidirectional solidification on the microstructure and thermoelectric power factor of Cu_2Te-Sb_2Te_3 pseudo-binary alloys while the latter focus on the effect of processing root change in the microstructure and thermoelectric property. The detail of these experiments has been discussed in the next chapters.

2.2 Sample Preparation Techniques

2.2.1 Ingot Formation

The stoichiometric amount of metallic elements Cu, Sb, and Te were weighed and filled into a one-sided closed quartz tube at one end and evacuated. Sealing the quartz tube ends was performed after softening by applying the hot flame which is a mixture of burning acetylene and oxygen. In a quartz tube, the mixture is sealed under very low pressure, about 10^{-5} atm. Then the metallic elements were then induction melted. For Directionally Solidified samples,

a modified-Bridgman type furnace was used to melt the samples at 900 K. And for Brine Quenching, with the help of hand LPG (propane) flame, the alloy in quartz tube were remelted repeatedly for better homogenization and rapidly quenching in a brine solution, and it has been shacked repeatedly to ensure homogeneous distribution of the elements. The sealed tube was kept in an upright position in both the melting process. Generally, two cooling processes are included in this work. These are furnace cooling and rapid ice water quenching.

2.2.2 Surface Preparation

Microscopy needs surface preparation of the sample. The transverse and longitudinal direction cross-sections were taken for directionally solidified alloys, and one side of the cross-section was taken for this purpose. Once the ingot has been cut, each piece had been mounted by mounting resin, for comfortable handling. The target surface is polished by different grid polishing papers (sandpapers). 8 to 2-micron meter diamond past and Al_2O_3 was used for polishing, as a second step. Thirdly silica suspension was used for polishing fine scratches. After polishing, the silica suspension was cleaned from the surface of the sample by distilled water in a sonication machine for 15-30 minutes and then dried by hot blowing air, using a hair drier. Since the resin, we use for mounting is a polymer, it is non-conductor. So we cover that area with carbon tape without covering our sample. Aluminium foil was used to avoid charging the sample by the applied electron beam during characterization by electron microscopy. To prevent contamination of the samples by dust, the samples had been kept in a roughly evacuated desiccator.

2.2.3 Directional solidification

Directional solidification is the basic principle of controlled solidification of a melt, having the greatest significance in metallurgical casting. The growth of single crystals by melting a charge in a crucible and freezing the melt from one end (seed) to the other (tail) has been used for many materials for a long time. However, the strong interaction of the growing crystal with

the crucible material limits the yield, and hence the industrial applicability is limited to only certain cases. The method can be carried out by moving the growth interface in a horizontal or a vertical direction. The crystal growth configuration consists typically of a tube furnace which provides a temperature profile with negative gradients parallel to the growth direction (at least in the vicinity of the growth interface but mainly in the major portion of the melt and crystal). The single-crystal seed is positioned at one end of the boat or the lower end of the vertical crucible (see Fig. 2). (Crystal Growth from the Melt)

The use of processes to control the solidification direction may cause micro and even in some extreme cases macro-segregation on the obtained castings. (Wang et al., 2004).

2.3 Characterization Techniques

2.3.1 X-Ray Diffractometer

X-ray diffraction (XRD) is the most important analytical high-tech non-destructive technique for characterizing a wide range of materials including fluids, metals, minerals, polymers, catalysts, plastics, pharmaceuticals, thin-film coatings, ceramics, solar cells, and semiconductors. X-ray diffraction (XRD) crystallography for powder samples is familiar and commonly used in the field of materials characterization to get information on the atomic scale structure of numerous substances in different states. It provides information on structures, preferred crystal orientations (texture), phases, and other structural parameters, such as average grain size, strain, crystallinity, and crystal defects. X-ray diffraction peaks are formed by constructive interference of a monochromatic beam of X-rays scattered at particular angles from each set of lattice planes in the sample. The peak intensity is determined by the distribution of atoms inside the lattice. Consequently, the X-ray diffraction pattern is the pattern of periodic atomic arrangements in a given material.

Max von Laue and Co., in 1912, discovered that crystalline substance act as a threedimensional diffraction grating for X-ray wavelengths similar to the spacing of planes in a crystal lattice

[1]. X-ray diffraction is currently a common technique for the study of atomic spacing and crystal structures. X-ray diffraction is working on a crystalline sample and based on the constructive interference of a monochromatic X-rays. These X-rays are produced by cathode ray tubes (CRT), next filtered to produce monochromatic radiation, collimated to concentrate, and directed toward the sample. For a given crystalline sample to generate an Xray pattern, the interaction of the incident rays with the sample will produce diffracted rays, and this ray will only create constructive interference when conditions satisfy Bragg's low.

$$n\lambda = 2d_{hkl}\sin\theta$$

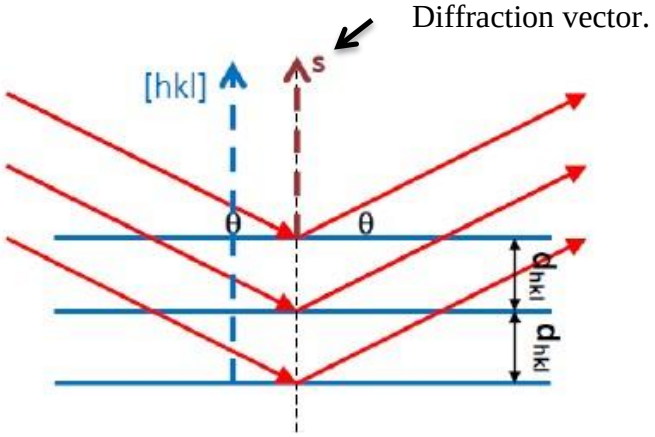

Fig. 2.1. Bragg`s law [1]

Where n is an integer, λ is the wavelength of the incident X-rays, d is the interplanar spacing generating the diffraction, and u is the diffraction angle. Bragg`s law interconnects the wavelength of electromagnetic radiation to the lattice spacing and the diffraction angle in the crystalline sample. These diffracted X-rays are then detected, processed, and calculated.

When the crystalline sample is scanned through a range of 2θ˚angles ($5 \leq \theta \leq 140$), all possible diffraction direction of the lattice should be achieved due to the random orientation of the powdered material. Changing the diffraction peaks to d spacing enables the identification of the compound because each compound has a set of assigned unique d spacing. Usually, this is attained by comparison of compound X-ray d spacing with standard reference patterns. X-ray

diffractometer comprises three basic elements: an X-ray tubes, sample holders, and X-ray detector [2].

In a cathode ray tube (CRT), X-rays are generated by heating a filament to produce electrons, accelerating the electrons on the way to a target by applying the target, and bombarding the target sample with electrons. When the bombarded electrons have adequate energy to take out inner shell electrons of the target sample, characteristic X-ray spectra lines are produced. These lines fall into several sets, referred to as K, L, M, etc., in the order of increasing wavelength, all the lines together forming the characteristic spectrum of the metal used as the target (Mo, Cu, Co, Fe, Cr), the most common characteristic X-ray spectra lines are Kα and Kβ. Kα consists of Kα1 and Kα2. Kα1 has a somewhat shorter wavelength and double the intensity of Kα2. Filtering by crystal monochromators or foils is required to produce monochromatic X-rays necessary for diffraction. Kα1 and Kα2 are sufficiently close in wavelength to one another such that an average of the two is used. Copper is the most communal target material for single crystal diffraction, with Cu Kα radiation $\lambda = 1.5418$ Å.

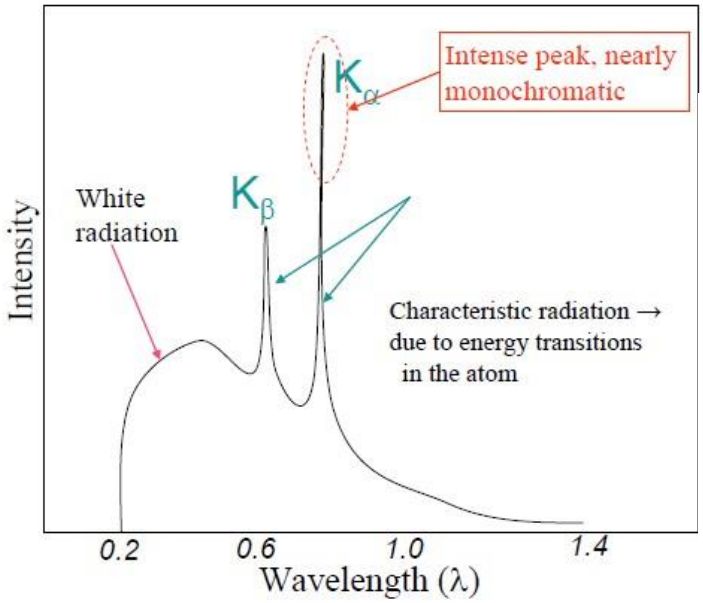

X-ray sources with different λ for doing XRD studies

Target Metal	λ Of K_α radiation (Å)
Mo	0.71
Cu	1.54
Co	1.79
Fe	1.94
Cr	2.29

Fig. 2.2. The characteristic spectrum of the copper [3]

. These X-rays are parallel and directed onto the sample. As the detector and sample are rotated, the intensity of the reflected X-rays is recorded on a computer. When the geometry of the incident X-rays striking the sample satisfies Bragg`s law, constructive interference occurs, and a peak in intensity appears [4].

A detector registers and processes this X-ray signal and converts it to a count rate, which is then output to a printer or a computer monitor.

For the sample to characterize the sample rotates in the path of the collimated X-at the angle θ though the X-ray detector mounted on the opposite side arm to collect the diffracted X-ray and rotate the angle of 2θ. The instrument used to sustain the angle and then rotate the sample is called a goniometer.

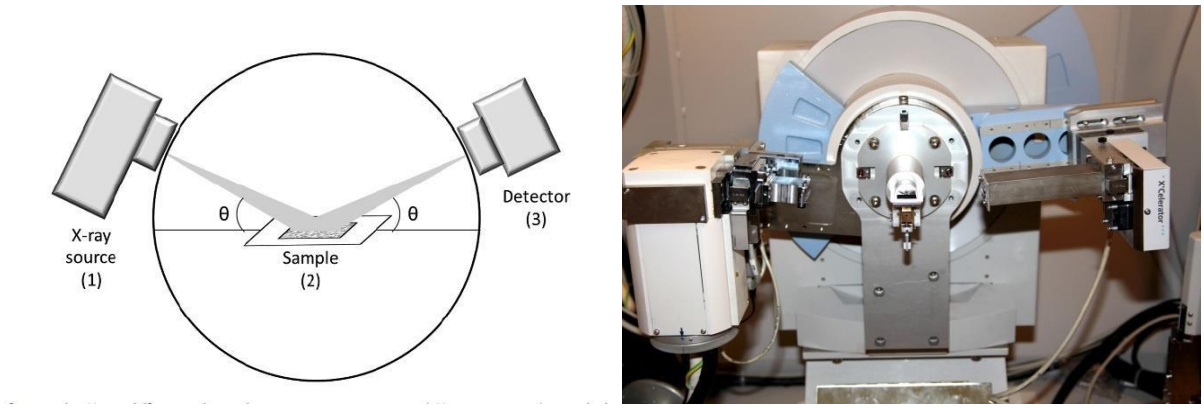

Fig. 2.3. Schematic [2] and Instruments [5] for powder X-ray diffraction

For powder patterns, data are collected at 2θ from 5 to 80, angles that are present in the X-ray scan. X-ray powder diffraction is most commonly used for the identification of unknown crystalline materials (for instance: inorganic compounds, minerals). Determination of unknown crystalline materials is vital to studying material science, environmental science, engineering, biology, and geology. Additional uses include determining phase composition of a sample, residual strain, crystal structure/texture/orientation, crystallite size and microstrain, determination of unit cell dimensions, and measurement of sample purity.

With specialized techniques, X-ray diffraction (XRD) can be used to determine crystal structures, volume and density by using Rietveld refinement, determine modal amounts of minerals (quantitative analysis), characterize thin film samples, and make texture measurement, for example, the orientation of grains in polycrystalline samples [6].

2.3.1.1 Sample Preparation

Appropriate sample preparation is one of the most important requirements in the analysis of powder samples by X-ray diffraction. Sample preparation contains the right sample treatments to eliminate unwanted substances and proper techniques to obtain looked-for particle size, orientation, thickness, and other parameters.

Analysis of powder samples by X-yay diffraction requires that they are extremely fine-grained to achieve good signal-to-noise ratio and avoid fluctuation in intensity, spottiness, and

minimize favoured orientation. The reduction of powders to fine particles also guarantees enough particles involvement in the diffraction progressions. The suggested size range is about 1-5 mm [4, 7], particularly if the quantification of numerous phases is desired.

For predictable qualitative development of mineral components, the samples are typically grounded to pass through a 325-mesh sieve (45 mm). Grinding is accomplished either through hand grinding with mortar and pistil or in a mechanical grinder. The effects of unnecessary grinding lead to lattice distortion and the possible formation of an amorphous layer (Beilby layer) outside the grains.

2.3.2 Microscopy

2.3.2.1 Scanning Electron Microscopy (SEM)

The scanning electron microscopy (SEM is one of the most multipurpose devices accessible for examining the chemical composition and microstructure morphology characterization. It is essential to know the basic principle of light optics to understand the fundamentals of electron microscopy.

A scanning electron microscope uses a superbly focused beam of electrons to bring out the detailed surface characteristics of a sample and provide information associate with its three-dimensional structure. It also has a specific advantage of providing a great depth of field. Starting the first commercial instruments in the mid-1960s, the scanning electron microscope provided the connection between the magnification ranges offered by light microscopy and the higher resolving capability of the transmission electron microscope (TEM). At present, following the development of electromagnetic lens systems, vacuum systems, and electron guns, the SEM scan has a 1 nm resolution. So, there is no substantial overlap between the resolving power of the two forms of electron microscope available, although the techniques are complementary and different types of microstructural information are obtained in each case [8].

2.3.2.1.1 Configuration of SEM

The electron gun produces the electrons and accelerates them to an energy level of 0.1-30 keV. The diameter of an electron beam produced by a hairpin tungsten gun is too large to form a high-resolution image. Therefore, apertures and electromagnetic lenses are used to define and focus the electron beam on a small, focused electron on the samples. This process demagnifies the size of electron sources (a tungsten filament ~50 μm) to the final necessary spot size (1-100 nm). During this process, a high-vacuum environment, which allows electron travel without scattering by the air, is needed. The sample stage, electron beam scanning coil, signal detection, and processing systems gives real-time observation and image recording of the sample surfaces [9].

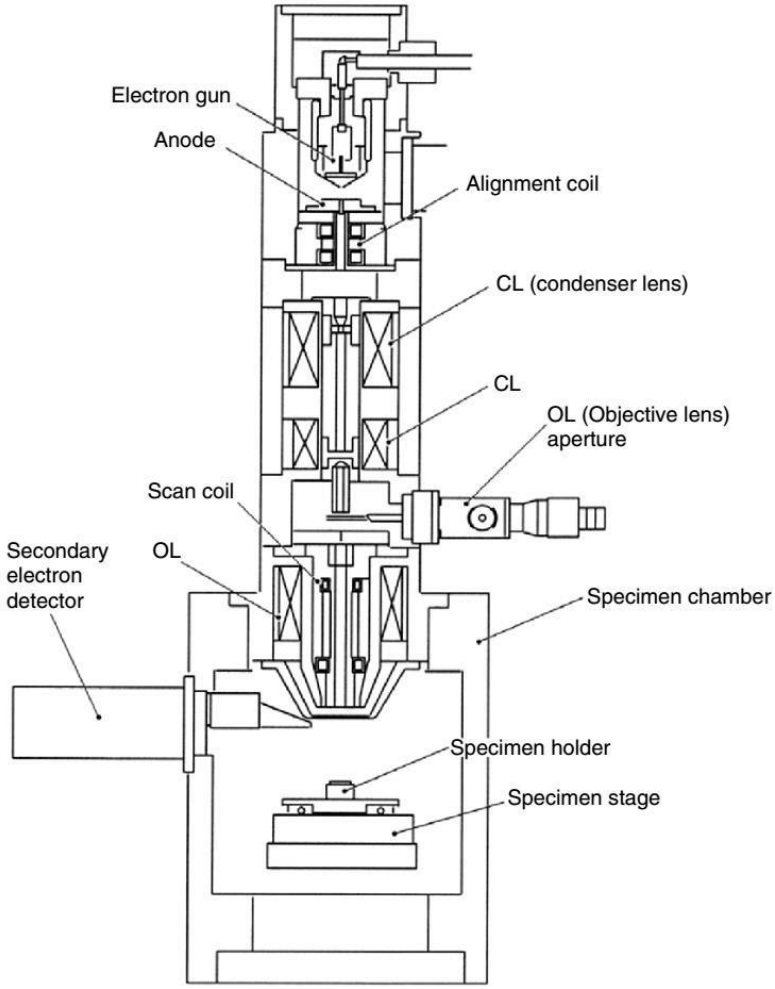

Fig. 2.4. Schematic diagram of a scanning electron microscope (SEM) (JSM-5410, courtesy of JEOL, USA) [9].

Electron Guns

Present SEM systems need the electron gun to produce a steady electron beam with high current, adjustable energy, small spot size, and small energy dispersion. Numerous types of electron guns are used in the SEM system, and the electrons beam they produced qualities vary considerably. The first SEM systems generally used Tungsten "hairpin" or lanthanum hexaboride (LaB_6) cathodes, which provides ease of operation, low cost, and simplicity. But for the present SEMs, the trend is to use field emission sources, which provide lower energy dispersion and improved current. Emitter lifetime is another important consideration for the selection of electron sources.

Electron Lenses

Electron beams can be focused by a magnetic or an electrostatic field. However, an electron beam controlled by the magnetic field has a smaller abrasion. Therefore the only magnetic field is employed in the SEM system. Coils of wire, known as "electromagnets," are used to produce a magnetic field, and the paths of the electron can be attuned by the current applied on these coils. The electron lenses can be used to magnify or demagnify the electron beam diameter, because their strength is variable, which results in a variable focal length.

Condenser lenses

The electron beam will deviate after passing through the anode plate from the emission source. By using condenser lenses, the electron beam is converged and collimated into a comparatively parallel stream. The position of the focal point can be controlled by adjusting the condenser lens current. For modern electron microscopes, a second condenser lens is often used to provide additional control on the electron beam.

Objective lenses

The electron beam will diverge under the condenser aperture. Objective lenses are used to focus the electron beam into a probe point at the sample surface and to provide further demagnification. A suitable choice of lens demagnification and aperture size results in a reduction of the diameter of an electron beam on the specimen surface (spot size) and enhance the image resolution.

2.3.2.1.2 SEM working Principles

When a fine beam of electrons is focused on to the surface of a sample, different interactions occur, including the emission of secondary electrons (SE) and backscattered primary electrons (BSE). If these are collected and amplified, they can be used to create an image corresponding

to the sample's surface topography. The electron beam is scanned across the sample recurrently in a raster pattern, which is synchronized with the scan of a cathode ray tube such that the image is presented in a digitized form built upon a computer monitor.

As with transmission electron microscopes, conventional instruments must be operated under a high vacuum so that the electron beam can travel to the sample surface without collision with gas molecules [8].

2.3.2.1.3 Sample Preparation

Cutting: Saw equipment for sample precision cutting to obtain dimensions limited by support table disposed inside the sample chamber.

Mechanical polishing: Polishing by using special waterproof fine-grain grinding papers and using special velvet tissue immersed by diamond paste or water suspension of Al_2O_3. Any traces of scratches must be removed. The specimen surface must be brilliant.

Etching: Etching is the last operation necessary for microstructure visualization. It is realized by application chemical reagent on the surface of a polished specimen.

Mounting: Samples are embedded at epoxy resin for better mounting on the holder called sample stub and correction of sample quality before mounting samples must be cleaned, free of dust, grease, and any impurities.

Sample coating: Samples analyzed by SEM methods must conduct electrical current. If the sample doesn't conduct electrical current, they must be coated with a thin layer

, i.e., 20nm-30 nm of conductive metal of Au, Pt, W, Cr, C, or Cu. Sample coating is anticipated to prevent charge-up occurrence by letting the charge on the sample surface goes to ground through the coated conductive film.

Sample Labelling: The SEM sample must be properly labelled. It is hardly possible to label the sample directly; however, this method can be achieved with a permanent marker on the undesired of a metal sample.

2.3.2.2 Electron Probe Micro Analyser (EPMA)

The Electron Probe Micro Analyser "EPMA" is an instrument to analyse which elements compose a substance by irradiating electron beams onto the substance surface and measuring the characteristic X-ray generated. It gives a detailed image of the sample with nondestructive in situ chemical analysis.

EPMA was developed and presented by Dr Castaing of France in his academic dissertation in 1951. EPMA today is playing an active role worldwide, as a multi-purpose, multi-functional tool equipped with electron optics technology. EPMA has evolved into an instrument that can handle the elemental analysis of sub-micron areas as well as observation, examination, and image analysis for areas as large as 10 cm^2.

This apparatus is used for basic research in a devise range of fields, such as minerals, steels, ceramics, semiconductors, medical and dental materials, textiles, biology, and applied research and product quality management [18].

EPMA works by bombarding a micro-volume of a sample with a focused electron beam and collecting the X-ray photons in that way emitted by various elemental species. Since the wavelength of these X-rays is typical of the emitting species, the sample's composition can be simply known by recording WDS (Wavelength Dispersive Spectroscopy) spectra. WDS spectrometers function based on Bragg's law and use numerous moveable, shaped monocrystals as monochromators.

2.3.2.2.1 Mechanism of instrument

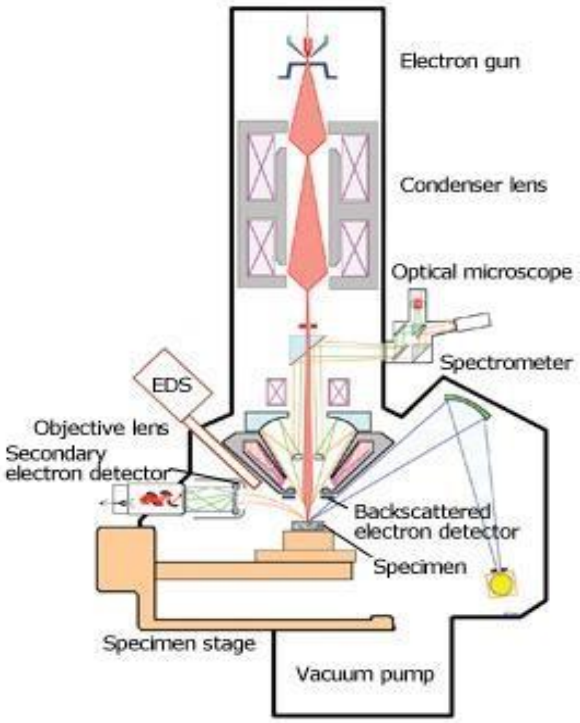

Fig. 2.5. The structure of an EPMA device [18].

Electrons emitted by electron gun are accelerated at a definite accelerating voltage and collimated through electron lenses. Once this electron beam hits the sample, an X-ray is produced from the sample. By scattering this X-ray using a dispersive element, the composition of a sample can be studied. This type of spectrometer is known as a wavelength dispersive spectrometer (WDS) [19].

- EPMA is a qualitative and quantitative technique of non-distractive elemental analysis of micro-sized volumes at the surface of materials, with sensitivity at PPM level. It is the most accurate micro-analysis method.
- EPMA is completely compatible with routine analysis sessions, with a simple and interpretation of the outcomes.

- EPMA devices are equipped with complete equipment of built-in microscopy tools that allow concurrent X-ray (EDS and WDS), BSE and SEM imaging, additionally complex visible light optics, they provide very flexible sample examination with image magnification ranging from 40 to 400,000.
- Determination of thickness and elemental composition from nm to mm thick layers in stratified materials is possible.

EPMA delivers a much better result than typical SEM/EDS systems. Since WDS's internal properties, the general sensitivity, analysis of light elements, and risks of a mistaken clarification of measurable spectra are all greater with EPMA. Spectra detector and resolution end time are much better than EDS. The excitation beam regulation system and complex sample stage abilities guarantee that this method provides outstanding constancy and measurement repeatability.

2.3.2.3 Seebeck coefficient and electrical conductivity measurements

Seebeck coefficient, also known as the thermopower, is usually measured by either a dc or ac technique. 12-14, the former represents one of the simplest transport measurements. It requires a thermal gradient to be established along with a sample and measuring both the thermoelectric voltage and the temperature difference between two points along the length of the sample [10].

During the measurement of the Seebeck coefficient and electrical conductivity of bulk thermoelectric materials, the sample holder was designed to have a dense structure that can be directly mounted in a standard cryostat system for temperature-dependent measurements. During the measurement of the Seebeck coefficient, a thin bar or cylinder-shaped sample is mounted joining the two copper bases, and two type thermocouples are connected to the in the middle of the sample to determine both temperature and voltage differences between two widely separated points on the sample. Two ceramics heater are used to generate a temperature

gradient along with the sample. The thermocouple intersection is flattened into a disk and pressed onto the sample surface by using spring load. The springy fixation technique we implemented simplifies the sample mounting process and avoids thermal contact deterioration because of the mismatch of thermal expansion coefficients among the sample holder and other parts [11].

A variety of approaches have been developed for measurements of the Seebeck coefficients, each with their advantage and disadvantage [12-14].

In general, methods for measuring the Seebeck coefficient can be divided into two categories: the two-probe scheme and the four-probe scheme. In the two-probe scheme, two metal blocks with embedded thermocouples are used to clamp the bulk sample and establish a temperature gradient across the sample. The temperature difference is determined on two metal blocks. In the four-probe scheme, the temperature gradient is also applied through two metal blocks, but the temperature difference is determined by directly attaching thermocouples onto two points on the sample. As mentioned by Rouleau and Alleno, the two-probe scheme neglects the effect of contact thermal resistance between the sample and metal blocks and therefore is only applicable for thick or block-shaped samples. For thin bar-shaped or cylindrical samples, the four-probe scheme is required since the contact thermal resistance is not negligible. The good thermal contact between the sample and thermocouples is crucial for an accurate Seebeck coefficient measurement [11].

ULVAC The thermal power, thermoelectric power, or Seebeck coefficient of a material measures the magnitude of an induced thermoelectric voltage in reply to a temperature difference across that material. The Seebeck coefficient has units of (V/K).

For Seebeck coefficient measurements, the general idea is to measure the voltage generated by the sample under a temperature gradient. Some key guidelines that are commonly followed during Seebeck coefficient measurements are listed below:

1) Voltage and temperature must be measured at the same locations and at the same time;

2) Excellent thermal (isothermal) and electrical (Ohmic) contacts must be maintained between the probes and the sample;

3) The measurement system must be stable, and noise from the measurement and data acquisition systems must be minimized as voltages generated in samples are typically in the range of a few μVs

For measurements of electrical resistivity, the four-point probe method is widely used for thermoelectric materials, not only to evaluate new high zT materials [15] but also to develop a Seebeck coefficient standard reference material [16]. Since the four-point probe method requires an axial current flow and precise dimensional measurements to apply the proper geometric correction factors [17], bar-shaped samples are the preferred geometrical shape with this technique. These measurement techniques exclude the influence of contact resistance and minimize the influence of the thermal emf arising from the Peltier effect. The latter effect is particularly difficult in thermoelectric materials, where the Peltier contribution can lead to serious errors in measurements of the electrical resistivity. Since the emf arising from the Peltier effect is of thermal origin, it takes a fraction of a second to develop in the sample. If the excitation current is reversed in a time shorter than the time needed to develop the Peltier-generated emf, the Peltier contribution can be effectively eliminated, and a purely ohmic signal can be measured [12].

2.3.2.3.1 Method

Usually, a sample of bar or cylindrical shape is vertically positioned in the middle of two electrodes. The lower electrode (or optional also the upper electrode) block for a temperature gradient inversion contains a heater, while the entire measuring arrangement is located in a furnace, which heats the sample to a specified temperature. On this temperature, the secondary heater in the lower electrode block generates a set of a temperature gradient. The two thermocouples $T1$ and $T2$ then measure the temperature differences ($\Delta T = T2 - T1$) between the sample's hot and cold sides. Also, one wire of each of the two thermocouples is used to measure the occurring electromotive force EMF and thermal voltage Vt, respectively. A unique spring-based thermocouple mechanism permits the best possible electric contacts, which gives the highest accuracy measurements. The Seebeck coefficient can easily be calculated from the obtained data.

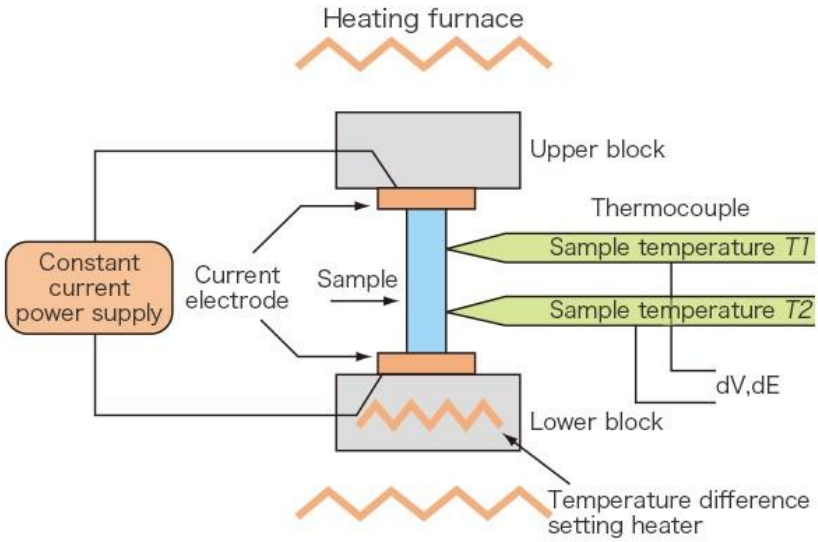

Fig. 2.6. Schematic diagram of the Seebeck coefficient and electrical resistivity measurement [17].

For the measurement of electrical resistance, the dc four-terminal method is used, which allows neglecting parasitic effects, like contact or wire resistances. For the measurement, a constant

current ($I\ dc$) is applied through the upper and lower electrode, and the corresponding voltage drop ($V\Omega$) along the sample is measured between one wire at each of the two thermocouples.

2.4 Scope

This research covers the effect of different processing root on transport properties and microstructure formed by the Cu-Sb-Te pseudo-binary system. The microstructural study will include researching the effect on the transport properties formed by directional solidification and brine quenching and induction melting. The thermoelectric property will be studied to examine the effect of this different processing root on Cu-Sb-Te. The research on the region of Cu_2Te-Sb_2Te_3 focuses on determining different microstructures which may have potential application for thermoelectric devices. The study of microstructure variation focuses on the effect of the composition, processing method, and solidification speed on the transport properties. The samples will be compared in terms of their thermoelectric properties.

2.5 General Objective

- ✓ Investigation of the effect of processing roots on the thermoelectric properties of the pseudo-binary system of Cu-Sb-Te for thermoelectric application.

2.6 Specific Objectives

- ✓ Synthesis of different thermodynamically stable phases of the pseudo-binary system of Cu-Sb-Te with different compositions and solidification speed (for the directional solidification sample).
- ✓ Characterize the microstructure of the synthesis pseudo-binary system of Cu-Sb-Te alloys.
- ✓ Measure thermoelectric transport properties of the synthesis pseudo-binary system of Cu-Sb-Te.

2.7 References

1. Eckert, M., *Max von Laue and the discovery of X-ray diffraction in 1912.* Annalen der Physik. **524**: p. 83-A85.
2. Bunaciu, A.A., E. UdriÅžTioiu, and H. Aboul-Enein, *X-Ray Diffraction: Instrumentation and Applications.* Critical reviews in analytical chemistry / CRC. **45**.
3. Deutsch, M., et al., *K alpha and K beta x-ray emission spectra of copper.* Physical review. A, 1995. **51**: p. 283-296.
4. CULLITY, B.D., & STOCK, S. R., Elements of x-ray diffraction. Upper Saddle River, NJ, Prentice-Hall. (2001): Harvard (18th ed.)
5. https://www.icsp.nat.fau.eu/philipspanalytical-xpert-pro-mpd-powder-diffractometer/.
6. GÃ¼ven, N., *Crystal Structures of Clay Minerals and Their X-ray Identification.* Clays and Clay Minerals, 1982. **30**(1): p. 80-80.
7. Alessi, D.S., et al., *X-ray Diffraction Techniques*, in *Analytical Geomicrobiology: A Handbook of Instrumental Techniques*, Cambridge University Press: Cambridge. p. 215-237.
8. Echlin, P., *Handbook of Sample Preparation for Scanning, Electron Microscopy and X-Ray Microanalysis*: Cambridge Analytical Microscopy, UK
9. Weilie Zhou, R.P.A., Zhong Lin Wang, and David Joy, *Fundamentals of Scanning, Electron Microscopy*.
10. Zhou, Z. and C. Uher, *Apparatus for Seebeck coefficient and electrical resistivity measurements of bulk thermoelectric materials at high temperature.* Review of Scientific Instruments, 2005. **76**: p. 023901-023901.
11. Qiang Fu, Y.X., Wenhua Zhang, and Dongyan Xua), *A setup for measuring the Seebeck coefficient and the electrical resistivity of bulk thermoelectric materials.* 2017.
12. C, Z.Z.a.U. and. *Apparatus for Seebeck coefficient and electrical resistivity measurements of bulk thermoelectric materials at high temperature.* Rev. Sci. Instrum, 2005. **76 1-5]**.
13. Iwanaga S, T.E.S., LaLonde A and Snyder G J *A high-temperature apparatus for measurement of the Seebeck coefficient* Rev Sci Instrum, 2011(82 63905).
14. Martin J, *Apparatus for the high-temperature measurement of the Seebeck coefficient in thermoelectric materials* Rev Sci Instrum, 2012. **83 65101**.
15. Korkosz R J, C.T.C., Lo S H, Doak J W, Kim Y J, Wu C I, Hatzikraniotis E, Hogan TP, Seidman D N, Wolverton C, Dravid V P and Kanatzidis M G 2014 High ZT in ptype (PbTe)1-2x(PbSe)x(PbS)x thermoelectric materials J Am Chem Soc 136 3225–37.
16. Lowhorn N D, W.-N.W., Lu Z-Q, Martin J, Green ML, Bonevich J E, Thomas E L, Dilley NR and Sharp J 2011 Development of a Seebeck coefficient Standard Reference MaterialTM J. Mater. Res. 26 1983–92.
17. J., S.F.M.M.o.S.R.w.t.F.-P.P.B.S.T.
18. Dennis, J.K. and T.E. Such, *Chapter 2 - Metallurgical aspects of electrodeposition*, in *Nickel and Chromium Plating (Third Edition)*, J.K. Dennis and T.E. Such, Editors. 1993, Woodhead Publishing. p. 13-40.
19. Kearns, S., *Electron Probe Microanalysis (EPMA)*, in *Encyclopedia of Geochemistry:* W.M. White, Editor. 2016, Springer International Publishing: Cham. p. 1-3.

CHAPTER THREE

3. Tuning the thermoelectric material transport properties: Case of unidirectionally solidified Cu_2Te-Sb_2Te_3 eutectic

3.1. Introduction:

In a recent year, many efforts have been made to improve the figure of merit zT value of thermoelectric materials, such as controlling the microstructure [1, 2] preparing nano composites [3, 4] and elemental doping [5]. Controlling microstructure, for the most part, influences the thermoelectric properties of the material. For instance, controlling the microstructure enhanced the thermoelectric properties of Bi_2S_3 polycrystalline. The fine grain size contributes to the large Seebeck coefficient and low thermal conductivity but leads to an increase in electrical conductivity. However, the coarse grain size contributes to low electrical resistivity but causes an increase in thermal conductivity. Although many works have been done to optimize grain size for improving the TE properties of bulk and film materials, they just find a suitable grain size which could optimize TE properties, and could not fully utilize the characteristics of fine and coarse grains [6-8]. To fully functionalize such dual effects of grain size, a high-performance TE material may need a good combination of coarse and fine grains in an individual material.

Some of the approaches for modification of the microstructure for changing these properties are solidification [9, 10], spinodal decomposition [11-13] as well as solid-state precipitations [14-17]. Among these, solidification can produce wide-range of microstructural features starting from amorphous to multiphase to single-crystal during liquid to solid transformation. During solidification, the temperature gradient across the solid-liquid interface and its growth velocity are the two important processing parameters which can influence the evolution of microstructure [18, 19]. The desired morphology can be attained by controlling the temperature gradient and velocity independently. Microstructural modifications through the control of

cooling rate to enhance the thermoelectric performance has gained attraction over the recent past [20-22]. However, these efforts are geared towards the reduction of the contribution of lattice thermal conductivity to the total thermal conductivity (κ) to enhance the thermoelectric figure of merit zT (where $zT= S^2\sigma/\kappa$). The enhancement of the thermoelectric power factor ($S^2\sigma$) can also significantly improve thermoelectric performance that may be equally important to that of the reduction of thermal conductivity [23-25]. The microstructural modification provides a mean for achieving this. For instance, the microstructure and the thermoelectric properties of the polycrystalline Bi_2Te_3-PbTe alloy which was prepared by spark plasma sintering of 90 nm size powders, were examined. The grain which has 200 nm numerous mm size were observed by SEM and TEM. The polycrystalline alloy consists of Pb-rich and Bi-rich regions with several nm sizes, which was identified by EDS. The polycrystalline alloy has the highest value of power factor of 4.30×10^{-4} W m^{-1} K^{-2}, and zT 0.39 at 473 K. The thermal conductivities were smaller than those of the Bi_2Te_3-PbTe ingot and the polycrystalline Bi_2Te_3. Thermal conductivity by phonon can be more decreased by the control of the microstructure of polycrystalline Bi_2Te_3-PbTe alloy. Therefore, in this work, we have developed unidirectional solidification to modify the microstructure in such a way that can improve the thermoelectric transport properties, S Seebeck coefficient, and σ is the electrical conductivity which collectively improves the power factor $S^2\sigma$.

Thermoelectric composites comprising of the two or more different phases show to improve the figure of merit zT as a result of the low lattice thermal conductivity. The low lattice thermal conductivity of composite material is typically expected to be related with the improved phonon scattering by meso / nanoscale interfaces, either heterophase interfaces or grain boundaries. This theory encouraged wide research on understanding the function of nanostructured and the synthesis of nanostructured thermoelectric materials. Among others, thin-film thermoelectric materials show a mainly of the high figure of merit zT. But, the

production of such materials often includes thin-film technologies with an inadequate production, which limits their particular applicability. It is highly wanted to produce materials with similar structures, but through bulk processing that permits obtainability in almost applicable large quantities. Lamellar eutectic structures are comparable to superlattice structures, but of enlarged layered thicknesses or distances and consequently, they are capable candidates.

The pseudobinary systems differ from the true binary ones by the presence of one or more phases with compositions lying outside those of the binary join, i.e., the compositions of all the phases cannot be expressed as a linear combination of the two end-member components. A p-type Sb_2Te_3 and n-type Ag_2Te composite have been achieved a high zT of 1.5 at 700K and a high power factor of 1.0 – 1.5 $mw^{-1}K^{-1}$ with a temperature inconsiderate behaviour over wide temperature range [26]. PbTe-Sb_2Te_3 pseudobinary alloy, which is prepared by rapid solidification and decomposition of the thermoelectric composite. The decomposition phase $Sb_2Te_3$and PbTe are highly originated respect to one another, characteristics typically epitaxial crystal growth, suggest the presence of clean, atomically precise interfaces. The presence of such interface with nanoscale superlattices may be critical for high performance nano-structured thermoelectric Sb_2Te_3 and PbTe. The composite is p-type with a Seebeck coefficient of 30 μV/K and electrical resistivity of $4*10^{-4}$Scm [27]. Recent research efforts have focused on decreasing the lattice thermal conductivity of these materials, without a concomitant reduction in their electrical conductivity, by using the phonon-glass–electron crystal approach.5 For example, Venkatasubramanian et al. were able to increase ZT to up to 2.5 by synthesizing a p-type Bi_2Te_3/Sb_2Te_3 superlattice structure through metal-organic chemical vapour deposition (MOCVD) [28]. Cao et al. developed Bi_2Te_3/Sb_2Te_3 nanocomposites using a hydrothermal synthesis method and hot pressing, achieving a maximum ZT of 1.476 [29].

Eutectics are common feature in many phase diagrams and have developed for various application [2, 18–26]. For instance, Cu2Te-Sb2Te3 [30], PbTe-Sb_2Te_3 [21, 31], PbTeBi2Te3 [32], PbTe-Si/Ge [33], PbTe-TeAg5Te3 [34], Ag_2Te-PbTe-Sb2Te3 [35], PbTe-MnTe [36], InSb-Sb [37], among others, have been studied mainly in the recent seven years.

At the current time, research on eutectic thermoelectric materials was mostly direct the course on randomly oriented eutectic structures. Bearing in mind that the constituent phase of a composite has different physical properties, the transport performance along the hetero-phase interface will be different from that across the interfaces, as e.g. theoretically predicted by models for physical properties of composite materials [38, 39] and shown by experimental observations [40]. This proposes that the thermoelectric properties of isotropic eutectics with randomly distributed interface orientations do not satisfactorily differentiate the effect of the interfaces from other factors. It is highly necessary to study the influence of microstructural features such as volume fractions, length scales and crystallographic orientation distribution independently.

During solidification of eutectic systems [41, 42], solid-phases self-organise themselves into characteristic spacing based on the solidification velocity and grow along the imposed temperature gradient. Such alignment of the eutectic phases along the temperature gradient causes anisotropy in the properties i.e. property along growth direction (longitudinal direction) is different concerning that along the perpendicular to growth direction (transverse direction). In case the constituent phases of the eutectic microstructure have different transport properties, such a variation will result in variable transport behaviour in the alloys with changes in the solidification rates as well as the growth directions [9]. Directional solidification with the well-defined orientation of eutectic lamellae is appropriate to separate crystal anisotropy from microstructural features. This can further help to enhance the thermoelectric performance of eutectic thermoelectric composites. This drives the motivation for the current work in which

we have studied the thermoelectric properties along growth direction as well as transverse direction by varying the solidification rates under a constant temperature gradient.

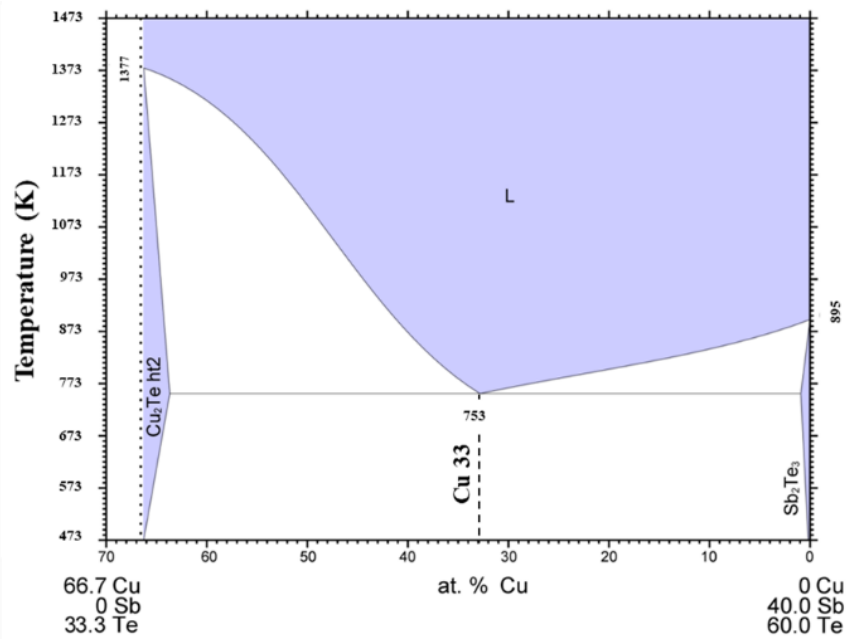

Fig.3.1: Pseudo-binary phase diagram of Cu_2Te-Sb_2Te_3 system [43]

The Cu_2Te-Sb_2Te_3 pseudo-binary phase diagram in Fig.3.1 shows the existence of a eutectic point at a copper concentration of Cu 33 at. % and temperature 753 K. We have chosen the composition $(Cu_2Te)_{62.02}$-$(Sb_2Te_3)_{37.98}$ of the eutectic alloy from this system. The metal Chalcogenides (S, Te, Se) have been attracting significant attention in a variety of energy harvesting applications including, solar cells, light-emitting diodes (LED), batteries, sensors, supercapacitor, thermoelectric devices … etc [44-46]. Compared with oxides, metal chalcogenides based thermoelectric materials possess high thermoelectric transport properties due to less covalent nature of their bonding, arising from their low electronegativity. Their heavier atomic weight, compared to some other thermoelectric materials, is beneficial for reducing thermal conductivity.

In earlier reports, the thermoelectric transport properties of the constituent phases, i.e. Cu_2Te and Sb_2Te_3, has been tuned by controlling the charge carrier concentration via doping/alloying [47-49] and by microstructural engineering [50, 51]. Both chalcogenides crystallize in the

trigonal system and are intrinsically p-type semiconductors that form solid solution with each other over a wide range of compositions.

Cu_2Te has unique electronic properties [52] and belongs to the phonon-liquid-electron-crystal (PLEC) system possessing low thermal conductivity [53]. In recent times, di-copper chalcogenides such as Cu_2S, Cu_2Se, and Cu_2Te have become common due to the high thermoelectric figure-of-merit exhibited by these compounds [54]. Regardless of the simple chemical formula of copper chalcogenides, they have quite complex crystal structures, usually accompanied by several phase transitions [55]. From all these copper chalcogenide families, the phase sequence of Cu_2Te is the most complicated, which undergo five successive phase transitions from room temperature to 900 K. Cu_2Te, corresponding to α, β, γ, δ, and ε, took place at 454 K, 597 K, 627 K, and 759 K, respectively [54, 55]. Electronic band structure calculations show that Cu_2Te is a semimetal with metallic conductivity, while optical studies find this alloy to be a semiconductor with a bandgap of 1.04 eV [54]. The phase transition could indeed cause extra phonon and carrier scattering, then Cu_2Te should be a striking critical scattering candidate for TE materials. Additionally, tellurium is not only heavier but is also less electronegative than sulphur and selenium, making telluride's reasonably more promising TE materials than sulphides and selenides [56]. The sample CT2 has a higher S (29.5 μV K−1 at 573 K) and a lower σ (2513 S cm at 573 K) due to a lower carrier (hole) concentration.

In Sb – Te system, Sb_2Te_3 is the most stable compound. Sb_2Te_3 is a p-type thermoelectric material applicable near room temperature application and plays a vital role in thermoelectric technology [57-61]. This material has rhombohedra (R-3m) structure with a lattice parameter of a = b = 4.264 Å and c = 30.458 Å consisting of a layer of five atomic planes with a sequence of Te1-Sb-Te2-Sb-Te (R), where Te1 and Te2 denote the position of Te atoms [60], Each of the five atomic planes is a weak Van-der-Waals interaction that exists between the adjacent layers [57]. The thermoelectric properties of Sb_2Te_3 and its alloys has been studied extensively

both theoretically and experimentally. The room temperature Seebeck coefficient value of Sb_2Te_3 compound is 83 μV/K along the cleavage plane and 92 μV/K perpendicular direction [62].

Thermoelectric properties of a pseudo-binary phase Sb_2Te_3 and Cu_2Te prepared by solid-state synthesis for hypereutectic, eutectic, and hypoeutectic composition SN05, SN15, SN25, SN33, and SN42 it has been reported a power factor PF of 0.4 - 0.6 (unit). The alloys have a higher Seebeck coefficient at a higher temperature (S∼110 μV/K at 600 K), and σ lies in the range of 4000 and 11,000 S cm^{-1} at 350 K from SN05 to SN62 [30]. However, few quantitative studies in the literature are available that aims at correlating quantitatively the scale and arrangements of multicomponent phases with thermoelectric power factor. The goal of this study is to achieve this on a set of pseudo-binary Cu_2Te-Sb_2Te_3 eutectic alloys through directional solidification using a modified-Bridgman type apparatus.

3.2. Experimental Procedure:

The pseudo-binary eutectic alloy composition $(Cu_2Te)_{62.02}$-$(Sb_2Te_3)_{37.98}$ was chosen for the present study according to the phase diagram given in Fig.3.1 [43]. The elemental shots of Cu (4N), Sb (4N) and Te (4N) were weighed according to the stoichiometric ratio Cu (33 at.%), Sb (20.21 at.%) and Te (46.79 at.%) and sealed in evacuated quartz tubes. The elements were melted together to obtain homogeneous compositions using induction melting. Synthesized alloys were sealed in evacuated quartz tubes and were used for directional solidification experiments. A modified-Bridgman apparatus was used for directionally solidifying the alloys. The modified-Bridgman type apparatus consists of the isothermal hot zone, isothermal chill zone separated by an insulating zone as shown in

Fig. 3.2 (a). The required temperature of the hot zone is obtained through resistance heating (Kanthal-A is used as a heating element). Chill zone is maintained at lower temperatures by

continuous circulation of chilled water. The purpose of the insulation zone is to establish a thermal gradient between the hot and chill zones without much heat transfer between the zones. The axial temperature profile in the apparatus is obtained when the hot zone is set at 923 K and the chill zone has 398 K water circulation, using a thermocouple which is kept stationary and measured the temperatures when the apparatus is moved relatively to the thermocouple. The axial temperature plot is as shown in

Fig. 3.2 (b). The temperature gradient at the melting point of the eutectic is calculated using the axial temperature plot and is 23.4 K/mm. We have varied solidification rates by changing the rate of traverse of the apparatus relative to the stationary sample using a gearbox coupled with a stepper motor that translates the assembly along a fixed linear drive. Using this assembly, we directionally solidified the alloys up to 80 mm length at a constant temperature gradient (23.4 K/mm) and different pull velocities (V= 1, 4, 16, 32 µm/s).

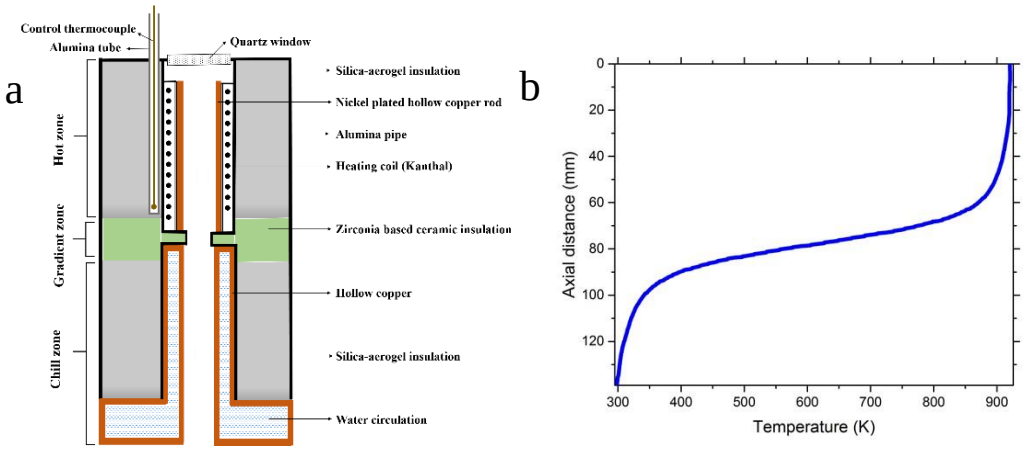

Fig. 3.2: Schematic of the modified Bridgman apparatus is shown in (a), whereas (b) is axial temperature profile obtained using thermocouple from hot zone to chill zone

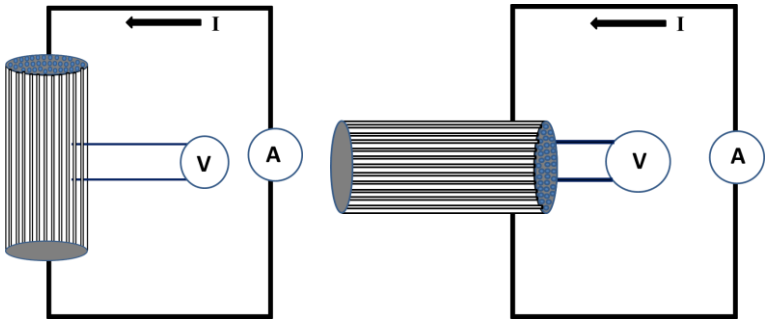

(a) *(b)*

Fig. 3.3: Schematic showing the measurement of the Seebeck coefficient and electrical resistivity along (a) longitudinal direction (parallel to the solidification direction) and (b) transverse direction (perpendicular to the solidification direction)

3.2.2. Characterization techniques:

Traditional polishing techniques are employed for metallographic analysis of transverse and longitudinal sections of the directionally solidified samples. Microstructure characterization has been done using a field-emission microscope equipped with an electron probe microanalyzer JEOL, JXA-8530F. Cylindrical samples of c.a 12 mm x 6 mm were used for the measurement of the transport properties, along both parallel and perpendicular to the solidification direction as shown in Fig. 3.3 (a) and (b) respectively. The transport properties such as Seebeck coefficient and electrical resistivity of the alloys were measured in the temperature range between 300 K and 600 K, using the ULVAC ZEM-3 system. A differential method was used for the measurement of Seebeck coefficient while a four-probe method was used for electrical resistivity. The errors in measurement for the Seebeck coefficient and electrical resistivity were 7% and 10% respectively.

3.3. Results and Discussions

3.3.1. Microstructure and phase analysis:

The microstructures of the eutectic system obtained by directional solidification at different solid-liquid interfacial velocities are shown in Fig. 3.4. The microstructure of the low magnification transverse section using SEM is shown in a1, b1, c1, d1 whereas that of high magnification transverse sections shown in a2, b2, c2, d2 of Fig. 3.4. Micrographs of the

longitudinal section are shown in a3, b3, c3, d3 of Fig. 3.4. The microstructures reveal the formation of two-phase colonies in the samples solidified at V=32, 16, 4 μm/s. Since the alloys we have chosen fall in the pseudo-binary eutectic valley in the ternary phase diagram [43], such compositions can undergo univariate eutectic reaction during solidification and can lead to diffusive instabilities that arise beyond a critical velocity leading to the formation of two-phase colonies. This phenomenon is very similar to the Mullins-Sekerka instability [63] that occurs in single-phase solidification. Such types of two-phase instabilities (colonies) reported in [64, 65]. At velocities greater than 1 μm/s, the eutectic front gets de-stabilized, causing the formation of these colonies.

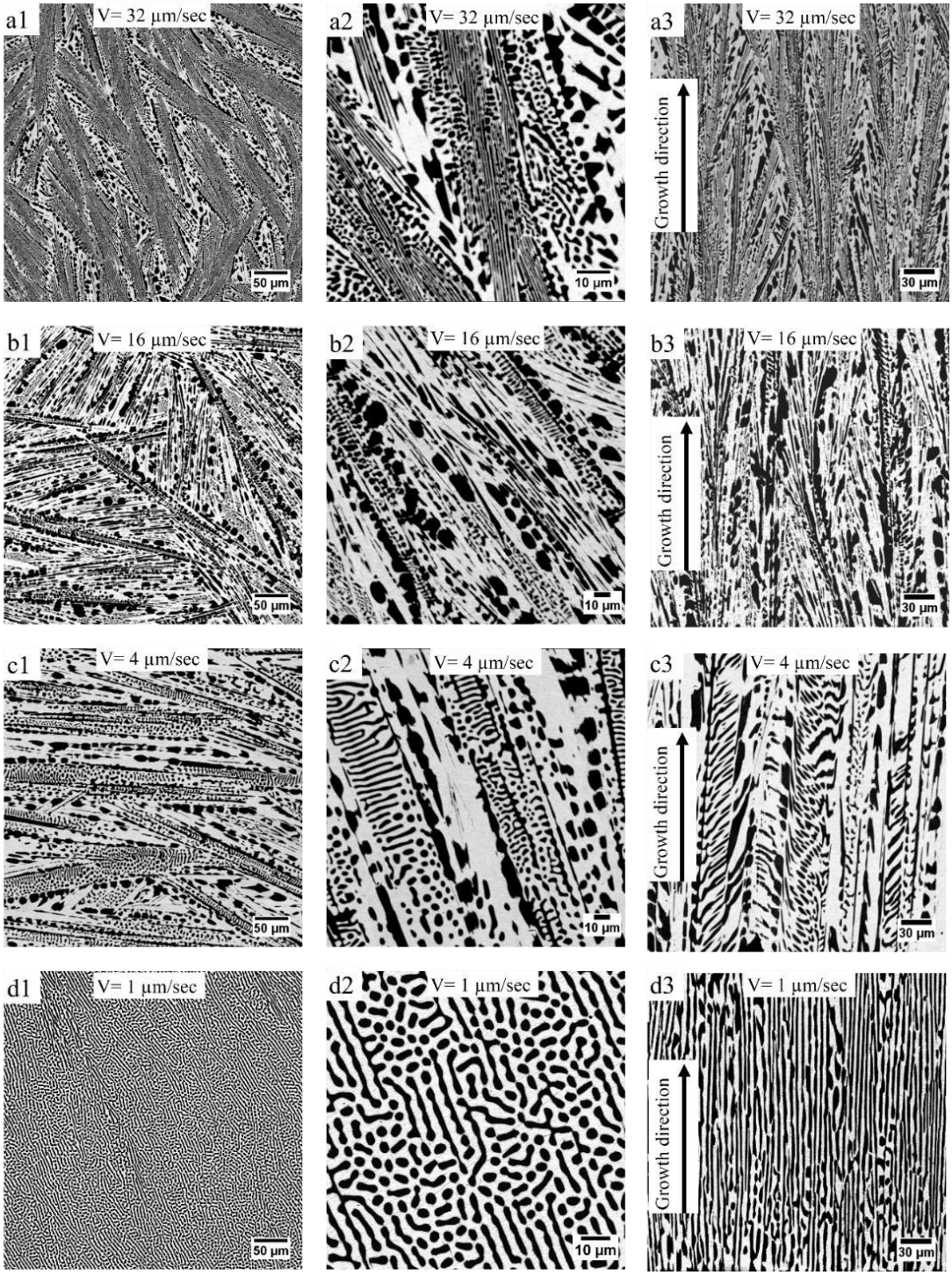

Fig. 3.4: SEM images captured from directionally solidified samples at different velocities (a to d represent the variation in morphology with a decrease in velocity). a1,a2,b1,b2,c1,c2,d1,d2 are images captured from transverse sections and a3,b3,c3,d3 are the images captured from the longitudinal sections

3.3.2. Morphology and eutectic length scale selection:

The morphology of eutectic is lamellar inside the colony at higher velocities i.e. V = 32, 16 µm/s. However, with a decrease in velocity to V = 4, 1 µm/s, we observe predominantly

degenerate lamella morphology of the eutectic. Morphology of the colonies observed in all cases is plate type. We have determined the eutectic spacing as well as the colony spacing using ImageJ software. In Table 1 and Fig. 3.5 (a), the variation of the eutectic lamellar and colony spacing with solidification rates have been provided. The variation of average eutectic spacing (λ) with the inverse square root of velocity ($V^{-0.5}$) is plotted in the Fig. 3.5 (b). The eutectic spacing shows an increasing trend with a decrease in velocity. The square of the slope of the linear fit gives the scaling constant $\lambda^2 V$ as c.a. 2.37±0.16 $\mu m^3/s$. A slight deviation from the linear fit could be due to the formation of colonies in the eutectic system.

Table 3.1: The lamellar and colony spacing of the alloys at different solidification rates

Nomenclature	*Solidification rate (µm/s)*	*Lamellar spacing (µm)*	*Colony Spacing (µm)*
Alloy 1	***1***	***2.41±0.22***	∞
Alloy 2	***4***	***1.86±0.13***	***95.7±17.2***
Alloy 3	***16***	***1.46±0.35***	***49.7±8.8***
Alloy 4	***32***	***0.95±0.27***	***42.7±10.2***

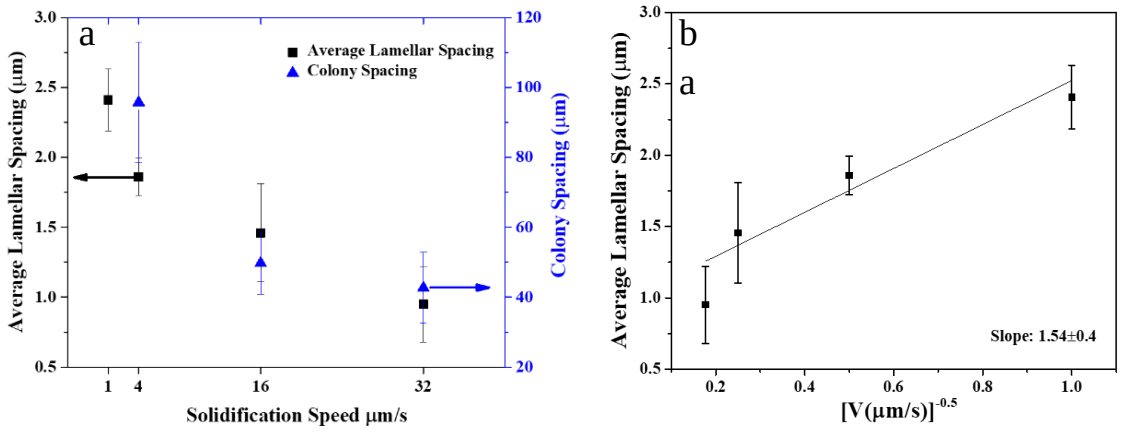

Fig. 3.5: (a) Variation of lamellar spacing and colony spacing with different solidification velocities; (b) variation of eutectic lamellar spacing of the alloys with the inverse square root of different solidification velocities

3.3.3. Composition distribution:

Composition distribution maps are obtained with an electron probe microanalyzer (JEOL, JXA-8530F) equipped with a field emission source. The map of the sample solidified at 32 µm/s along the transverse direction is shown in Figure 3.6. It reveals that composition is not homogenous throughout the microstructure. The higher compositions of Sb in inter-colony regions as shown in Figure 3.6 is due to segregation of Sb in the cell boundary during solidification. Similar variations in Sb composition is also observed in samples solidified at a growth rate of 16 and 4 µm/s. The Composition distribution map of the sample solidified at 1 µm/s along the transverse section is shown in Fig. 3.7. As we already pointed out that the samples solidified at 1 µm/s had no colony formation due to suppression of colonies, we observe the uniform distribution of elements in their respective phases.

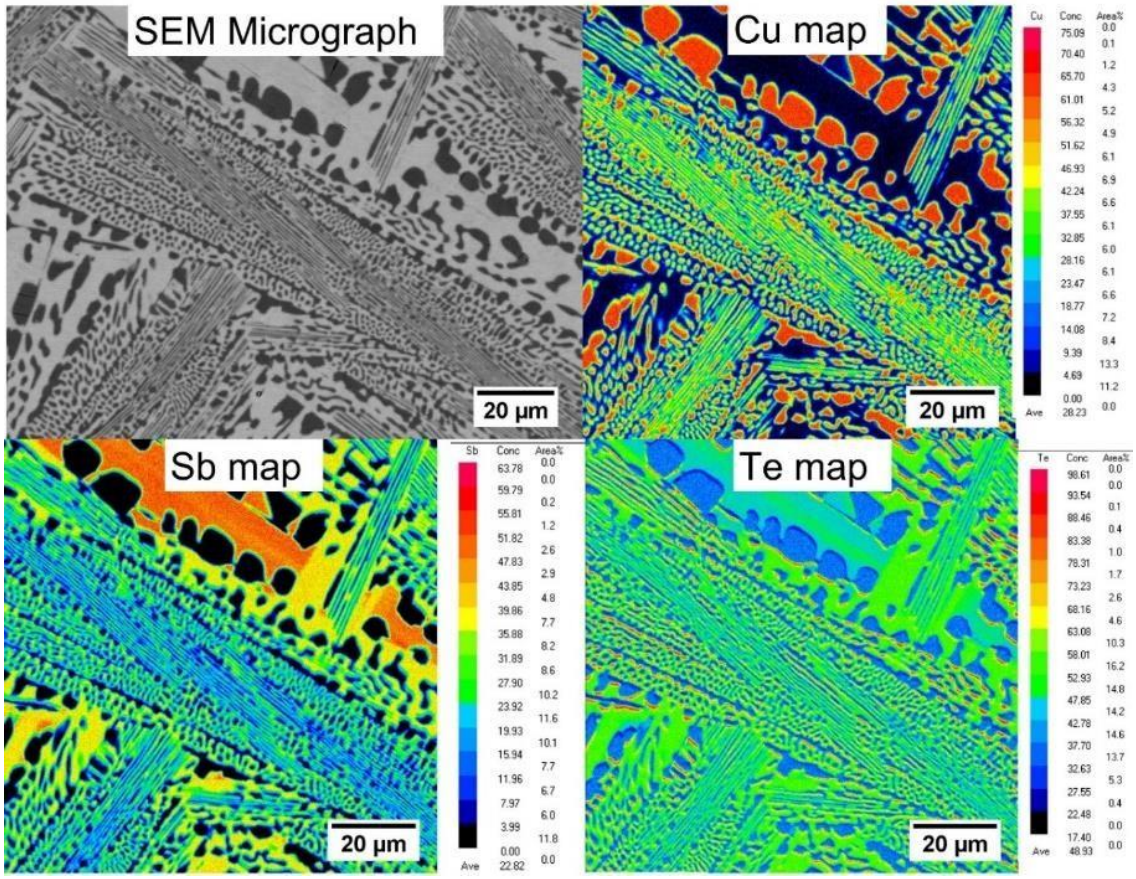

Figure 3.6: Composition distribution maps (along the transverse section) obtained from the sample solidified at 32 µm/s for Cu, Sb, Te elements showing segregation of element Sb in inter colony regions

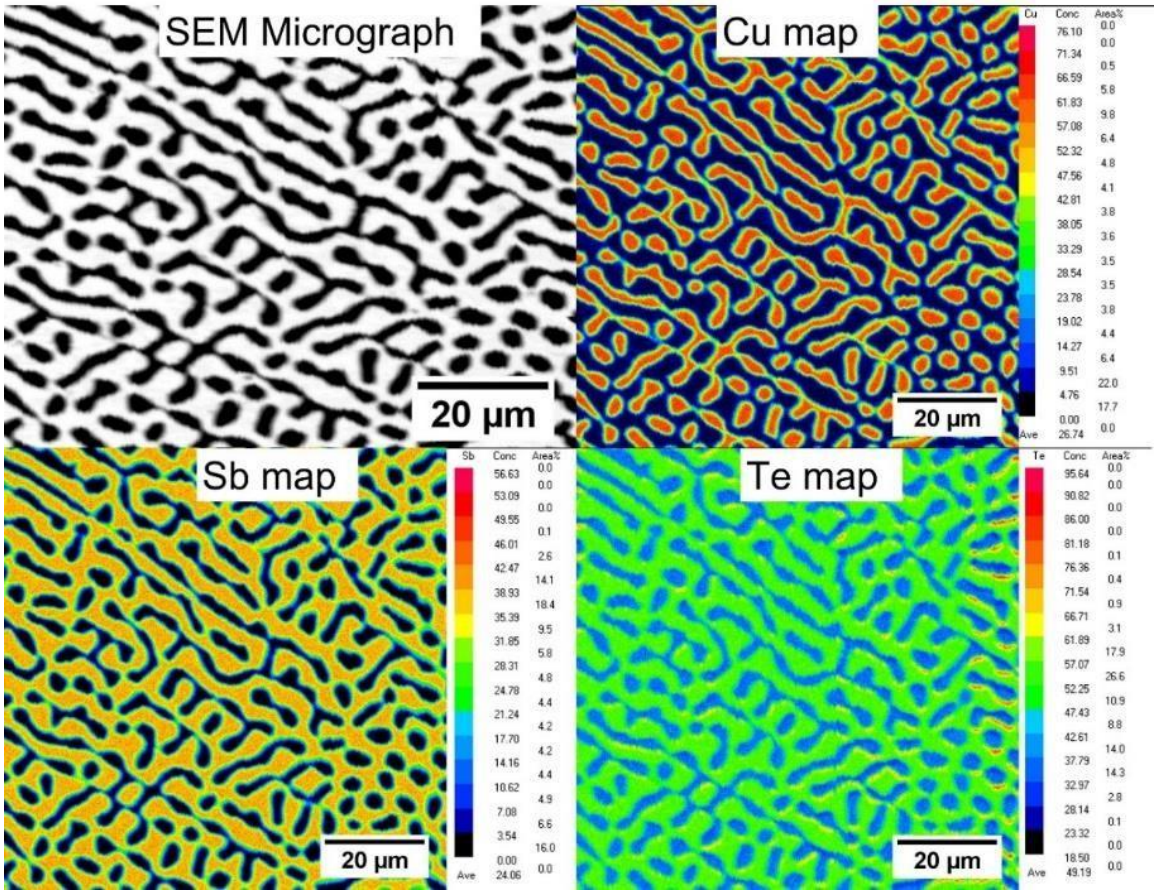

Fig. 3.7: Composition distribution maps (along the transverse section) obtained from the sample solidified at 1 µm/s for Cu, Sb, Te elements showing the uniform distribution of elements in each phase.

3.4. Thermoelectric transport properties:

The different rates of solidification results in the variation of the spacing of the eutectic as well as the morphology of the phases. As has been shown in Table 3.1 and Fig. 3.5 (a), the average lamellar spacing, as well as the colony spacing, decreases with an increase in the solidification rate. The decrease in the spacings will result in enhanced carrier (holes) scattering and thereby affect the transport properties. Moreover, the difference in the alignment of the phases results in anisotropy in electronic properties in different directions. We, therefore, measured the transport properties of the alloys in two directions: (1) parallel to the solidification direction (termed as longitudinal, and (2) perpendicular to the solidification direction (termed as transverse) and correlated the properties in each of the directions with the variation in lamellar spacing.

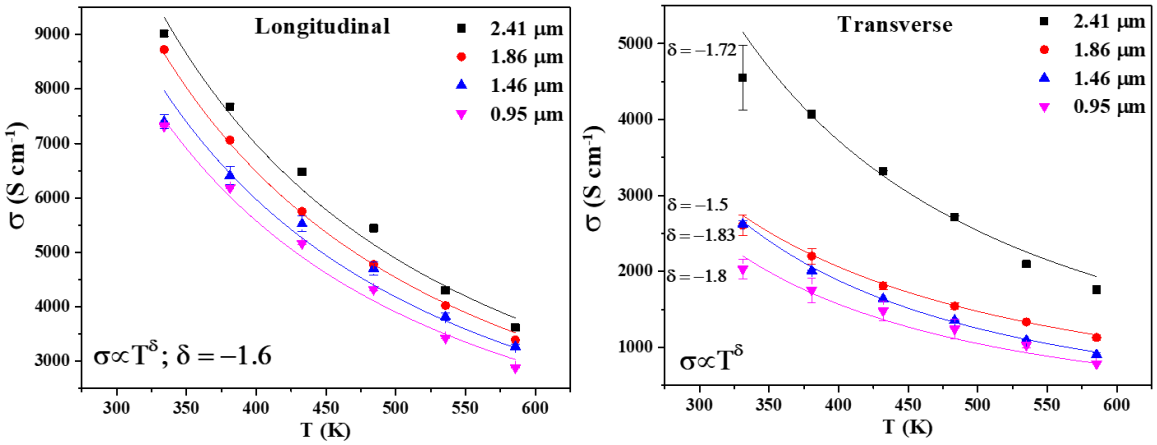

Fig. 3.8: Temperature-dependent variation of the electrical conductivity with changes in lamellar spacing; measurement carried out along longitudinal and transverse directions As shown in Fig. 3.8, the electrical conductivity of the alloys decreases with temperature following the power-law $\sigma \propto T^{\delta}$ where δ is the relaxation time [65]. From the theoretical fit of the power-law, the δ values for all the alloys in the longitudinal direction could be estimated to be -1.6. The same δ values indicate that the scattering phenomena in all the alloys are the same in a longitudinal direction. Whereas, the values were different for each alloy in the transverse direction. This indicates that carriers get scattered differently in each alloy due to differences in the Cu_2Te-Sb_2Te_3 interfaces. In both the longitudinal and transverse directions, the values of δ indicate that the carrier scattering is dominated by acoustic phonon scattering [66, 67].

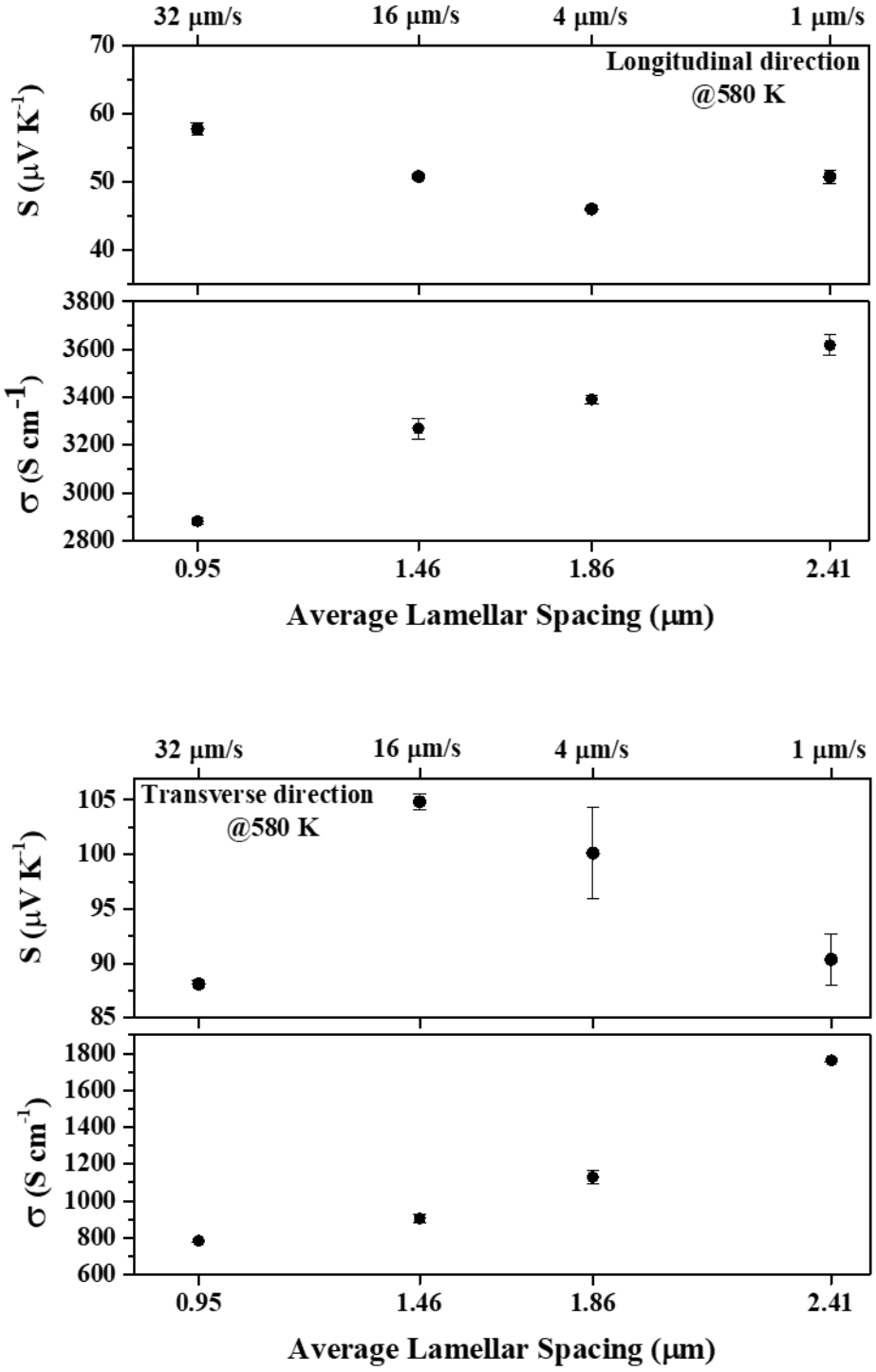

Fig. 3.9: Variation of Seebeck coefficient and electrical conductivity with lamellar spacing along a longitudinal and transverse direction at 580 K

In both the configurations, the electrical conductivity is higher in the sample with 1μm/s solidification rate and decreases systematically with an increase in the rate. This correlates with the systematic decrease in the lamellar spacing as shown in Fig. 3.9. As the solidification rate

increases, the lamellar spacing decreases from 2.41 µm to 0.95 µm. This means that the number of interfaces increases, leading to an enhancement in charge carriers scattering in the alloy with 0.95 µm spacing. There is a systematic trend between electrical conductivity and lamellar spacing in both longitudinal and transverse cases. However, the conductivity has reduced significantly (almost by half) in the transverse direction compared to the longitudinal direction. This is because, when the electrical conductivity is measured in the longitudinal direction, the equivalent electrical circuit will be similar to that of resistors (here the $Cu_2TeSb_2Te_3$ eutectics) connected parallel to each other. Compared to a series connection with the same set of resistors, the overall resistivity will be low (i.e. conductivity will be high) in parallel configuration (longitudinal direction).

In Fig. 3.10, the Seebeck coefficient of the alloys measured along longitudinal as well as in transverse direction has been shown. The alloys exhibit p-type semiconducting nature as can be observed from positive values of Seebeck coefficients. The following defect equilibrium relations (3.3 and 3.4) shows the origin of the p-type conductivity. The Cu vacancies (V'_{Cu}) and the antisite defects (Sb'_{Te}) leads to the creation of holes ($h^{\cdot}$) in the pseudo-binary alloys.

(3.3) $$Sb_2Te_3 \rightarrow 2Sb'_{Te} + 2h^{\cdot} + \frac{5}{2}\,Te_2\,(g)$$

(3.4) $$Cu_{2-x}Te \rightarrow 2Cu^{\times}_{Cu} + Te^{\times}_{Te} + xV'_{Cu} + xh^{\cdot}$$

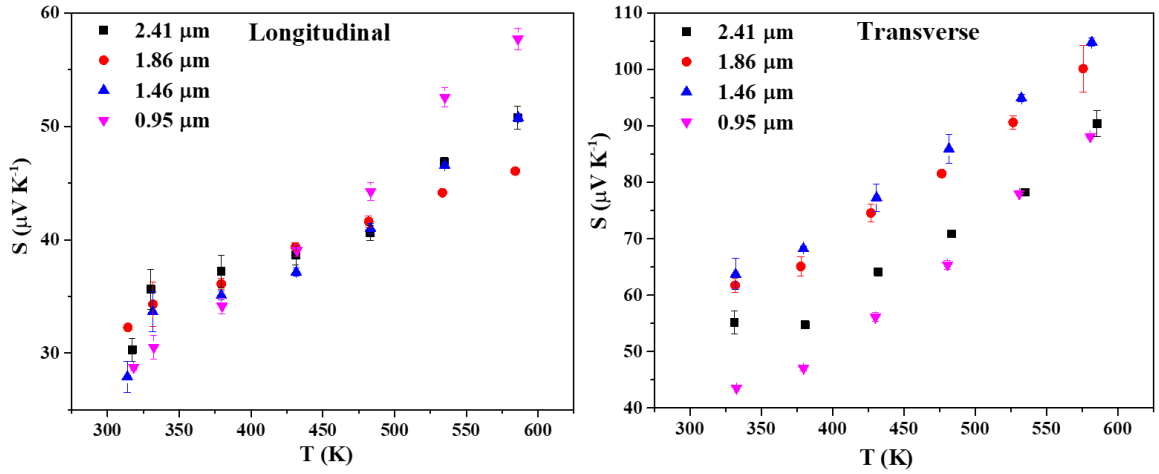

Fig. 3.10: The temperature-dependent Seebeck coefficient measured along the longitudinal and transverse direction

According to the relation,

$$S = \frac{8\pi^2 k_B^2}{3eh^2} m^*_{DOS} T \left(\frac{\pi}{3n}\right)^{2/3} \quad (3.7)$$

(Where S is the Seebeck coefficient, m^*_{DOS} is the density-of-states effective mass of the carriers, n is the carrier concentration and T is the absolute temperature); it can be seen that the Seebeck coefficient is inversely related to the charge carrier concentration. Since the electrical conductivity is lower in the transverse direction, the available charge carriers might also be lower. Hence, compared to the Seebeck coefficient in the longitudinal direction of measurement, those at the transverse direction of measurement are higher.

As can be seen in Fig. 3.9, the effect of lamellar spacing on the electrical conductivity is systematic throughout all the alloys. This contrasts with our observation for Seebeck coefficient. As the lamellar spacing increases, the available charge carriers are more since it does not undergo scattering. If the effective mass (m^*_{DOS}) of the carriers remains constant and only the carrier concentration differs (as governed by relation 3.7), then the value of Seebeck coefficient will decrease with increase in lamellar spacing. In the longitudinal direction, the Seebeck values decrease systematically until 1.86 µm. Thereafter, a slight increase in *S* can be observed as the lamellar spacing increased to 2.41 µm. In the transverse direction, the Seebeck

value was ~ 88 μV K^{-1} at 0.95 μm and showed a peak at 1.46 μm. Thereafter it decreased systematically from 104 μV K^{-1} to 90 μV K^{-1} with an increase in the lamellar spacing from 1.46 μm to 2.41 μm.

The power factor ($PF=S^2\sigma$) for all the alloys, in both longitudinal and transverse directions, as shown in Fig. 3.11. The power factor does not vary much with temperature in both the directions of measurement. This holds significant importance from the perspective of the application. The PF increased with an increase in lamellar spacing in both the directions of measurement. It can be observed from the microstructural studies that, the formation of colonies in the eutectic system could be suppressed by reducing the solidification velocity. Suppression of colonies eliminated the compositional inhomogeneity that arises due to segregation of components in the inter-colony regions. Such uniform microstructure obtained below critical velocity (i.e. 1 μm/s) showed uniform distribution of components. This led to an improvement in the thermoelectric power factor which was even higher than that obtained in ref. [51] for the same eutectic composition. The highest power factor was obtained for the alloy with 2.41 μm along the transverse direction.

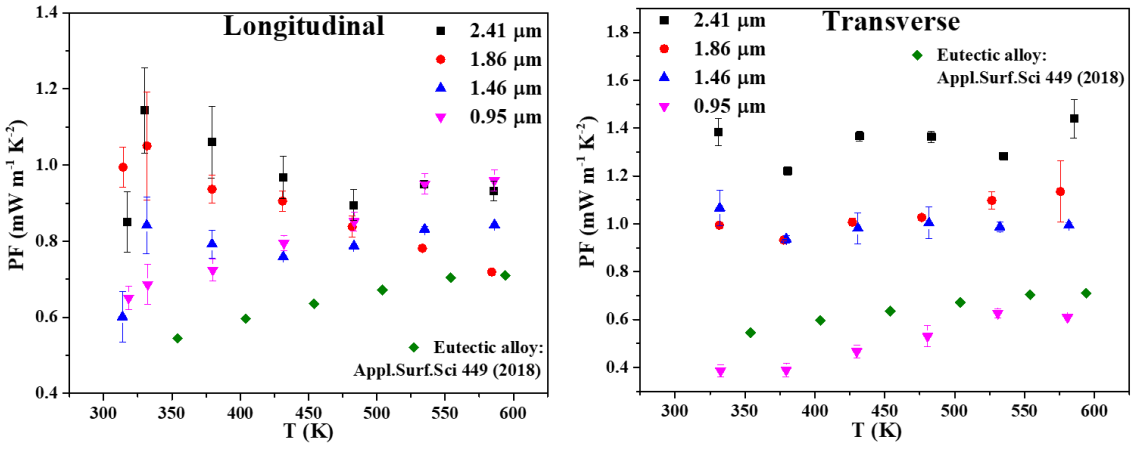

Fig. 3.11: The power factor ($S^2\sigma$) along a longitudinal direction and transverse direction; power factor of the eutectic alloy with composition Cu 33 at.% from ref [51] has been plotted for comparison

Table 3.2: Comparison of the transport properties of the alloys in the transverse direction with that of pristine Sb_2Te_3 [71], Cu_2Te [48] and the same eutectic alloy $(Cu_2Te)_{62.02}$-$(Sb_2Te_3)_{37.98}$ taken from [51]at 350 K

Sample	*Seebeck Coefficient ($\mu V\ K^{-1}$)*	*Electrical conductivity ($S\ cm^{-1}$)*	*Power factor ($mW\ m^{-1}\ K^{-2}$)*
Sb_2Te_3[49]	*100*	*5000*	*5*
Alloy 1 (2.41 µm)	*54.77±0.52*	*4550.05±427.83*	*1.22±0.01*
Alloy 2 (1.86 µm)	*65.10±1.68*	*2607.81±130.81*	*0.93±0.01*
Alloy 3 (1.46 µm)	*68.26±0.34*	*2623.08±44.46*	*0.94±0.02*
Alloy 4 (0.95 µm)	*47.05±0.49*	*2031.10±126.54*	*0.39±0.02*
Eutectic Alloy [34]	*28.90*	*6526*	*0.55*
Cu_2Te[32]	*10*	*10000*	*0.1*

3.5. Conclusion:

In this work, the microstructure and thermoelectric transport properties of the self-organized eutectic composites obtained by directional solidification of pseudo-binary $(Cu_2Te)_{62.02}(Sb_2Te_3)_{37.98}$ alloys have been explored. At higher growth rates (32, 16 and 4 µm/s), cellular microstructures and segregation at cell boundaries could be observed due to growing instability. However, the sample solidified at a slower growth rate (1 µm/s) had uniform microstructures free of cellular segregation. Due to variation in the configuration of the phases along the longitudinal and transverse direction, anisotropy was observed in the thermoelectric transport properties. A higher electrical conductivity accompanied by a lower Seebeck coefficient was obtained in the alloys along longitudinal direction compared to that in the transverse direction. Further, a systematic trend between conductivity and lamellar spacing in both longitudinal and transverse cases was observed. With an increase in the solidification rate, the lamellar spacing decreased from 2.41 µm to 0.95 µm. This resulted in increased carrier scattering and hence the electrical conductivity was least in the sample with
0.95 µm in both directions. However, this adversely affected the thermoelectric power factor (PF) and a maximum value of PF of ~ 1.4 mW m^{-1} K^{-2} along the transverse direction could be obtained at 580 K in the sample free of cellular segregation with an interlamellar spacing of
2.41 µm.

3.6. Reference

1. M. G. Kanatzidis, C.M., 2010, 22, 648.

2. Z. H. Ge, B.P.Z., P. P. Shang and J. F. Li, J. Mater. Chem., and 2011, 9194.

3. J. R. Szczech, J.M.H.a.S.J., J. Mater. Chem., 2011, 21, and 4037.

4. Y.X. Zhao, J.S.D.a.C.B., J. Mater. Chem., 2011, 21, 17049.

5. X. Shi, J.Y., S. Q. Bai, J. H. Yang, H. Wang, M. F. Chi,, W.Q.Z. J. R. Salvador, L. D. Chen and W. Wong-Ng, Adv., and Funct. Mater., 20, 755.

6. K. Kishimoto and T. Koyanagi, J.A.P., 2002, 92, 2544.

7. M. R. Dirmyer, J.M., G. S. Nolas, A. Sen and J. V. Badding, and Small, 5, 933.

8. M. Takashiri, K.M., S. Tanaka, J. Kurosaki, D. Nagai and and J.A.P. H. Tsukamoto, 2008, 104, 084302.

9. D. Liu, C.D., M. Sayring, S. Teichert, M. Rettenmayr, Reduced thermal conductivity of Bi-In-Te thermoelectric alloys in a eutectic lamellar structure, (2018) 730–736.

10. M.-J. Suk, G.-H.C., I.-H. Moon, Determination of microstructural anisotropy in SbInSb eutectic by electrical resistivity measurement, J. Mater. Sci. 31 (1996) 1663– 1668. doi:10.1007/BF00357879.

11. Q. Zhang, E.K.C., Y. Wang, H.S. Kim, R. He, F. Cao, K. Dahal, D. Broido, G. Chen, Z. Ren, High thermoelectric performance of n-type PbTe1-ySy due to deep lying states induced by indium doping and spinodal decomposition, Nano Energy. 22 (2016) 572–582. doi:10.1016/j.nanoen.2016.02.040.

12. S. Gorsse, P.B.P., R. Decourt, E. Sellier, Microstructure engineering design for thermoelectric materials: An approach to minimize thermal diffusivity, Chem. Mater. 22 (2010) 988–993. doi:10.1021/cm901862m.

13. Y. Gelbstein, B.D., O. Ben-Yehuda, Y. Sadia, Z. Dashevsky, M.P. Dariel, High thermoelectric figure of merit and nanostructuring in bulk p-type Gex(SnyPb1-y)1xTe alloys following a spinodal decomposition reaction, Chem. Mater. 22 (2010) 1054–1058. doi:10.1021/cm902009t.

14. A. Phys, I.e.c.i.f.-g.Z., Hf) NiSn based thermoelectric materials with nanoscale precipitates, 254104 (2015).

15. C. Yu, H.X., C. Fu, T. Zhu, X. Zhao, High performance half-Heusler thermoelectric materials with refined grains and nanoscale precipitates, J. Mater. Res. 27 (2012) 2457–2465. doi:10.1557/jmr.2012.171.

16. D. Liu, X.L., P.M. De Castro Borlido, S. Botti, R. Schmechel, M. Rettenmayr, Anisotropic layered Bi2 Te3 -In2 Te3 composites: Control of interface density for tuning of thermoelectric properties, Sci. Rep. 7 (2017) 1–13. doi:10.1038/srep43611.

17. J.D. Sugar, D.L.M., Precipitation of Ag2Te in the thermoelectric material AgSbTe2, J. Alloys Compd. 478 (2009) 75–82. doi:10.1016/j.jallcom.2008.11.054.

18. B. Chalmers, P.o.s., (1964).

19. J.A. Dantzig, M.R., Solidification, EPFL press, 2009.

20. J.R. Sootsman, J.H., V.P. Dravid, C.P. Li, C. Uher, M.G. Kanatzidis, High thermoelectric figure of merit and improved mechanical properties in melt quenched PbTe-Ge and PbTe- Ge1-x Six eutectic and hypereutectic composites, J. Appl. Phys. 105 (2009). doi:10.1063/1.3093833.

21. T. Ikeda, L.A.C., V.A. Ravi, F.S. Gascoin, S.M. Haile, G.J. Snyder, Chem. and M. 763e767.

22. T. Ikeda, V.A.R., G. Jeffrey Snyder, Microstructure size control through cooling rate in thermoelectric PbTe-Sb2Te3 composites, Metall. Mater. Trans. A Phys. Metall. Mater. Sci. 41 (2010) 641–650. doi:10.1007/s11661-009-0143-4.

23. J.B. Vaney, S.A.Y., H. Takaki, K. Kobayashi, N. Kobayashi, T. Mori, Magnetismmediated thermoelectric performance of the Cr-doped bismuth telluride tetradymite, Mater. Today Phys. 9 (2019) 100090. doi:10.1016/j.mtphys.2019.03.004.

24. T. Mori, N.P.a.N.M.f.E.T., Small. 13 (2017) 1–10. doi:10.1002/smll.201702013.

25. W. Liu, H.S.K., Q. Jie, Z. Ren, Importance of high power factor in thermoelectric materials for power generation application: A perspective, Scr. Mater. 111 (2016) 3– 9. doi:10.1016/j.scriptamat.2015.07.045.

26. Lee, M.H., et al., *High thermoelectric figure-of-merit in Sb2Te3/Ag2Te bulk composites as Pb-free p-type thermoelectric materials.* J. Mater. Chem. C. **3**.

27. Ikeda, T., et al., *Self-Assembled Nanometer Lamellae of Thermoelectric PbTe and Sb2Te3 with Epitaxy-like Interfaces.* Chemistry of Materials, 2007. **19**(4): p. 763-767.

28. Venkatasubramanian, R., et al., *MOCVD of Bi2Te3, Sb2Te3 and their superlattice structures for thin-film thermoelectric applications.* Journal of Crystal Growth, 1997. **170**(1): p. 817-821.

29. Cao, Y.Q., et al., *Syntheses and Thermoelectric Properties of Bi2Te3/Sb2Te3 Bulk Nanocomposites with Laminated Nanostructure.* Applied Physics Letters, 2008. **92**: p. 143106-143106.

30. Mukherjee, S., et al., *Microstructure and thermoelectric properties of Cu2Te-Sb2Te3 pseudo-binary system.* Applied Surface Science. **449**: p. 805-814.

31. J. Liu, X.W., L. Peng, Intermetallics 41 (2013) 63e69.

32. J.H. Yim, K.J., H.J. Kim, H.H. Park, C. Park, J.S. Kim, J. Electron. Mater. 40 and 1010e1014.

33. J.R. Sootsman, J.H., V.P. Dravid, S. Ballikaya, D. Vermeulen, C. Uher, and C.M.e. M.G. Kanatzidis.

34. H. Wu, W.F., S. Chen, G.J. Snyder, App. Phys. Lett. 101 (2012), 023107.

35. J. Dadda, E.M., S. Perlt, T. H€oche, R. Hermann, A. Neubrand, Phys. Status and S.A. 1276e1281.

36. Y. Zhang, L.W., J. Zhang, J. Xing, J. Luo, Acta Mater. 111 (2016) 202e209.

37. Y. Cheng, J.Y., Q. Jiang, D. He, J. He, Y. Luo, D. Zhang, Z. Zhou, Y. Ren, J. Xin, and J.M.C.A. 5163e5170.

38. A.A. Kulkarni, E.H., R. Zhang, K. Thornton, P. V. Braun, Archimedean lattices emerge in template-directed eutectic solidification, Nature. 577 (2020) 355–358. doi:10.1038/s41586-019-1893-9.

39. D.A. Pawlak, S.T., M. Gajc, K. Kolodziejak, R. Diduszko, K. Rozniatowski, J. Smalc, I. Vendik, How far are we from making metamaterials by self-organization? the microstructure of highly anisotropic particles with an SRR-like geometry, Adv. Funct. Mater. 20 (2010) 1116–1124. doi:10.1002/adfm.200901875.

40. I. Kh. Mamedov, D.H.A., A.A. Khalilova, R.N. Rahimov, Inorg. Mater. 52 and 423e428.

41. R. Elliot, E.S.P.C.a.G.A., Butterworths &Co Ltd. (1983).

42. S. Akamatsu, M.P., Eutectic and peritectic solidification patterns, Curr. Opin. Solid State Mater. Sci. 20 (2016) 46–54. doi:10.1016/j.cossms.2015.10.002.

43. R.A. Kuliev, A.N.K., V.M. Glazov, Phase Equilibria and Intermolecular Interactions in Systems Formed by Copper and Antimony Chalcogenides, Russ. J. Phys. Chem. (1969).

44. Guin, S.N., A. Banik, and K. Biswas, *Thermoelectric Energy Conversion in Layered Metal Chalcogenides,* in *2D Inorganic Materials beyond Graphene*, WORLD SCIENTIFIC (EUROPE). p. 239-274.

45. Han, C., et al., *Thermoelectric Enhancement of Different Kinds of Metal Chalcogenides.* Advanced Energy Materials. **6**(15): p. 1600498.

46. Tzounis, L., et al., *Chapter 9 - Synthesis and Processing of Thermoelectric Nanomaterials, Nanocomposites, and Devices*, in *Nanomaterials Synthesis*, Elsevier. p. 295-336.

47. K. Zhao, K.L., Z. Yue, Y. Wang, Q. Song, J. Li, M. Guan, Q. Xu, P. Qiu, H. Zhu, L. Chen, X. Shi, Are Cu2Te-Based Compounds Excellent Thermoelectric Materials?, Adv. Mater. 1903480 (2019) 1–8. doi:10.1002/adma.201903480.

48. S. Ballikaya, H.C., J.R. Salvador, C. Uher, Thermoelectric properties of Ag-doped Cu2Se and Cu2Te, J. Mater. Chem. A. 1 (2013) 12478. doi:10.1039/c3ta12508d.

49. Y. He, T.Z., X. Shi, S.-H. Wei, L. Chen, High thermoelectric performance in copper telluride, NPG Asia Mater. 7 (2015) e210. doi:10.1038/am.2015.91.

50. R. Venkatasubramanian, E.S., T. Colpitts, B. O'Quinn, Thin-film thermoelectric devices with high room-temperature figures of merit, Nature. 413 (2001) 597–602.

51. S. Mukherjee, O.E.F., R. Chetty, K. Chattopadhyay, S. Suwas, R.C. Mallik, Microstructure and thermoelectric properties of Cu2Te-Sb2Te3pseudo-binary system, Appl. Surf. Sci. 449 (2018) 805–814. doi:10.1016/j.apsusc.2017.11.198.

52. Y. Zhang, B.S., J. Zhou, Z. Sun, First principles investigation of the structure and electronic properties of Cu2Te, Comput. Mater. Sci. 81 (2014) 163–169. doi:10.1016/j.commatsci.2013.08.009.

53. S. Mukherjee, R.C., P.V.P. Madduri, A.K. Nayak, K. Wojciechowski, T. Ghosh, K. Chattopadhyay, S. Suwas, R.C. Mallik, Investigation on the structure and thermoelectric properties of Cu x Te binary compounds, Dalt. Trans. 48 (2019) 1040–1050. doi:10.1039/C8DT04351E.

54. Mallick, M.M. and S. Vitta, *Realizing high figure-of-merit in Cu2Te using a combination of doping, hierarchical structure, and simple processing.* Journal of Applied Physics. **122**(2): p. 024903.

55. Qiu, Y., et al., *Facile rapid synthesis of a nanocrystalline Cu2Te multi-phase transition material and its thermoelectric performance.* RSC Advances. **7**(36): p. 22558-22566.

56. Snyder, G.J. and E.S. Toberer, *Complex thermoelectric materials.* Nat. Mater., 2008. **7**.

57. Das, D., et al., *Defect induced structural and thermoelectric properties of Sb2Te3 alloy.* Journal of Applied Physics. **118**(4): p. 045102.

58. Femi, O., R. Narayanan, and K. Chattopadhyay, *Microstructure evolution and thermoelectric properties of Te-poor and Te-rich (Bi,Sb)2Te3 prepared via solidification.* Journal of Materials Science. **51**.

59. Wang, X.-y., et al., *The Thermoelectric Performance of Sb2Te3-based Alloy is Improved by Introducing PN Junctions.* ACS Applied Materials & Interfaces. **10**.

60. Xu, B., et al., *Thermoelectric properties of monolayer Sb2Te3.* Journal of Applied Physics. **124**(16): p. 165104.

61. Yoo, I.-J., et al., *Thermoelectric characteristics of Sb2Te3 thin films formed via surfactant-assisted electrodeposition.* Journal of Materials Chemistry A. **1**: p. 54305435.

62. Lee, M.H., et al., *High thermoelectric figure-of-merit in Sb2Te3/Ag2Te bulk composites as Pb-free p-type thermoelectric materials.* Journal of Materials Chemistry C. **3**(40): p. 10494-10499.

63. W.W. Mullins, R.F.S., Stability of a planar interface during solidification of a dilute binary alloy, J. Appl. Phys. 35 (1964) 444–451. doi:10.1063/1.1713333.

64. S. Akamatsu, G.F., Traveling waves, two-phase fingers, and eutectic colonies in thinsample directional solidification of a ternary eutectic alloy, Phys. Rev. E - Stat.

Physics, Plasmas, Fluids, Relat. Interdiscip. Top. 61 (2000) 3757–3770. doi:10.1103/PhysRevE.61.3757.

65. Z. Ovadyahu, Y.I., Conductivity power-law temperature dependence of thin indium oxide films, J. Phys. C Solid State Phys. 18 (1985) 18–25. doi:10.1088/00223719/18/1/004.

66. J. Shuai, J.M., S. Song, Q. Zhu, J. Sun, Y. Wang, R. He, J. Zhou, G. Chen, D.J. Singh, Z. Ren, Tuning the carrier scattering mechanism to effectively improve the thermoelectric properties, Energy Environ. Sci. 10 (2017) 799–807. doi:10.1039/c7ee00098g.

67. S. Sarkar, X.Z., S. Hao, X. Hua, T.P. Bailey, C. Uher, C. Wolverton, V.P. Dravid, M.G. Kanatzidis, Dual Alloying Strategy to Achieve a High Thermoelectric Figure of Merit and Lattice Hardening in p-Type Nanostructured PbTe, ACS Energy Lett. 3 (2018) 2593–2601. doi:10.1021/acsenergylett.8b01684.

68. B. Zhang, J.S., H.E. Katz, F. Fang, R.L. Opila, Promising thermoelectric properties of commercial PEDOT:PSS materials and their Bi2Te3 powder composites, ACS Appl. Mater. Interfaces. 2 (2010) 3170–3178. doi:10.1021/am100654p.

69. M. Wang, N.P., Predictions of effective physical properties of complex multiphase materials, Mater. Sci. Eng. R Reports. 63 (2008) 1–30. doi:10.1016/j.mser.2008.07.001.

70. M.F. Ashby, Y.J.B., Designing hybrid materials, (2003) 5801–5821.

71. M.M. Ibrahim, M.M.W., E.K. Shokr, H.A.A. Ei-ghani, Electrical Properties of Antimony Telluride, 241 (1991) 237–241.

CHAPTER FOUR

4. Tuning the thermoelectric material transport properties: Case of brine quenched Cu_2Te- Sb_2Te_3 eutectic

4.1. Introduction

In most cases, the waste heat is lost without any either environmental or economic profit .this energy does not cost anything. It can be used to reduce the impact of energy crises and heating of the environment. Therefore, the interconversion of waste heat into electricity becomes a better solution. The converter of heat into electricity is called a thermoelectric generator (TEG). Thermoelectric generators (TEGs) have established their ability to directly convert thermal energy into an electrical one via the Seebeck effect. Also, they are no contribution to environmental pollution because they do not contain chemical products; they function noiselessly because they do not have mechanical structures and/or moving parts.

They can be fabricated on many types of substrates like polymers, ceramics, and silicon [1, 2]. The material which converts heat flow into electric current and vies verse is called power generation or refrigeration, respectively, known as thermoelectric materials [3]. The efficiency of both power generation and refrigeration is determined in general by a measure of the material`s dimension figure of merit, zT defined as:

$$zT = \frac{S^2 \sigma T}{K} \qquad (4.1)$$

Where S, σ, T, and K are Seebeck coefficient, electrical conductivity, absolute temperature at which figure of merit is measured, and thermal conductivity, respectively.

From this, it is clear that a high-performance TE material must possess a high Seebeck coefficient together with low thermal conductivity and electrical resistivity. The critical phenomenon to generate thermoelectric power is the Seebeck effect, where electricity generates due to temperature differences. The Seebeck coefficient is the electric potential difference

created by a temperature gradient (ΔT) [4]. It can also be defined as an intrinsic property of the materials related to their electronic properties and independent of their geometry [5]. Moreover, it is positive for p-type semiconductors and negative for the n-type ones. Fig. 1 shows the direction of charge flow during the Seebeck effect and on both cooling and power generation [6].

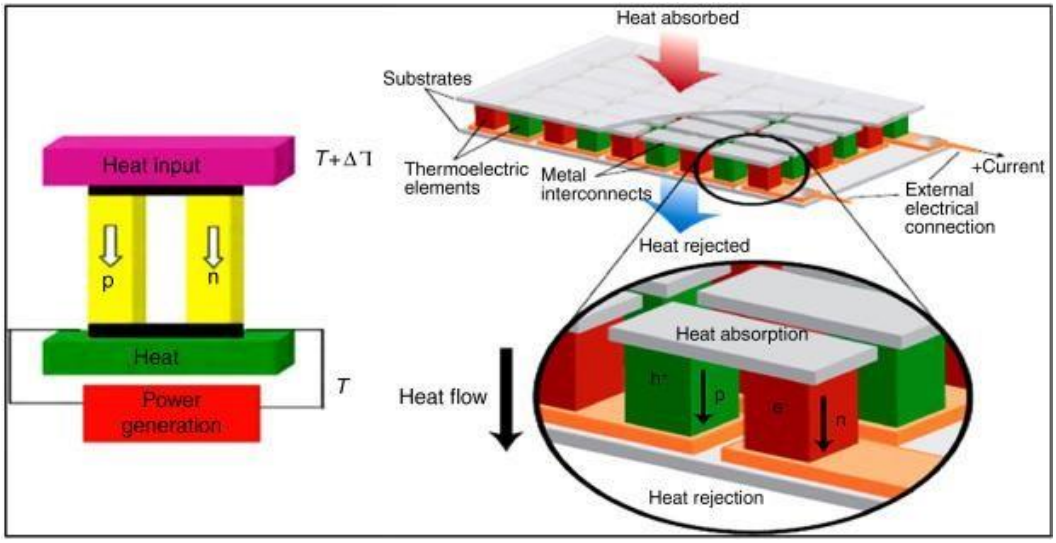

Fig. 4.1: Thermoelectric generator and cooling and direction of charge flow during Seebeck effect power generation) [6]

The power factor ($S^2\sigma$) is then a useful quantity for comparing the electrical properties of thermoelectric materials. Within much optimism about thermoelectrics in the 1950s and 1960s, numerous general criteria for better performance thermoelectric materials were established:

(a) They should be semiconductors with band gaps of ~4 kBT, where kB is the Boltzmann constant and T is the operating temperature;

(b) They should have low effective mass if acoustic phonon scattering controls conduction and high effective mass if ionized impurity scattering controls conduction;

(c); they should be comprised of heavy elements and

(d) They should be solid solutions with a disorder on the anion site and cation site for n-type and p-type materials, respectively [7].

There are two ways to increases zT one by boosting the power factor ($P=S^2\sigma$), two lowering thermal conductivity; thermal conductivity is the sum of electrical and thermal conductivity, especially the lattice thermal conductivity contribute to the total thermal conductivity properties comparing to the electronic thermal conductivities. At the present day, the most recent stage in the development of high thermoelectric performance composite is mainly due to their very low lattice thermal conductivity (R), resulting from phonon scattering. For example: In electron-phonon scattering effect on the lattice thermal conductivity of silicon nanostructures, the results show that the lattice thermal conductivity decreases as the feature size of nanostructures goes down and could be ignored at low feature sizes (50 nm for n-type nanowires and 20 nm for p-type nanowires and n-type solid thin films) even when the carrier concentration is as high as 10^{21} cm^{-3} [8].

A comparison of the data reported in the literature confirms that the Cu-Sb-Te pseudobinary system contains two binary compounds $Cu_{2-x}Te$ and Sb_2Te_3. In this work, we report the microstructure and thermoelectric Properties Of $(Cu_2Te)_x$-$(Sb_2Te_3)_{100-x}$ pseudobinary system synthesized by brine quenching method and compare the microstructure and transport properties to the same composition synthesized by solid-state synthesis.

4.1.1. Different media for quenching metal

Metal quenching is one of the main phases in the heat treatment of metal parts because it is a process that adds hardness. The idea is comparatively simple: heat metal and then rapidly cool it to make it harder. The cooling system has a substantial effect on the properties for instance hardness uniformity, microstructure, residual stress, and the strength of hardened part in addition to on the distortion produced by the Harding. Different quenchants offer a different

cooling system, and the character of the quenchant and its cooling capacity may change over time [29].

4.1.1.1. Severity of quenchants

The severity of a quench refers to how quickly heat can be drawn out of a part. Different quenching media have different degrees of severity. Caustics are the most severe quenchants, followed by oils, then salts, and, finally, gases. The makeup of metal parts and the specified hardness to be achieved dictate which quenching medium is used. Generally, lowhardenability parts made from carbon steel and low-alloy steel require more severe quenches to achieve a specified hardness. High-alloy steels, which are much more hardenable, are best quenched in less severe media

Caustics

The most severe quenches are executed with water, brines, and caustic sodas. While these quenchants can pull heat out of parts more quickly than other quenching media, faster isn't always better. Quenching in caustics dissipates heat so quickly that metal parts are at risk of cracking and warping due to the drastic variation in temperature between the part surface and its core. Also, workers must take special precautions when using caustic materials because they're harmful when inhaled or exposed to skin and eyes.

Oil

Quenching metal in oil is the most popular method because it is relatively severe but with a diminished risk of cracking and warping. Also, a wide range of parts quenches well in oils because the chemical makeup and temperature of a quenching oil can be adjusted to suit desired results. For example, if a metallurgist determines a part's intended final properties require faster quenching to achieve, "fast" oils are used. These oils are formulated to extend the amount of time during which the highest rate of cooling takes place. Quenching in fast oils is best suited

for low-carbon steels and low-alloy parts. As the method's name indicates, these quenches do not take long.

Conversely, sometimes cooling needs to be slowed. Hot oils, which are kept at higher temperatures cool metal surfaces, but not so quickly that a part's core temperature and surface temperature differ too widely. High-alloy parts with intricate designs quench well in hot oils, as the method reduces the risk of warping and cracking associated with differences in surface and core temperatures. Quenching in hot oil is a slower process compared to quenching in fast oil. Because oil is flammable, workers must know the flashpoint of the oil in use as well as the load weight and surface area of the products in the workload to avoid fires during quenching.

Molten Salt (Brine)

Quenching metal parts in molten salt (also called salt baths) comes with a further reduced risk of distortion or cracking of parts because they're hotter than hot oils. This means cooling is more controlled and uniform compared to colder, faster, and more severe quenches. The hotter the quenchant, the less severe the quench. The less severe the quench, the lower the risk of distortion. Different mixtures of salts have different melting points and working ranges, offering added versatility as a quenching option. Because salts are not flammable, they pose no risk of fire. On the other end of the spectrum, some salt mixtures have high melting points and working ranges and can be used to heat parts.

Salt baths are a long-lasting heat treating and quenching solution as long as they're correctly maintained. This includes ensuring oxides are regularly removed from high-heat salts and sledging out high-heat salts that contaminate quenches salts on salt-to-salt lines.

Gas

Quenching metal via gas in vacuum furnaces has become more popular for parts that require high hardness and specific finishes with significantly reduced risk of distortion. In gas quenching, parts are sealed in a vacuum chamber before being blasted with gases. The rate of cooling of a part can be precisely controlled by adjusting the pressure and speed at which the gas is delivered. Additionally, because gas quenches occur in vacuum chambers, parts emerge significantly cleaner compared to other quenching media. Nitrogen is the most popular gas quenchant due to its relatively low atomic mass, wide availability, and low cost. Helium and argon are also used in gas quenching. Specified finished qualities dictate which gas quenchants are to be used. High-alloy tool steels and jet engine turbines are typical examples of parts often quenched in gas.

A series of Bi_2 (Se0.4Te0.6)3 compound was synthesized by a rapid rout of melt spinning (MS) combined with a following spark plasma sintering (SPS) process. The measurement results show that the cooling rate of melt spinning had an important influence on the transport properties of electrons and phonons, efficiently improving the TE properties of the compounds.

Thus, the electrical conductivity decreases with the increased cooling rate because of the simultaneous reduction of carrier concentration and mobility. With increasing cooling rate, the electrical conductivity decrease and the seebeck coefficient decreases, however, the dramatic reduction of the thermal conductivities contributes greatly to the improvement of the resultant zT. The sample with the highest cooling rate reached a maximum figure of merit zT of o.93 at 460 K. This may be a reasonable approach to solve the problem of the shortage of the rare element tellurium in thermoelectricity [30].

Because the cooling rate affects the thermoelectric properties [31-33]. From the above and other research paper fast cooling rate increase the thermoelectric properties, especially it reduces the thermal conductivity, which helps to improve the figure of merit zT. Because of

this out of the quenching media, we choose brine (salt) quenching, which has a fast cooling rate out of all quenching media.

4.2. Experimental procedure

We synthesized the pseudobinary alloys of Cu_2Te – Sb_2Te_3 highly pure elemental pellets Cu, Sb, and Te of 99,99 were weighed in a stoichiometric ratio according to nominal composition, which is listed in table 1 from phase diagram of pseudobinary, Cu-Sb-Te, figure 4.2. Brine quenching methods were used to prepare the hypereutectic alloys Cu5 and Cu25, eutectic alloys Cu33, and hypoeutectic of Cu42. The weighed samples were loaded into the quartz tube and sealed in fused quartz tubes with 10 mm inner diameter and 1.5-mm-thick under a vacuum of a $5x10^{-6}$ bar. The alloys were melted via induction Heating for approximately 5 min and then cooled (while still in the fused quartz ampoules) by a method of cooling in air.

After induction melting for brine quenching method, with the help of hand LPG (propane) flame, the alloy was re-melted repeatedly for better homogenization and rapidly quenching in brine salt solution. A compositional deviation is a usual occurrence in Cu–Sb–Te type alloys due to the evaporation of volatile Sb and Te. The densities of the alloys were measured by the Archimedes principle.

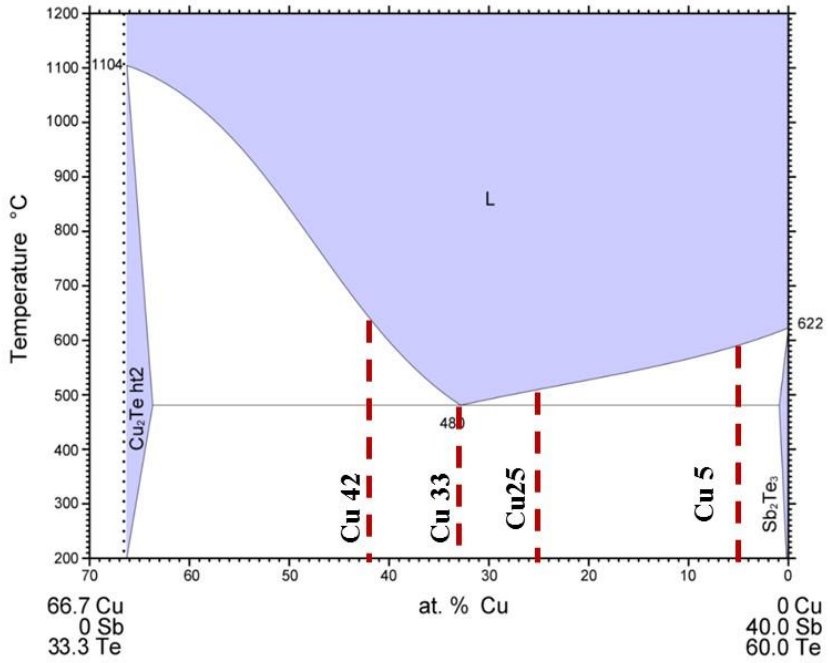

Fig. 4.2: Phase diagram of the Cu_2Te-Sb_2Te_3 pseudobinary system [22]. Cu5 and Cu25 are the hypereutectic alloys; Cu33 is the eutectic alloy; Cu42 is the hypoeutectic alloys.

Alloy Name	***C mposition (at. %)***			***Pseudobinary notation***
	Cu	***Sb***	***Te***	
Cu5	***5***	***37.01***	***57.99***	$(Cu_2Te)_{11.91} - (Sb_2Te_3)_{88.09}$
Cu25	***25***	***25.01***	***49.99***	$(Cu_2Te)_{50.00} - (Sb_2Te_3)_{50.00}$
Cu33	***33***	***20.21***	***46.79***	$(Cu_2Te)_{62.02} - (Sb_2Te_3)_{37.98}$
CU42	***42***	***14.81***	***43.19***	$(Cu_2Te)_{73.95} - (Sb_2Te_3)_{26.05}$

Table 4.1: Nominal compositions of alloys (Cu5, Cu25, Cu33, and Cu42) used in the present study.

The crystal structure was analyzed by the powder x-ray diffraction method at room temperature using a Panalytical X-ray diffraction instrument using Cu-K_α radiation (λ=1.5406 Å) was carried out. All the X-ray diffraction (XRD) measurements were performed on powdered samples in the range of $10 < 2\theta < 80$. The alloys so prepared were cut, mounted in epoxy resins. Then samples were prepared metallographically by polishing with a series of SiC papers up to a grit size of 5000 and then, with 3mm Al_2O_3. The morphologies and the phase were examined using a scanning electron microscope in the backscatter electron mode.

The individual compositions of the two phases are measured with the help of a wavelength dispersive spectroscope (WDS). For each phase at least ten measurements are made. The composition analysis is shown in Table 1. The overall bulk compositions of the alloys measured via the energy dispersive spectroscopy method (EDS) are found to be $Cu_{7.02}Sb_{38.77}Te_{54.21}$, $Cu_{24.75}Sb_{26.755}Te_{48.955}$, $Cu_{33.13}Sb_{20.21.02}Te_{45.86}$, and $Cu_{42.4}Sb_{12.56}Te_{45.04}$, for Cu5, Cu25, Cu33, and Cu42 respectively. The chemical compositions were determined energy dispersive x-ray (EDS) analysis (JEOL).

The as-prepared samples were cut into Cylindrical with dimensions of 12-10 mm^3, for simultaneously measuring the Seebeck coefficient (S) and the electrical conductivity (s). The measurement of transport properties was conducted using standard using the standard fourprobe method in a helium atmosphere in the temperature range of 323 K to 573 K with the temperature gradient of 223 K using ULVAC-RIKO ZEM-3 instrument. Heating and cooling cycles were conducted on each tested sample to give repeatability. The uncertainty of the Seebeck coefficient and electrical conductivity measurements was less than 3%. The thermal conductivity (κ) was measured with a laser flash diffusivity technique by a laser flash TADLF-2800.

Starting composition (at %)	***Overall composition (at%)***		
Elements	***Cu***	***Sb***	***Te***
$Cu_5Sb_{37.0015}Te_{57.9985}$	***7.02±***	***38.77±***	***54.21±***
$Cu_{25}Sb_{25.0015}Te_{49.9925}$	***24.75±0.76***	***26.755±0.36***	***48.495±0.41***
$Cu_{33}Sb_{20.2099}Te_{46.7901}$	***33.13±0.47***	***21.02±0.42***	***45.86±0.06***
$Cu_{42}Sb_{14.8126}Te_{43.1817}$	***42.4±***	***12.56±***	***45.04±***

Table 4.2: Summary of the average composition measured across the different phases observed in Fig. 4.2

4.3. Result and Discussion

4.3.1. X-ray diffraction analysis

The X-ray diffraction patterns of Cu_2Te-Sb_2Te_3 pseudo-binary alloys are shown in Fig.4.3 Cu_2Te, including its nonstoichiometric compound $Cu_{2-x}Te$, possesses the most complicated crystal structure among all the copper chalcogenides. For the hypereutectic (Cu5, and Cu25), eutectic alloy (Cu33), and for the hypoeutectic alloy (Cu42) the XRD peaks were matched with or Cu_7Te_5 (space group P) with crystal system of orthorhombic Sb_2Te_3 (space group R−3m). These samples show the presence of the maximum intensity peak hkl (052) around $\theta = 26.66^{\circ}$ and at hkl (154 around θ = (43.63), which belongs to Cu_7Te_5. In addition to the Cu_7Te_5 peaks, the XRD pattern also confirms the presence of Sb_2T_3 peaks in these samples, which are expected.

Cu_2Te belongs to a hexagonal crystal system with space group P6m2. This hexagonal crystal structure of Cu_2Te was proposed in 1993 [34] and was later found to be in good agreement with crystal structure determined by experimental groups [1, 25]. The XRD pattern for this hexagonal Cu2Te shows that the maximum intensity peak (006) is at $2\theta = 24.72^{\circ}$.

The number of peaks of Sb2Te3 decreased, and that of Cu2Te increased from the sample Cu5 to Cu42, indicating that the concentration of Cu2Te increased. This is as expected from the nominal composition of the pseudobinary system given in Table 4.1. From Fig. 4.3 for Cu42, it can be seen that the presence of the Cu_2Te influences the lattice parameters of Sb_2Te_3 for Cu5, Cu25 Cu33, and Cu42. Both a and c lattice parameters of Sb_2Te_3 increase with an increase in Cu_2Te content. This might be due to the strain and lattice mismatch between the two phases in these alloys.

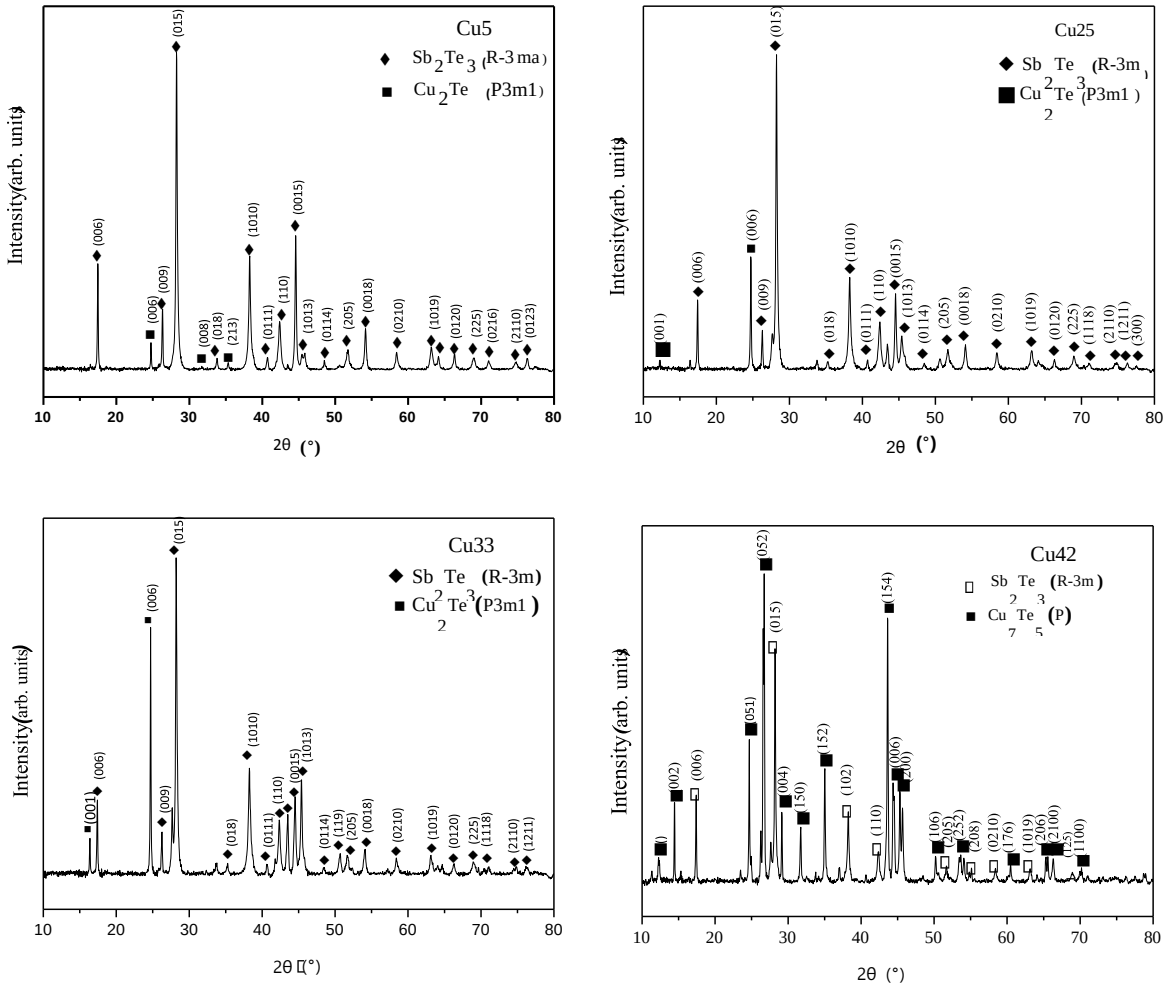

Fig. 4.3: Presents the powder X-ray diffraction patterns of the brine quenched pseudobinary samples Cu5, Cu25, Cu33, and Cu42, with the major diffraction peaks of the Sb_2Te_3 and $Cu_{2-x}Te$ single-phase compounds.

The diffraction peaks of the Sb_2Te_3 and Cu_2Te show single phases of rhombohedra (R3m) Sb_2Te_3 and hexagonal (P6m2) of Cu_2Te crystal structures, respectively. The lattice parameters of Cu_2Te and Sb_2Te_3, which are synthesized by brine quenching methods, are almost the same as those reported in the literature for hypereutectic and eutectic phase [26]. For hypoeutectic, the crystal system is changed to Orthorhombic with a space group of P, which is one of the dive space groups of $Cu_{2-x}Te$ chalcogenides. The chemical composition determined by the EDX analysis does not deviate from the stoichiometric composition. The sample bulk density is very high; approximately 99% of the powder density measured by the Archimedes method. All samples appear to be stable in air at room temperature.

In order to compare the XRD diffraction pattern results of the sample prepared by brine quenched alloying and solid-state synthesized, we compare all compositions to each other. The pattern associated with the process of solid-state synthesis indicates the existence of different phases in SN42, which is a $Cu_{10.7}Te_2$ phase rather than the hexagonal structure Cu_2Te phase, which we obtained by brine quenching. Almost certainly due to the existence of a large number of structural variants for $Cu_{2-x}Te$. No further structural change can be observed.

4.3.2. Microstructure and phase analysis

Scanning electron microscopy imaging (Backscattered electron (BSE) mode) was performed on polished pellets of brine to find the different phases in the samples. The BSE micrographs of the samples, Cu5, Cu25, Cu33, and Cu42 (for brine quenched), are shown in Fig. 4(a).

The sample with the eutectic composition (Cu33) comprises eutectics which are predominantly rod-like with a small number of degenerate eutectics at the boundaries. The BSE images in Fig. 4(b) of the samples Cu42 shows the presence of a dispersed copper telluride phase in the eutectic matrix of the pseudobinary alloy. The microstructures of the Cu_2Te-Sb_2Te_3 pseudobinary system are as expected from the phase diagram given in Fig. 1. For the hypereutectic alloys, Cu5 and Cu25, Brine quenched sample alloys exhibit a rod-shaped structure composed of two phases. Based on the WDS analysis, the darker phase is identified as Cu_2Te. The Cu_2Te exhibits a bimodal grain size distribution, but both large grained and small-grained regions have similar composition, as indicated in Table 2. The lighter phase in brine quenched samples has a stoichiometry, which corresponds to Sb_2Te_3. The lighter phase in Fig. 4.4 corresponds to Sb_2Te_3 (molecular weight of Sb_2Te_3 is 626.32 g/mol), whereas the darker phase corresponds to Cu_2Te (molecular weight of Cu_2Te is 254.69 g/mol). A wavelength dispersive spectrometry (WDS) analysis showed that the phases were off-stoichiometric from their nominal compositions.

As the concentration of copper increases from 5 at.% to 25 at.%, colonies of the eutectic microstructure begin to appear in the matrix of Sb_2Te_3. When Cu is 33 at.% (Cu33), the microstructure is completely eutectic with rod and lamellar shaped. A eutectic reaction occurs when a single liquid phase is transformed simultaneously into two solid phases. During this transformation, there is a redistribution of the components of the two solid phases due to atomic dispersion. Such a transformation results in a microstructure which consists of alternating layers of the two solid phases. The microstructure for Cu33 hence consists of Cu_2Te-Sb_2Te_3 eutectics. These eutectics are both lamellar-shaped and rod-shaped, depending on the growth orientation. The hypoeutectic alloys Cu42 have a microstructure consisting of a mixture of the eutectic structure and regions of the copper telluride-rich phase. In such a microstructure, the copper telluride phase appears in two locations - in the eutectic as well as in the dispersed phase. An exciting feature of the microstructures that can be observed in this system is that unlike the hypereutectic alloys, the copper telluride-rich phase constituent in the hypoeutectic alloys is not continuous with its eutectic constituent. Such features occur when one phase tends to surround the other phase in eutectic systems.

To confirm the composition of the samples, an electron probe microanalysis (EPMA) was carried out for the brine quenched samples using the elemental standards of JEOL JXA8530F wavelength dispersive spectrometry (WDS). The nominal and the observed composition for all the samples taken at several points and averaged are listed in Table 2. As seen from the BSE images, the WDS results also suggest the presence of the darker and lighter phases in the samples Cu5 and Cu25. The composition of this lighter phase is similar to the Sb_2Te_3, and the darker phase is Cu_2Te. The WDS results show that all the samples have a deficit of copper in the copper telluride phase. In Table 2, it can be seen that the composition of the copper telluride-rich phase in the hypoeutectic The WDS composition of the lighter phase (Sb_2Te_3) agrees well with the nominal composition.

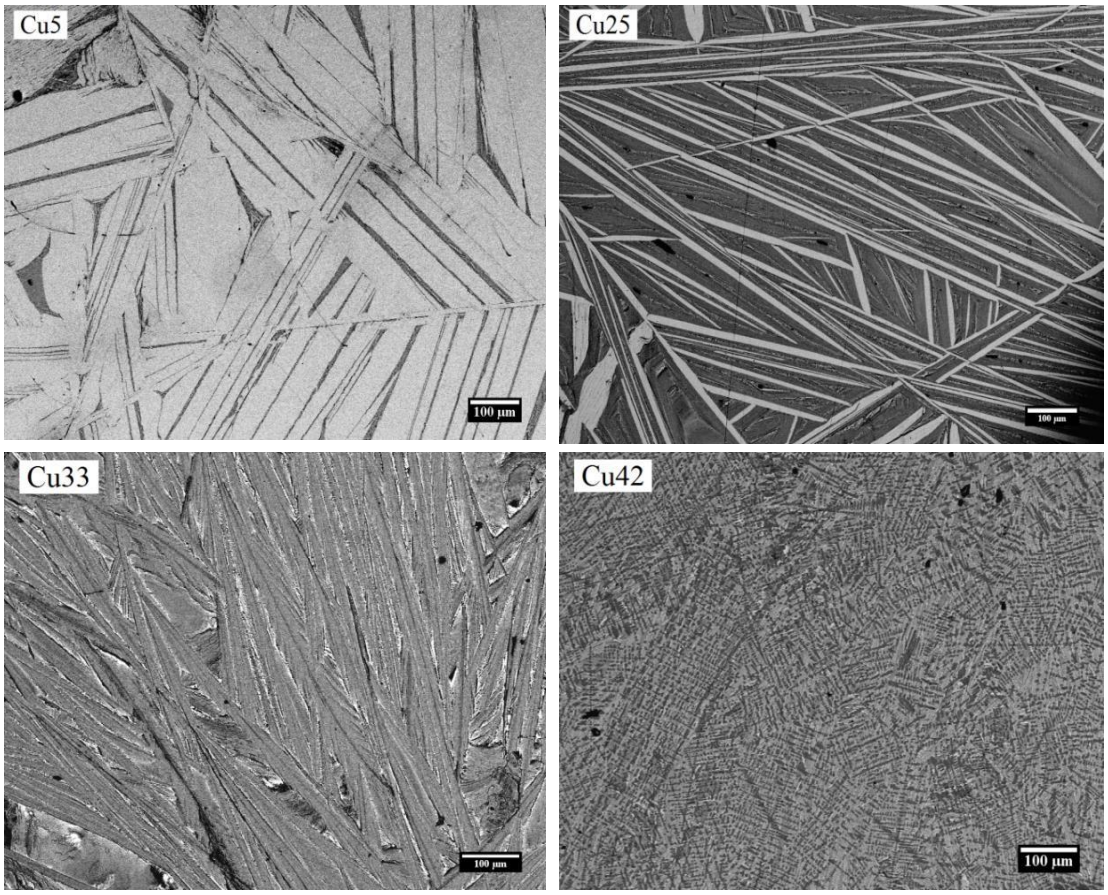

Fig. 4.4: Backscattered electron micrographs of hot-pressed samples Cu5, Cu25, Cu33, and Cu42. The darker phase corresponds to $Cu_{2-x}Te$, whereas the lighter phase corresponds to Sb_2Te_3.

As we expected from BSE, for Cu5 and Cu25 predominately, the majority phase is Sb_2Te_3. The finite assemblage of rod-like Cu_2Te phase segregated in the lamellae structured phase, which is found in a small amount on the large matrix of Sb_2Te_3. The lamellae structure is observed for Cu25, which is very less in SN25. This structure significantly affects the electronic flow, which leads to lower electrical conductivity. For Cu33, Cu_2Te finitely scattered on the matrix of Sb_2Te_3. That is why it gives a dark grey phase to SN33. It has both Lamellae and rod-shaped structure. Cu42 Shows mixture of eutectic phase and Cu_2Te Cu_2Te phase found on both on scattered phase, and eutectic phase Solid state synthesized sample has regular phase shape than brine sample. Quenching can cause internal stresses on the solidified alloys, leading to geometrical and microstructural alteration or deformation during subsequent brine (salt) quenching operations [35].

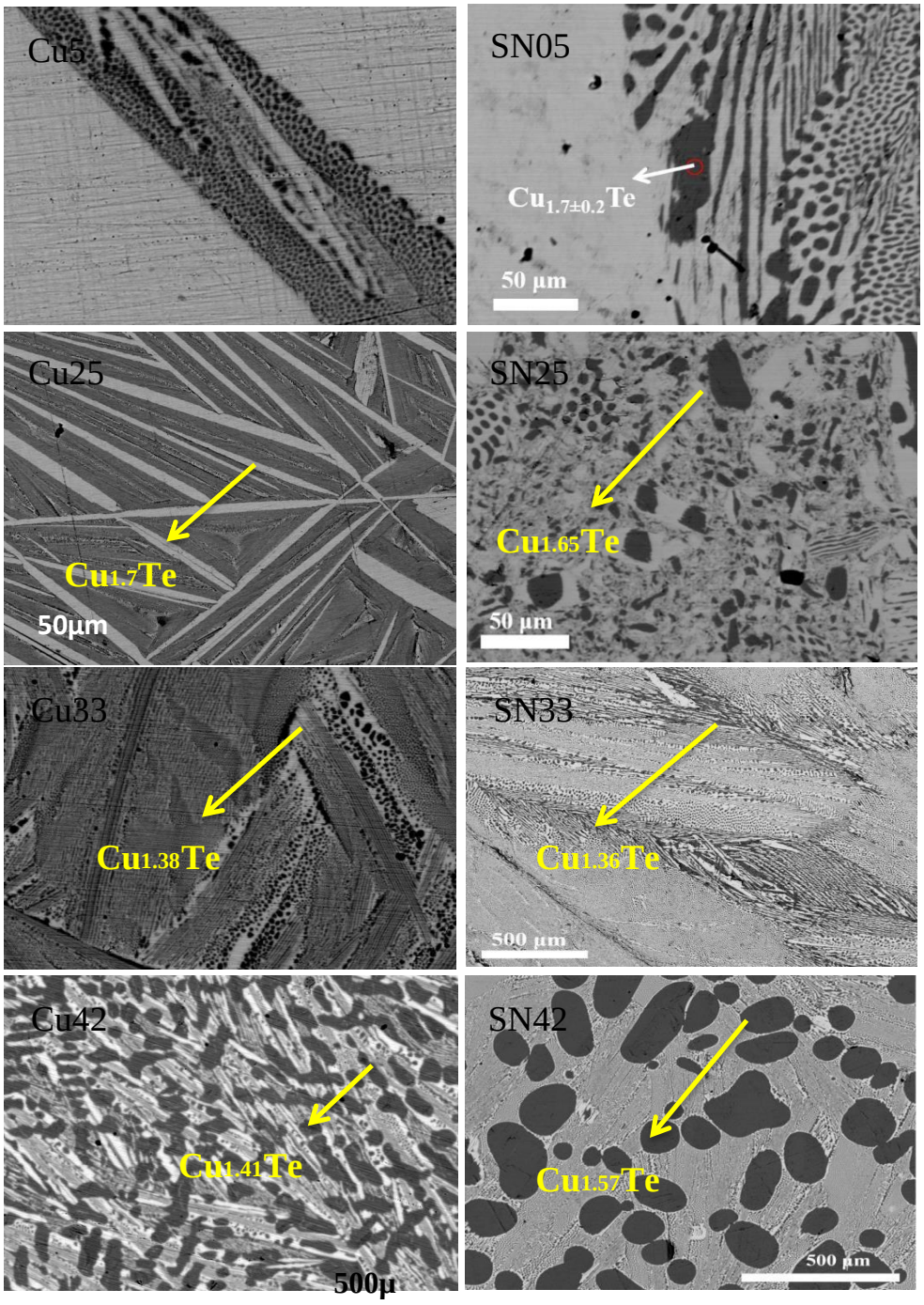

Fig 4.5. Copper vacancy (Cu_V) comparison between Backscattered electron micrographs of brine quenched samples (Cu5, Cu25, Cu33 and Cu42) and hot-pressed samples (SN05, SN25, SN33 and SN42)

4.3.3. Thermoelectric Transport properties analysis

The Seebeck coefficients of the Cu_2Te- Sb_2Te_3 composites synthesized by the brine quenching method are presented in Fig. The Seebeck coefficient increases with increasing temperature (from room temperature 300K to 573K), which this linear increase of the Seebeck coefficient

indicates the metallic behaviour of the alloys. Because of the decreased electrical conductivity, the Seebeck coefficient increases with increasing Cu_2Te dispersion concentration. The absolute seebeck coefficient value is positive for all the samples throughout the measurement temperature range, and this indicates that holes are the majority charge carriers and it is a p-type semiconductor.

The highest value of the Seebeck coefficient is recorded for Cu5, which is 113.8uV/K at 573K, which is higher than previously report Seebeck coefficient values synthesized by the solid-state method.

The Seebeck coefficient increases with increasing temperature for the brine quenching sample, which is p-type TE material. Pristine Sb_2Te_3 and Cu_2Te show the formation of antisite defects of Sb_{Te} (accepter like defect) and vacancy of Cu (V_{Cu}), respectively. This trend can also be seen in Fig.4.5. This leads to the creation of holes in carrier concentration. Cu5 and SN05 have the highest Seebeck coefficient among all samples because both are Sb_2Te_3 reach. Also comparing to SN05, Cu5 has high Seebeck because of lower Cu vacancy (V_{Cu}), which increase Seebeck coefficients.

The power factor (PF) was calculated using the relationship PF = S^2ó. PF increases with increasing temperature for all the samples. It shows a trend similar to that of the Seebeck coefficient over the measured temperature range. A higher PF is obtained for Cu5 (1.4 mW m^{-1} K^{-2} at 573 K) owing to the higher Seebeck coefficient compared to those of Cu25 and Cu33. This value is, however, lower than that reported in the literature (1.8 mW m^{-1} K^{-2} at 572 K) [26] due to the higher Seebeck coefficient in Cu5.

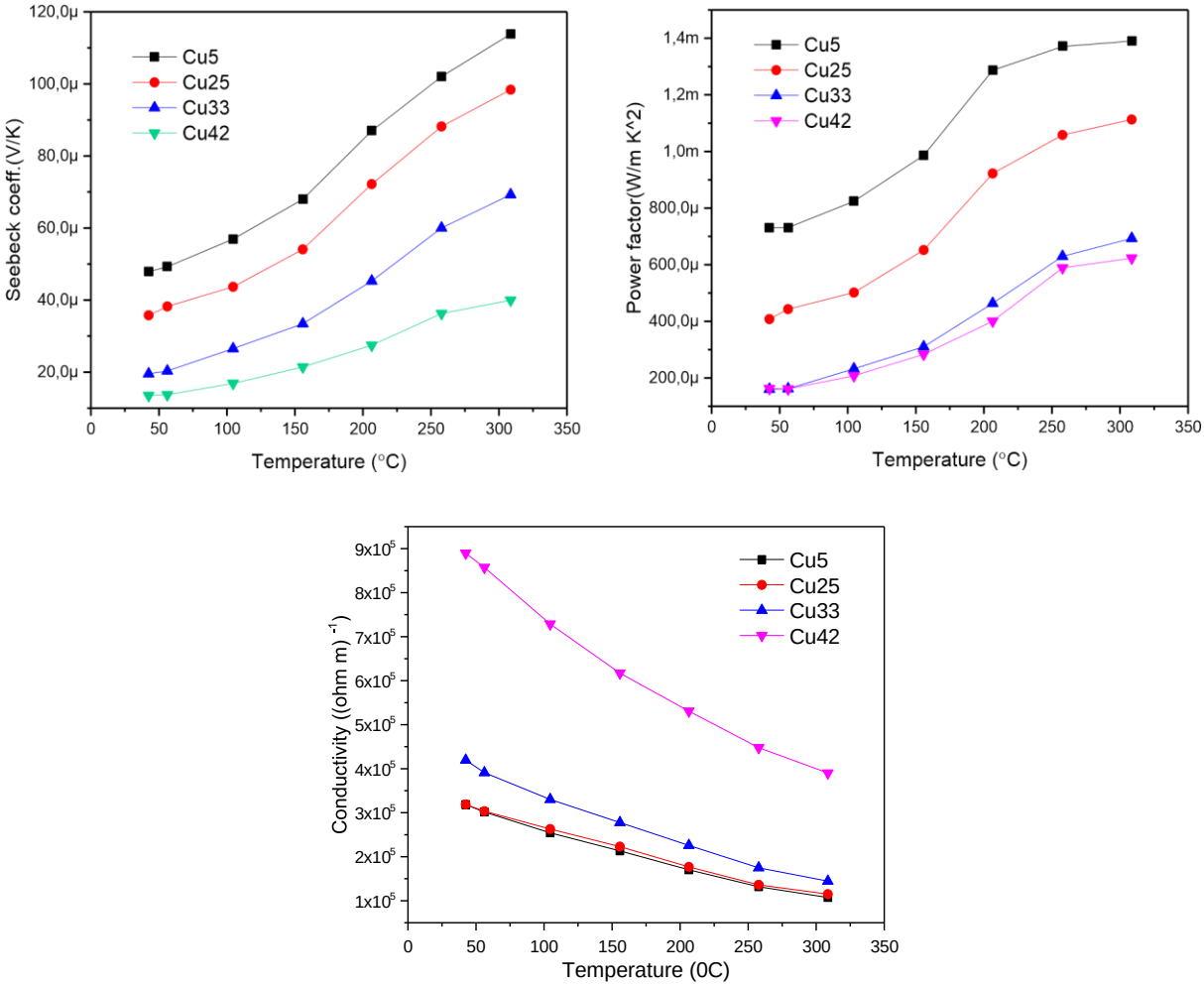

Fig. 4.6: Transport properties of the samples (Cu5, Cu25, Cu33, and Cu42, SN52 as a function of temperature. The positive Seebeck coefficient indicates that holes are the majority charge carriers in these alloys.

An added advantage of synthesizing compounds by the brine (salt) quenching route over solid-state routes is the production of extremely fine-grained microstructure. The microstructure reveals the flow lines in the grains and structure. This feature helps the scattering of phonon better than sample prepared by solid-state synthesis

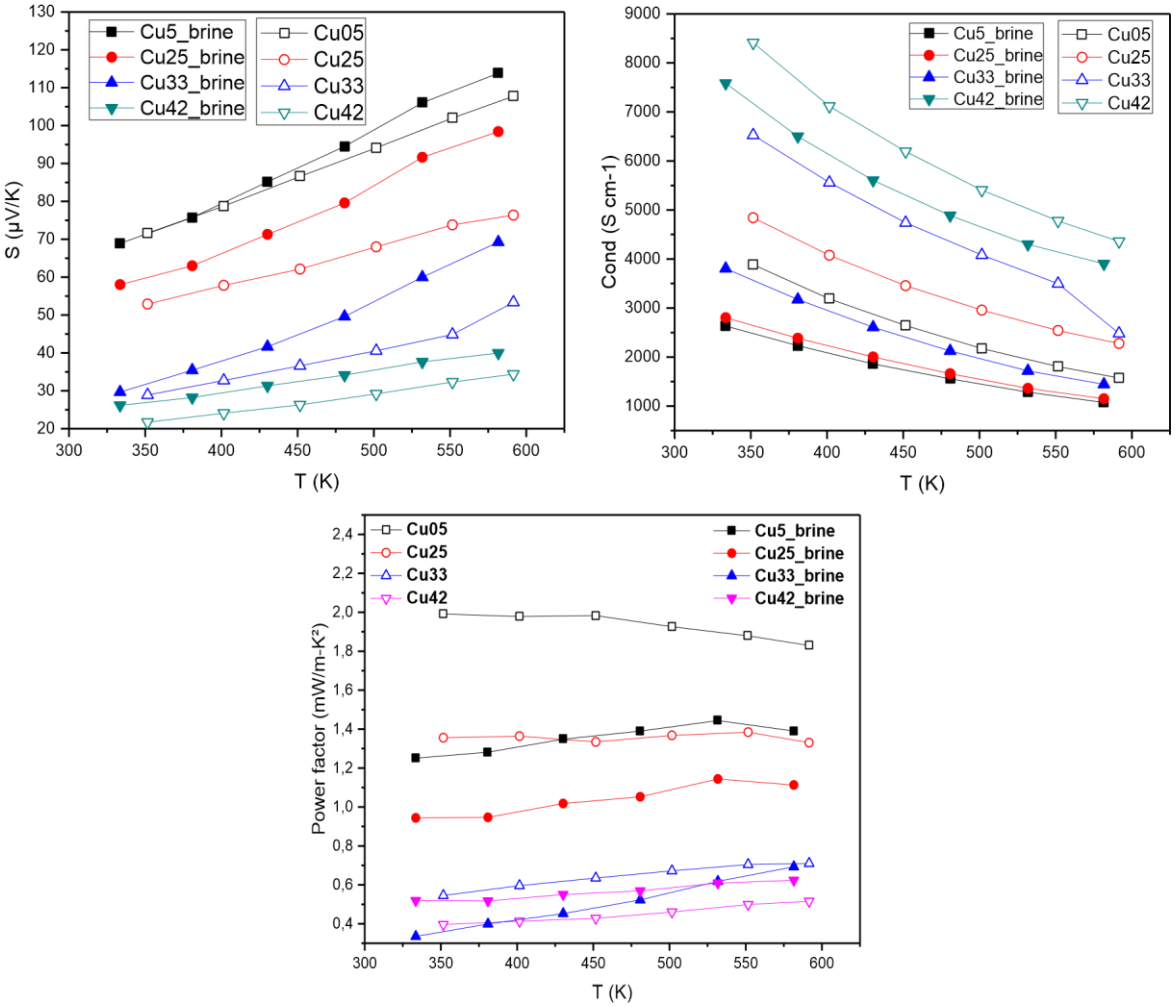

Fig. 4.7: Comparison between the transport properties of brine quenched sample and Hot pressed samples

Seebeck coefficient increases with increasing temperature for the brine sample, which is p- type TE material. Pristine Sb_2Te_3 and Cu_2Te shows the formation of anti-site defect of Sb_{Te} (accepter like defect) and vacancy of Cu (V_{Cu})respectively. This leads to the creation of holes in carrier concentration. Cu5 and SN05 have the highest Seebeck coefficient among all samples because both are Sb_2Te_3 reach. Also comparing to SN05, Cu5 has a high Seebeck because of lower Cu vacancy, which increases Seebeck coefficients.

Electrical conductivity (σ) of all the sample decrease with increasing temperature. This shows metallic behaviour at room temperature, Cu5 has the lowest σ (2.8 $*10^3$ S/cm) compering to Cu5 (4$*10^3$ S/cm). This happens because:-

1. As Cu_2Te increases, σ also increases because pristine Cu_2Te ~ 10^{-4} S/cm has higher electrical conductivity than Sb_2Te_3(~10^{-3}S/cm)
2. Brine sample creates a lower Cu vacancy (V_{Cu}) than a solid-state synthesized sample, which this vacancy leads to an increase in carrier concentration (n). $\sigma = (ne^{2l})/Vm^*$

PF is the combined effect of electrical conductivity and the Seebeck coefficient. The electrical conductivity of the solid-state synthesized sample is higher than the brine sample.

4.4. Conclusion

The pseudo-binary alloys of (Cu_2Te) x-(Sb_2Te_3)100-x) with starting composition of ($Cu_5Sb_{37.0015}Te_{57.9985}$, $Cu_{25}Sb_{25.0015}Te_{49.9925}$, $Cu_{33}Sb_{20.2099}Te_{46.7901}$, $Cu_{42}Sb_{14.8126}Te_{43.1817}$) were synthesized by brine quenching methods. The existence of Cu_2Te and Sb_2Te_3 phase in the alloys were confirmed by X-ray diffraction and WDS. The temperature-dependent Seebeck coefficient and electrical conductivity were measured at a temperature between 350 and 600 K for the alloys. The electrical conductivity decreases with temperature indicating metal-like behaviour. The Seebeck coefficients were positive in all the alloys which imply that majority carriers were holes. A systematic decrease in S and an increase in σ with Cu content were due to an increase in carrier concentration caused by the easy formation of Cu vacancies in Cu 2xTe. Brine sample creates a lower Cu vacancy (V_{Cu}) than a solid-state synthesized sample, which this vacancy leads to an increase in carrier concentration (n). $\sigma = (ne^{2l})/Vm^*$. The effect of lamellar phase boundaries on electron scattering for the eutectic alloy was not significant enough to reduce σ. The control of interfaces in this pseudo-binary system can be an important strategy in tuning the thermoelectric parameters.

4.5. References

1. Champier, D., *Thermoelectric generators: A review of applications.* Energy Conversion and Management. **140**: p. 167-181.

2. Jaziri, N., et al., *A comprehensive review of Thermoelectric Generators: Technologies and common applications.* Energy Reports.

3. Rademann, K., et al., *Chapter 3 - Crystallization and Growth Mechanisms of Nanostructures in Silicate Glass: From Complete Characterization Toward Applications*, in *Glass Nanocomposites*, William Andrew Publishing: Boston. p. 89114.

4. M. Liebscher, T.G., L. Tzounis, M. Micˇušík, P. Pötschke, M. Stamm, G. Heinrich, B. Voit, *Influence of the MWCNT surface functionalization on the thermoelectric properties of melt-mixed polycarbonate composites.* (2014). **101**: p. 133-138.

5. Terry, M.T., *Electrical and thermal transport measurement techniques for evaluation of the figure of- merit of bulk thermoelectric materials, Thermoelectrics Handbook.* CRC Press,Taylor & Francis Group, Boca Raton, New York, (2005) p. 23-20-23-21.

6. Ponnamma, D., et al., *12 - Piezo- and Thermoelectric Materials From Biopolymer Composites*, in *Biopolymer Composites in Electronics*, Elsevier. p. 333-352.

7. Wood, C., *Materials for thermoelectric energy conversion.* Reports on Progress in Physics, 1988. **51**(4): p. 459-539.

8. Fu, B., G. Tang, and Y. Li, *Electronâ€“phonon scattering effect on the lattice thermal conductivity of silicon nanostructures.* Physical Chemistry Chemical Physics. **19**(42): p. 28517-28526.

9. Zhao, X., X.-h. Zhu, and R.-z. Zhang, *Evaluation of energy filtering effect from first principles calculations.* physica status solidi (a). **213**(12): p. 3250-3253.

10. Yu, B., et al., *Enhancement of Thermoelectric Properties by Modulation-Doping in Silicon Germanium Alloy Nanocomposites.* Nano Letters. **12**(4): p. 2077-2082.

11. Jiang, Q., et al., *Enhancement of thermoelectric properties by atomic-scale percolation in digenite CuxS.* Journal of Materials Chemistry A. **2**(25): p. 9486-9489.

12. Guin, S.N., A. Banik, and K. Biswas, *Thermoelectric Energy Conversion in Layered Metal Chalcogenides*, in *2D Inorganic Materials beyond Graphene*, WORLD SCIENTIFIC (EUROPE). p. 239-274.

13. Han, C., et al., *Thermoelectric Enhancement of Different Kinds of Metal Chalcogenides.* Advanced Energy Materials. **6**(15): p. 1600498.

14. Tzounis, L., et al., *Chapter 9 - Synthesis and Processing of Thermoelectric Nanomaterials, Nanocomposites, and Devices*, in *Nanomaterials Synthesis*, Elsevier. p. 295-336.

15. Das, D., et al., *Defect induced structural and thermoelectric properties of Sb2Te3 alloy.* Journal of Applied Physics. **118**(4): p. 045102.

16. Femi, O., R. Narayanan, and K. Chattopadhyay, *Microstructure evolution and thermoelectric properties of Te-poor and Te-rich (Bi,Sb)2Te3 prepared via solidification.* Journal of Materials Science. **51**.

17. Wang, X.-y., et al., *The Thermoelectric Performance of Sb2Te3-based Alloy is Improved by Introducing PN Junctions.* ACS Applied Materials & Interfaces. **10**.

18. Xu, B., et al., *Thermoelectric properties of monolayer Sb2Te3.* Journal of Applied Physics. **124**(16): p. 165104.

19. Yoo, I.-J., et al., *Thermoelectric characteristics of Sb2Te3 thin films formed via surfactant-assisted electrodeposition*. Journal of Materials Chemistry A. **1**: p. 54305435.

20. Lee, M.H., et al., *High thermoelectric figure-of-merit in Sb2Te3/Ag2Te bulk composites as Pb-free p-type thermoelectric materials.* Journal of Materials Chemistry C. **3**(40): p. 10494-10499.

21. Mallick, M.M. and S. Vitta, *Realizing high figure-of-merit in Cu2Te using a combination of doping, hierarchical structure, and simple processing.* Journal of Applied Physics. **122**(2): p. 024903.

22. Qiu, Y., et al., *Facile rapid synthesis of a nanocrystalline Cu2Te multi-phase transition material and its thermoelectric performance.* RSC Advances. **7**(36): p. 22558-22566.

23. Snyder, G.J. and E.S. Toberer, *Complex thermoelectric materials.* Nat. Mater., 2008. **7**.

24. Lee, M.H., et al., *High thermoelectric figure-of-merit in Sb2Te3/Ag2Te bulk composites as Pb-free p-type thermoelectric materials.* J. Mater. Chem. C. **3**.

25. Ikeda, T., et al., *Self-Assembled Nanometer Lamellae of Thermoelectric PbTe and Sb2Te3 with Epitaxy-like Interfaces.* Chemistry of Materials, 2007. **19**(4): p. 763-767.

26. Mukherjee, S., et al., *Microstructure and thermoelectric properties of Cu2Te-Sb2Te3 pseudo-binary system.* Applied Surface Science. **449**: p. 805-814.

27. Venkatasubramanian, R., et al., *MOCVD of Bi2Te3, Sb2Te3 and their superlattice structures for thin-film thermoelectric applications.* Journal of Crystal Growth, 1997. **170**(1): p. 817-821.

28. Cao, Y.Q., et al., *Syntheses and Thermoelectric Properties of Bi2Te3/Sb2Te3 Bulk Nanocomposites with Laminated Nanostructure.* Applied Physics Letters, 2008. **92**: p. 143106-143106.

29. Troell, E., et al., *12.04 - Controlling the Cooling Process â€“ Measurement, Analysis, and Quality Assurance*, in *Comprehensive Materials Processing*, Elsevier: Oxford. p. 99-121.

30. Wang, S.Y., et al., *Effects of Cooling Rate on Thermoelectric Properties of n-Type Bi2(Se0.4Te0.6)3 Compounds.* Journal of Electronic Materials. **40**(5): p. 1150-1157.

31. Appel, O., et al., *Morphological effects on the thermoelectric properties of Ti0.3Zr0.35Hf0.35Ni1+Î´Sn alloys following phase separation.* Journal of Materials Chemistry C. **3**(44): p. 11653-11659.

32. Wang, S., et al., *Effects of Cooling Rate on Thermoelectric Properties of n-Type Bi2(Se0.4Te0.6)3 Compounds.* Journal of Electronic Materials. **40**: p. 1150-1157.

33. Yamashita, O., T. Ochi, and H. Odahara, *Effect of the cooling rate on the thermoelectric properties of p-type (Bi0.25Sb0.75)2Te3 and n-type Bi2(Te0.94Se0.06)3 after melting in the bismuthâ€“telluride system.* Materials Research Bulletin, 2009. **44**(6): p. 1352-1359.

34. Ghoumari-Bouanani, H., Brun, G., Liautard, B., Tedenac, J., . Mater. Res. Bull. , 1993: p. 28, 901,.

35. Vargel, C., *Chapter A.3 - The Metallurgy of Aluminium*, in *Corrosion of Aluminium*. 2004, Elsevier: Amsterdam. p. 23-57.

CHAPTER FIVE

5. Summary, conclusion and future work

5.1. Summary and conclusion

In this work, we try to tune the thermoelectric transport properties of the pseudo-binary Cu_2Te-Sb_2Te_3 system by unidirectional solidification and brine quenched. In the first case to achieve this we study this on a set of pseudo-binary Cu_2Te-Sb_2Te_3 eutectic alloys through directional solidification using a modified-Bridgman type apparatus. From this, the morphology of eutectic is lamellar inside the colony at higher velocities, i.e., V = 32, 16 μm/s. However, with a decrease in velocity to V = 4, 1 μm/s, we observe predominantly degenerate lamella morphology of the eutectic. Morphology of the colonies observed in all cases is plate type.

In the case of transport properties, there is a systematic trend between electrical conductivity and lamellar spacing in both longitudinal and transverse cases. However, the conductivity has reduced significantly (almost by half) in the transverse direction compared to the longitudinal direction. This is because, when the electrical conductivity is measured in the longitudinal direction, the equivalent electrical circuit will be similar to that of resistors (here the $Cu_2TeSb_2Te_3$ eutectics) connected parallel to each other. Compared to a series connection with the same set of resistors, the overall resistivity will be low (i.e., conductivity will be high) in parallel configuration (longitudinal direction). The alloys exhibit p-type semiconducting nature, as can be observed from positive values of Seebeck coefficients. The following defect equilibrium relations on equation (3.3 and 3.4) shows the origin of the p-type conductivity. The Cu vacancies (V'_{Cu}) and the antisite defects (Sb'_{Te}) leads to the creation of holes ($h^{\cdot}$) in the pseudo-binary alloys.

The microstructure effect on transport properties of Cu_2Te-Sb_2Te_3 is described by the effect of lamellar spacing. As the lamellar spacing increases, the available charge carriers are more since it does not undergo scattering. Seebeck coefficient will decrease with increase in lamellar

spacing. In the longitudinal direction, the Seebeck values decrease systematically to 1.86 μm. Thereafter, a slight increase in *S* can be observed as the lamellar spacing increased to 2.41 μm. In the transverse direction, the Seebeck value was ~ 88 μV K^{-1} at 0.95 μm and showed a peak at 1.46 μm. Thereafter it decreased systematically from 104 μV K^{-1} to 90 μV K^{-1} with an increase in the lamellar spacing from 1.46 μm to 2.41 μm. The PF increased with an increase in lamellar spacing in both the directions of measurement. The highest power factor was obtained for the alloy with 2.41 μm along the transverse direction.

In the second case, we tune the thermoelectric transport properties of the pseudo-binary Cu2Te-Sb2Te3 system by brine quenching. And compare the microstructure and transport properties to the same composition synthesized by solid-state synthesis.

The X-ray diffraction patterns of Cu_2Te-Sb_2Te_3 pseudo-binary alloys For the hypereutectic (Cu5, and Cu25), eutectic alloy (Cu33) The diffraction peaks of the Sb_2Te_3 and Cu_2Te show single phases of rhombohedra (R3m) Sb_2Te_3 and hexagonal (P6m2) of Cu_2Te crystal structures, respectively, and for the hypo-eutectic alloy (Cu42) the XRD peaks were matched with Cu_7Te_5 (space group P) with crystal system of orthorhombic and with for Sb_2Te_3 (space group R−3m).

The sample with the eutectic composition (Cu33) comprises eutectics which are predominantly rod-like with a small number of degenerate eutectics at the boundaries. As the concentration of copper increases from 5 at. % to 25 at. %, colonies of the eutectic microstructure begin to appear in the matrix of Sb2Te3. When Cu is 33 at. % (Cu33), the microstructure is completely eutectic with rod and lamellar shaped.

The highest value of the Seebeck coefficient is recorded for Cu5, which is 113.8uV/K at 573K, which is higher than previously report Seebeck coefficient values synthesized by the solid-state method. Pristine Sb_2Te_3 and Cu_2Te show the formation of anti-site defects of Sb_{Te} (accepter like defect) and vacancy of Cu (V_{Cu}), respectively. This leads to the creation of holes in carrier

concentration. Cu5 and SN05 have the highest Seebeck coefficient among all samples because both are Sb_2Te_3 reach. Electrical conductivity (σ) of all the sample decrease with increasing temperature. This shows metallic behaviour at room temperature, Cu5 has the lowest σ (2.8 $*10^3$ S/cm) compering to Cu5 ($4*10^3$ S/cm). This happens because:-

A higher PF is obtained for Cu5 (1.4 mW m^{-1} K^{-2} at 573 K) owing to the higher Seebeck coefficient compared to those of Cu25 and Cu33. This value is, however, lower than that reported in the literature (1.8 mW m^{-1} K^{-2} at 572 K) due to the higher Seebeck coefficient in Cu5.

5.1. Future works

Thermoelectric devices will be used widely for personal electronic applications. These applications range from wearable items, such as clothes or watches, to biomedical applications such as vital signs monitoring and drug delivery. Recent technology can provide devices for micro-thermoelectric applications, such as cooling of an integrated circuit. But, to reach the full potential of these applications, cost-effective mass production techniques need to be developed, and the performance needs to be optimized. This can be done by one of the following ways.

1. Optimizing the efficiency, effectiveness and reliability "E-E-R" our materials through different techniques, which include finding dopant and using different synthesizing methods
2. Improving the thermoelectric transport properties using Nano-grains, Nano-inclusions and nanoparticles strategies to reducing the lattice thermal conductivity and improving the ZT value
3. Finding good Contact materials with high thermal and electrical conductivity to prevent our thermoelectric material from degrading quickly at the working temperature.
4. Finding a way to form pseudo-ternary alloy from our pseudo-binary alloy and Investigating The effect of the combinatorial approach to microstructure and transport properties